Search for Heavy Stable Charged Particles at the CMS Experiment

A DISSERTATION
SUBMITTED TO THE FACULTY OF THE GRADUATE SCHOOL
OF THE UNIVERSITY OF MINNESOTA
BY

Seth Isaac Cooper

IN PARTIAL FULFILLMENT OF THE REQUIREMENTS
FOR THE DEGREE OF
Doctor of Philosophy

Yuichi Kubota

October, 2012

Acknowledgements

Anyone who has been through it before will tell you that completing a doctoral degree is an enormous effort! I've been fortunate to have been surrounded by people who have been supportive of me throughout the process. Without them, this would have been surely less enjoyable and even more difficult!

First of all, I'd like to thank my parents for nurturing my interest in science, and providing a never-ending source of positive encouragement. Throughout my life they've always been there to make me feel better, even in the darkest times.

I'd like to acknowledge my high school physics and chemistry teacher, Michael Roddy, who was a positive influence on my future in science.

At Carleton, Professor Arjendu Pattanayak encouraged me during a particularly difficult period. I'd also like to acknowledge my classmates and the physics department as a whole for positive feedback and support, with a special mention to Professor Bill Titus.

I did a Research Experience for Undergraduates in the summer of 2004 at Michigan State University, and my advisor there, Professor Carlo Piermarocchi, gave me confidence that I could succeed in a research environment and that graduate school would be the right idea. Although now I'm a long way from theoretical condensed matter!

I want to thank Professor Steve Gasiorowicz and Rabbi Harold Kravitz for supporting me and suggesting that I come to Minnesota.

At Minnesota, I want to mention those who I worked with in office 58, Mike Erickson, Matt Loth, Tanner Schulz, and Tom Kelley. There were many intense discussions about physics and other things. Thanks to Mike especially for bike rides and late night discussions.

Eric Grashorn gets a special mention. Not only a study partner for the written Ph.D.

qualification exam, but also a workout partner, a musical collaborator, and someone who would always listen to my complaints!

I'd like to thank Jason Haupt, a fellow graduate student at Minnesota on CMS, who acted as a mentor for me in the very early stages of my research, introducing me to the ECAL among other things.

Giovanni Franzoni has served as a mentor and role model for me within the Minnesota group, along with being a partner with me in many ECAL efforts. Along with nearly always having a good suggestion, I look up to his work ethic, integrity, and dedication.

Professor Yurii Maravin has acted as a professional mentor beginning with the first summer I travelled to CERN. I continue to trust and respect him greatly.

I really appreciate being able to work with and talk to Camilo Carrillo, another source of support and feedback.

For tirelessly responding to my questions about the Heavy Stable Charged Particles analysis, I acknowledge Loic Quertenmont.

I'd be remiss if I didn't thank my advisor, Professor Yuichi Kubota. From the beginning of my career at Minnesota until now, Yuichi has supervised my progress. I wouldn't have started this process without his support, and throughout it, he has been a nonstop advocate for me. I greatly appreciate his concern for my personal life in addition to my academic life, displaying extraordinary patience.

Finally, I'd like to thank someone very special to me, Laura Tchernin. Her patience, understanding, and wisdom are boundless, and she helped me at many times through this process.

Abstract

A method of searching for Heavy Stable Charged Particles (HSCP) using dE/dx and momentum measurements from the CMS inner tracking system is presented. The shape of the dE/dx distribution is used to distinguish background from signal, in combination with slicing the data into bins of pseudorapidity and number of dE/dx measurements, which together extend and improve on a previous analysis conducted as a counting experiment. In particular, the expected minimum cross section to make a discovery of 5σ significance is reduced, and expected upper limits are more restrictive. The data are consistent with the background-only hypothesis and are used to set upper limits on the production cross section as a function of mass for several different HSCP models. The data sample used was collected by the CMS detector in 2011 pp collisions at $\sqrt{s} = 7$ TeV, corresponding to approximately 5 fb^{-1}.

Contents

List of Tables

List of Figures

Chapter 1

Introduction

The leading theory of particle physics, the Standard Model, has had astonishing success in the experimental realm. Its predictions have been verified to an extremely high degree of accuracy. But there are important missing pieces.

This thesis describes a search for a type of new particle that could help to provide some of these pieces. Called Heavy Stable Charged Particles (HSCP), their observation would be a remarkable signal of theories predicting new physics.

The data used here was collected by the Compact Muon Solenoid (CMS) detector in 2011 using proton-proton collision data at a center of mass energy of 7 TeV produced by the Large Hadron Collider (LHC). The HSCPs produced at the LHC have high momenta but also large masses, and therefore travel slowly, giving rise to a large ionization energy deposit in the detector. This distinctive signature is used to distinguish these particles from the background of Standard Model particles.

In Chapter 2, the Standard Model is introduced and some of its gaps are described. Some of the theories which could help plug these gaps are described, and it is shown that they can predict HSCPs.

Chapter 3 describes the LHC machine and the CMS detector, including design requirements and performance.

Chapter 4 is dedicated to work done on the CMS electromagnetic calorimeter (ECAL) in the course of the thesis research. In particular, the ECAL timing calibration and performance is described and examined.

In Chapter 5, a novel search for "satellite" concentrations of protons in the LHC

beam surrounding the main proton bunch is described. This is an interesting and useful application of the ECAL timing, allowing a reduction of the uncertainty on the beam current and therefore, the luminosity measurement.

For the HSCP search, it is essential to be able to reconstruct the particle mass from the detector information. Chapter 6 details the mass reconstruction technique used in the HSCP search, including some background of specific ionization, the optimal combination of the available detector information, and some important instrumental effects.

Chapter 7 details the HSCP analysis method itself, including the triggers used to record events with an HSCP to tape, the selections, the data-driven background determination, the systematic uncertainties, and the results.

Chapter 2

The Standard Model and HSCP Phenomenology

2.1 Overview of the Standard Model

The Standard Model of particle physics describes the interactions of matter via the electroweak and strong forces. A relativistic quantum field theory, it incorporates the group symmetries of $SU(3)_C \times SU(2)_L \times U(1)$ and how they are spontaneously broken. Matter is made up of point-like particles, called fermions. In their interactions the fermions exchange particles called bosons, which propagate the various forces. Each fermion or boson can be described by a series of quantum numbers, such as their charge, spin, and color, in addition to their mass. The fermions have half-integer spin (typically 1/2) while the bosons have integer spin (typically 1). The particle content of the Standard Model is depicted in Figure 2.1.

The fermions have three generations, each generation consisting of two quarks, which experience the strong interaction, and two leptons, which do not. These generations have similar properties, but differ in their masses, which increase from one generation to the next. Typically, matter is composed of particles of the first generation only, as the particles of the second and third generation decay in a short time to first generation particles. For example, atoms are made of protons, neutrons, and electrons, the proton and neutron consisting of up and down quarks only, and the electron being an elementary particle itself. Each fermion has an oppositely-charged antiparticle.

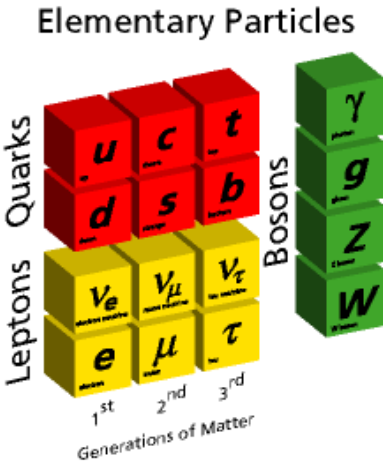

Figure 2.1: The elementary particles making up the Standard Model, without the Higgs boson [1].

The bosons represent the interactions: the photon is the carrier of the electromagnetic force, the W^+,W^- and Z bosons carry the weak force, and the eight gluons carry the strong force. Another boson, the Higgs, has yet to be observed directly, but is necessary to give mass to the other particles by way of electroweak symmetry breaking. The Higgs is predicted to have spin 0, and is expected to be discovered at the Large Hadron Collider.

The Standard Model has been tested extensively and shown to agree extremely well with experiments. The mass of the Z and W bosons, their widths, and the mass of the top quark have been predicted to better than 1 sigma with respect to the experimental uncertainty [2]. Figure 2.2 shows some electroweak measurements from CMS compared to their predictions, and the agreement is evident. However, there are several open questions that motivate so-called "beyond the standard model" (BSM) physics at energy scales above the electroweak regime of about 100 GeV. One issue is known as the "hierarchy problem:" the fact that in the Standard Model there seem to be two fundamental energy scales with nothing in between them: the electroweak (EW) at $\sim$ 100 GeV and the Planck mass scale $M_P = \sqrt{\hbar c/G} \sim 10^{19}$ GeV. As will be discussed later, the consequences of this involve large corrections to the masses of all the particles, something to be avoided. One solution is to introduce supersymmetry [4].

Another issue is that of dark matter and dark energy, which make up 96% of the

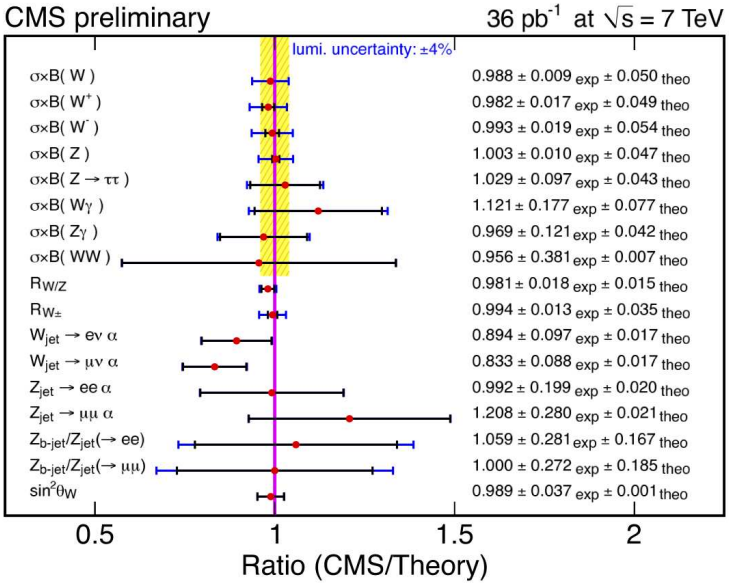

Figure 2.2: Electroweak measurements from CMS compared to Standard Model predictions, including the W and Z cross section times branching ratio, the W/Z and W+/W- cross section ratio, and the sine-squared of the Weinberg angle [3].

universe [5]. The Standard Model by itself does not describe them, but supersymmetric models can provide candidates for dark matter. Supersymmetry is therefore a well-motivated theory, and much effort is put into searching for it. As Heavy Stable Charged Particles (HSCP) are predicted by several supersymmetric models, observing them would be a signal of supersymmetry, or at least BSM physics.

2.2 Models of Heavy Stable Charged Particles

Heavy Stable Charged Particles (HSCPs) could be detected quite early at the Large Hadron Collider (LHC). In fact, at the LHC a large parameter space of many models predicting HSCPs can be excluded with as little as 100 pb^{-1} of integrated luminosity. Several different theoretical models predict particles which fit these characteristics. In general, these scenarios introduce a new quantum number, which is conserved, and therefore, the lightest new particle will be stable. Models having viable dark matter candidates typically predict the lightest particle to be neutral and non-colored, due to

cosmological constraints [6]. However, depending on details of the model, higher mass particles may also exist in stable or metastable states. In this paper supersymmetric and extra dimensional models are considered as examples of models predicting HSCPs.

2.2.1 Supersymmetric Models

As mentioned above, the Standard Model harbors a flaw known as the hierarchy problem, coming about because of the two different fundamental energy scales, the electroweak scale and the Planck scale. The SM requires that the Higgs field have a nonzero vacuum expectation value (VEV) at its minimum value; this is the "Mexican hat-shaped" property of the field. The VEV $\langle H \rangle$ can be determined from measurements of the W and Z boson masses and the fundamental charge, and is about 253 GeV. Since $\langle H \rangle = \sqrt{-m_H^2/2\lambda}$, $m_H^2 \sim -(200\text{GeV})^2$. But when higher-order Feynman diagrams as corrections to the Higgs mass-squared are taken into account, a problem occurs. In calculating these corrections, one introduces a high-momentum cutoff term for the loop integral. This term grows quadratically with the cutoff scale energy, and if that scale is chosen to be the Planck scale, as is typical, the correction to the Higgs mass-squared becomes many times larger than the mass-squared itself. This effect propagates to the Higgs VEV, and since all SM particles obtain mass via the Higgs VEV, all particles are affected by this enormous correction, which is problematic if one doesn't want to "fine-tune" by hand.

There are a number of possible solutions to this conundrum, but one of the most appealing is to arrange a symmetry such that all the correction terms cancel each other out. This is indeed the case in supersymmetry, in which operators are defined which turn fermionic states into bosonic ones, and vice versa. Each boson has a fermion counterpart (and vice versa) called a superpartner, and the superpartners form supermultiplets. Supersymmetry (SUSY) thus predicts the existence of at least one new particle for each particle in the SM [4]. Depending on the details of the model, some of these particles may be HSCPs. Several supersymmetric models with HSCPs are outlined in the following sections.

Another interesting property is gauge coupling unification. This can occur in SUSY models when, using the renormalization group, the values of the electroweak and strong coupling constants become equal at an energy scale of about 10^{16} GeV. Such a unification

is taken as a desirable feature, providing a "hint" favoring a grand unified theory [4].

Minimally Supersymmetric Standard Model

Because superpartners to SM particles have not been detected thus far, supersymmetry must be broken at some energy. Similar to electroweak symmetry breaking in the SM, where the gauge and Yukawa couplings dictate the masses of the bosons and fermions, the method of SUSY breaking is important to determining sparticle masses [7]. Typically, the gravitational interaction is thought to play a role similar to that of the gauge/Yukawa interactions. However, it is generally not possible to introduce tree-level couplings directly. Instead, the SUSY-breaking sector couples only to a messenger sector, which in turn couples to the observable particles and sparticles. The SUSY-breaking scale F, the Planck scale (thought to be related to quantum gravity effects), and the superpartner masses M_{SUSY} are related by $M_{SUSY} \sim F/M_P$ [8][9]. If M_{SUSY} is to be $\sim$ 1 TeV, $F \sim 10^{11}$ GeV. Usually, to avoid proton decay, R-parity conservation is invoked, where $R = (-1)^{3B+L+2S}$ [10]. Since R distinguishes between SM and SUSY particles (-1 for SUSY, +1 for SM), the lightest supersymmetric particle (LSP) is stable. In the minimally supersymmetric standard model (MSSM), all SUSY-breaking interactions are included, and the LSP can be a neutralino ($\tilde{\chi}^0$), stau ($\tilde{\tau}$), or gluino ($\tilde{g}$). One intriguing case occurs when a neutralino is the LSP and a dark matter candidate, combined with a small mass difference between it and the top squark ($\tilde{t}$) in the role of next-to-lightest supersymmetric particle (NLSP). The lightest chargino can be kept heavy enough so that only $\tilde{t}_1 \to c\tilde{\chi}^0_1$ occurs. Then the $\tilde{t}_1$ may have a long lifetime and is thus an HSCP candidate [6]. Stop production occurs primarily due to the coupling of the stop to the gluon, regulated by the stop mass and the strong coupling constant [11].

Note that in general, the MSSM adds more than one hundred parameters to the SM. Assuming a particular SUSY-breaking mechanism reduces this number, but the parameter space is still unmanageably large. A conference known as the Snowmass Workshop identified a number of benchmark scenarios warranting experimental exploration [12]. Some of the resulting points in the MSSM parameter space are used to guide parts of this analysis, as will be detailed below.

Gauge-mediated Supersymmetry Breaking

In gauge-mediated supersymmetry breaking (GMSB), a different SUSY-breaking approach is pursued. Instead of the gravitational interaction's providing the so-called "messenger scale" of the model, SM gauge interactions are used instead. This has the advantage of suppressing flavor violations that arise in other models, along with divorcing gravity from the fundamental phenomenology so that one does not have to think about quantum gravity in exploring the model [7]. In GMSB, the gravitino is usually the LSP, so the NLSP is naturally long-lived, as it must decay gravitationally. In most areas of parameter space, the NLSP is a stau [6]. The stau can be produced directly via a virtual γ or Z, and it can also be the result of the decay of heavier sparticles.

Split Supersymmetry

In split supersymmetry, the hierarchy problem is discarded as a guiding theoretical principle, and instead the SUSY-breaking scale is taken to be much higher than the EW scale $\sim$ 1 TeV. The masses of the scalar particles, e.g. squarks, are then close to this higher energy, whereas the fermions, e.g., gluinos, have masses close to the EW scale due to their observing chiral symmetry. This has the effect of suppressing a number of problems with conventional SUSY theories, such as flavor violations, a heavy Higgs boson, and non-negligible CP-violating phases. The theory preserves gauge coupling unification and predicts a Higgs boson of mass $\sim$ 120-150 GeV, experimentally preferred over a heavier Higgs. Since the squark masses are so large, and the gluino decays via virtual squarks to the lightest SUSY particle (plus either a gluon or two quarks) the gluino has a long lifetime, which can vary from microseconds to $\sim 10^{10}$ years depending on its mass and the value of the SUSY-breaking scale [13][14]. A plot of the gluino lifetime vs. scalar mass for several gluino masses is shown in Figure 2.3. This long-lived gluino is the key experimental prediction of the model and one that should be readily observable. The gluino can be pair-produced at the LHC via gluon fusion as in $g + g \rightarrow \tilde{g} + \tilde{g}$. The contribution to the production cross section from other processes is quite small [11].

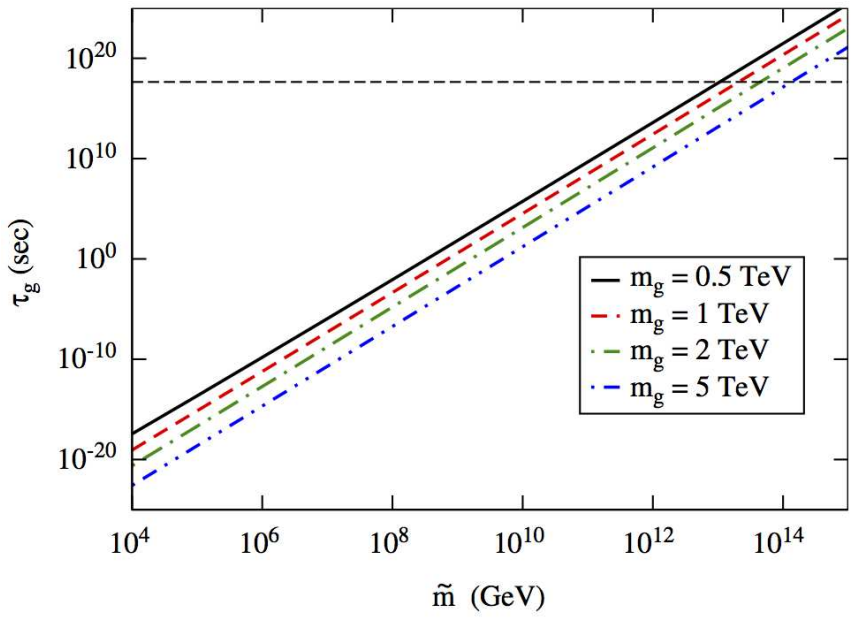

Figure 2.3: Gluino lifetime vs. mass of scalars for several gluino masses. The horizontal dashed line marks 14 Gyr, the age of the universe [6].

2.2.2 Kaluza-Klein Universal Extra Dimensions

In the universal extra dimensions model (UED), all gauge fields and particles are free to roam in a "bulk" of higher dimensional spacetime $D = 3 + \delta + 1$, where δ is the number of extra dimensions. These dimensions are usually taken to be compactified on a scale of $R \sim 1/\text{TeV}$. For each SM particle, there is a matching Kaluza-Klein (KK) state with the same spin and quantum number, whose mass is given by the relation $m_n \sim \sqrt{m_0^2 + n^2/R^2}$, where n is the energy level and m_0 is the SM particle mass [15][11]. In the D-space, momentum is conserved due to translational invariance, leading to conservation of KK parity $(-1)^n$, implying that the lightest KK particle (LKP) is stable. In the minimal universal extra dimensions (MUED) model considered here, $\delta = 1$. One case where an HSCP can occur in the MUED is when a KK photon is the LKP and the mass difference between the KK photon and KK lepton such as the KK μ has mass less than the SM lepton. Then the decay can only occur via a virtual W boson as in $\mu^{(1)} \rightarrow \gamma^{(1)} + \nu_\mu^{(0)} + \nu_e^{(0)} + e^{(0)}$ (superscripts indicating KK level, 0 indicating

an SM particle), and the lifetime of the KK muon is greater than that of the SM muon [16]. But for this case the parameter space is very small, such that only a KK τ that is right-handed with mass $\sim$ 300 GeV could be an HSCP. The cross section for direct KK $\tau\bar{\tau}$ production in this scenario at the LHC is about 20 fb. A KK τ could also be produced as a decay product from a more massive KK particle, but the cross section is lower, on the order of 5 fb [11].

2.3 HSCP Interactions with Matter

There are two basic classes of HSCPs: those that are lepton-like, such as the stau and KK lepton, and those that are strongly interacting, such as the gluino and stop. The lepton-like particles should behave like heavy muons, mainly interacting in the detector through ionization. The hadronizing particles, which are colored, form bound states with SM quarks or gluons known as R-hadrons; for example, R-mesons, R-baryons, and R-glueballs.

The R-hadrons present some experimental difficulties due to their interactions with detector materials. A graph of the nuclear interaction energy loss per interaction length for the R-hadrons is shown in Figure 2.4 for several hadronic interaction models. As shown, the energy loss is a few GeV per hadronic interaction, as the HSCP in the R-hadron acts only as a spectator in the interaction. Therefore for R-hadrons, the dominant energy loss mechanism is ionization, just as it is for the lepton-like particles.

However, there is an additional effect of these interactions: the possibility of the R-hadron's charge to become neutral or flip from positive to negative and vice versa via the exchange of quarks. A single R-hadron can even change charge multiple times as it travels from the inside to the outside of the detector. An example of the effect of such charge flipping on the R-hadron track is depicted in Figure 2.5. A recent study, implementing another hadronic interaction model, looked at the charges of R-hadrons after traversing 2 m of iron, a thickness corresponding to the amount of material in front of the muon system for a typical collider detector [19]. The study showed that gluino and sbottom R-hadrons are most likely to emerge from the material as neutral. This would make it difficult to detect such an R-hadron in the muon system.

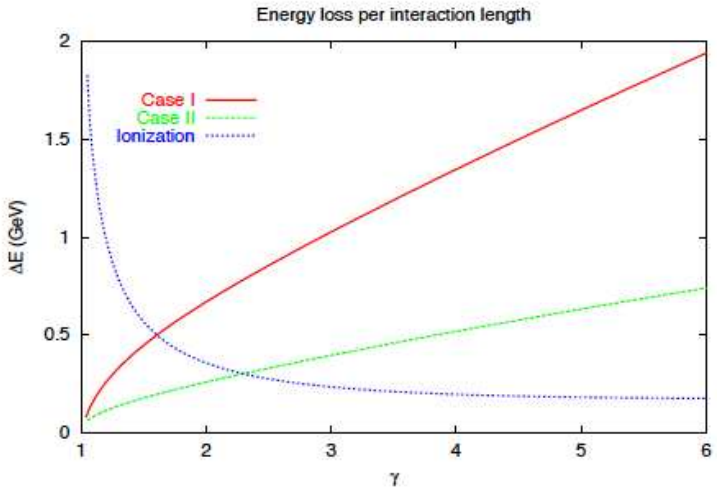

Figure 2.4: Hadronic energy loss per interaction length of R-hadrons vs. $\gamma = (1 - \beta^2)^{-1/2}$. Two different hadronic interaction models are used, as indicated by Case I and Case II [17].

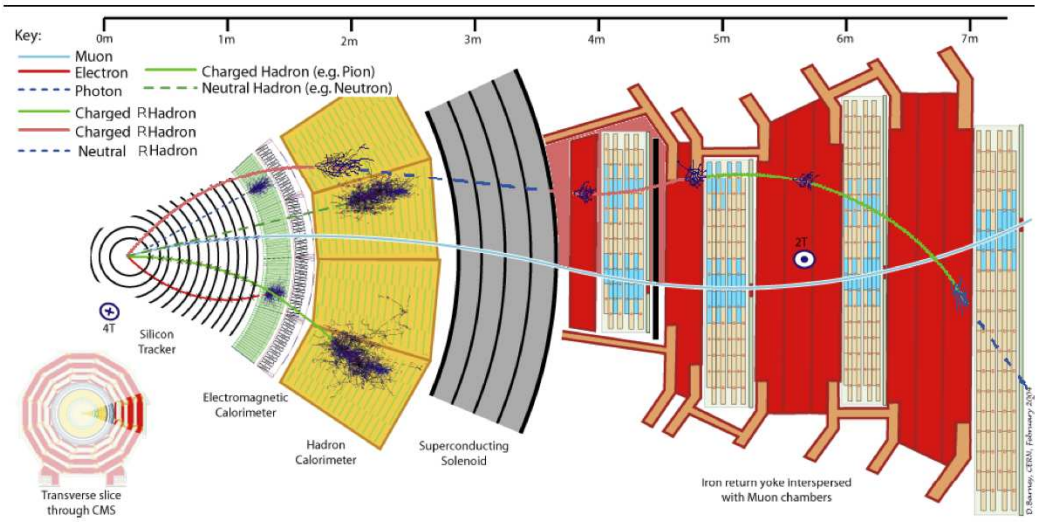

Figure 2.5: Behavior of R-hadrons, which can flip charge, in the CMS detector compared to other particles [18].

Therefore, experimental techniques independent of the muon system should be used at least in addition to those that require it.

2.4 HSCP General Properties

An HSCP is expected to have high mass, high momentum, and should travel ∼10 m before decaying due to its long lifetime [11]. These characteristics are exploited in HSCP searches to separate the signal from Standard Model particles. In particular, a slow-moving massive particle like an HSCP should have a high specific ionization and a long time of flight. From each of these the speed $\beta = v/c$ of the particle can be calculated. Both lepton-like and hadronizing HSCPs will leave a track in the inner tracking system, from which the momentum can be measured. Combining the momentum and β, the mass of the particle can be determined. This will be examined in more detail in Chapter 7.

Theoretical cross sections for the different models considered are shown in Table 2.1 for 7 TeV center-of-momentum energy. For the lepton-like GMSB stau, the cross section is computed using ISASUGRA version 7.69 [20], while for the stops and gluinos, the cross section is computed using PROSPINO [21] at next-to-leading-logarithmic order [22]. Both stops and gluinos are treated as stable and are directly pair produced, which is a model-independent process at leading order, the particle mass being the sole important parameter. For the lepton-like HSCPs, direct pair production can occur but in general decays from heavier SUSY particles have a higher cross section. The GMSB stau is generated using ISASUGRA, and two points on the SPS Snowmass [12] line 7 are selected as benchmarks. The mGMSB parameter values for the two SPS points are:

- $\tilde{\tau}(156)$: $N = 3$, $\Lambda = 50000$ GeV, $M = 100000$ GeV, $\tan\beta = 10$, $sign(\mu) = 1$, $c_{grav} = 10000$
- $\tilde{\tau}(247)$: $N = 3$, $\Lambda = 80000$ GeV, $M = 160000$ GeV, $\tan\beta = 10$, $sign(\mu) = 1$, $c_{grav} = 10000$

The squark and gluino masses in these scenarios are 1.1 and 1.7 TeV, for the 156 GeV and 247 GeV staus, respectively. To add a few more stau mass points, the Λ parameter

Model	**Mass (GeV)**	σ **(pb)**
GMSB $\tilde{\tau}$	100	1.3
GMSB $\tilde{\tau}$	200	1.2E-2
GMSB $\tilde{\tau}$	308	9.8E-4
GMSB $\tilde{\tau}$	432	1.4E-4
GMSB $\tilde{\tau}$	494	6.2E-5
Split SUSY $\tilde{g}$	400	1.1E1
Split SUSY $\tilde{g}$	600	6.9E-1
Split SUSY $\tilde{g}$	800	7.2E-2
Split SUSY $\tilde{g}$	1000	9.9E-3
Split SUSY $\tilde{g}$	1200	1.5E-3
MSSM $\tilde{t}$	200	1.3E1
MSSM $\tilde{t}$	400	2.2E-1
MSSM $\tilde{t}$	600	1.3E-2
MSSM $\tilde{t}$	800	1.1E-3

Table 2.1: Selected HSCP production cross sections, from ISASUGRA [20] ($\tilde{\tau}$) and PROSPINO [21] ($\tilde{t}$, $\tilde{g}$). Center-of-momentum energy is taken as 7 TeV.

is varied. In this region of parameter space, the pair production cross section of the heavy squarks and gluinos is at least one order of magnitude higher than that of staus.

To examine some of the kinematic properties of the HSCPs, different signal models are generated using Monte Carlo techniques. For the top squarks or stops ($\tilde{t}_1$), the MadGraph matrix element generator [23] is used as a first step, with the results fed into PYTHIA [24] to perform the showering and hadronization. In the latter program, initial and final state partons are allowed to branch into pairs several times over, creating a parton shower, and then the partons are grouped into colorless hadrons using phenomenological models. Typically an underlying event is added, i.e., interactions of beam particles other than those involved the hard scatter of primary interest [25]. In this case, the MLM algorithm is used in order to match parton showers from PYTHIA generated from softer processes to the hard partons generated at the matrix element stage by MadGraph [26]. Gluinos ($\tilde{g}$) are produced using PYTHIA for both generation and showering. Distributions of the velocity β, transverse momentum P_T, and pseudorapidity η for a few gluino, stop, and stau models are shown in Figure 2.6. The

transverse momentum spectrum gets harder as the particle mass increases, and in general production is central in η. Plots of the velocity β vs. the pseudorapidity η for two stop and two stau masses are shown in Figures 2.7 and 2.8. It can be observed from these Figures that in general, HSCP with high β are produced outside of the central η region, except for the lightest stau.

2.5 Comparison to Tevatron Experiments

Searches for HSCPs were conducted at the Tevatron located at Fermi National Accelerator Laboratory in Batavia, Illinois. The Collider Detector at Fermilab (CDF) searched for HSCPs with a tracker-based time-of-flight strategy. Events that had a muon with $P_T > 20$ GeV from the primary vertex along with a second muon or another particle were selected. The data was split into a signal sample where both particles have $P_T >$ 40 GeV and a control where both particles have 20 GeV $< P_T <$ 40 GeV. The control was used to model backgrounds in the signal sample. The theoretical model here was stop production. A single candidate with mass > 100 GeV was found. This was consistent with background predictions, so a lower mass limit of 240 GeV was set using the next-to-leading order cross section [29]. The results are shown in Figure 2.9.

A search for staus and charginos was conducted at the D0 detector, also at the Tevatron. These are pair-produced so selected events contain two muons. Most of the time the two are produced back-to-back. The average speed of the candidates was measured using information from the muon system and used to calculate a significance: $(1-\beta)/\sigma_{speed}$, where σ_{speed} is the resolution on the speed. Massive particles should have a large significance value, as opposed to muons, which should be centered about zero. This was used along with the reconstructed mass to make cuts. Six different masses of staus were considered, and the observed events were consistent with background for each. The same cuts were applied to the charginos, which are kinematically similar. The stau analysis cannot improve on limits set by LEP, while a chargino lower mass limit of 174 GeV can be set. The D0 results are shown in Figure 2.10.

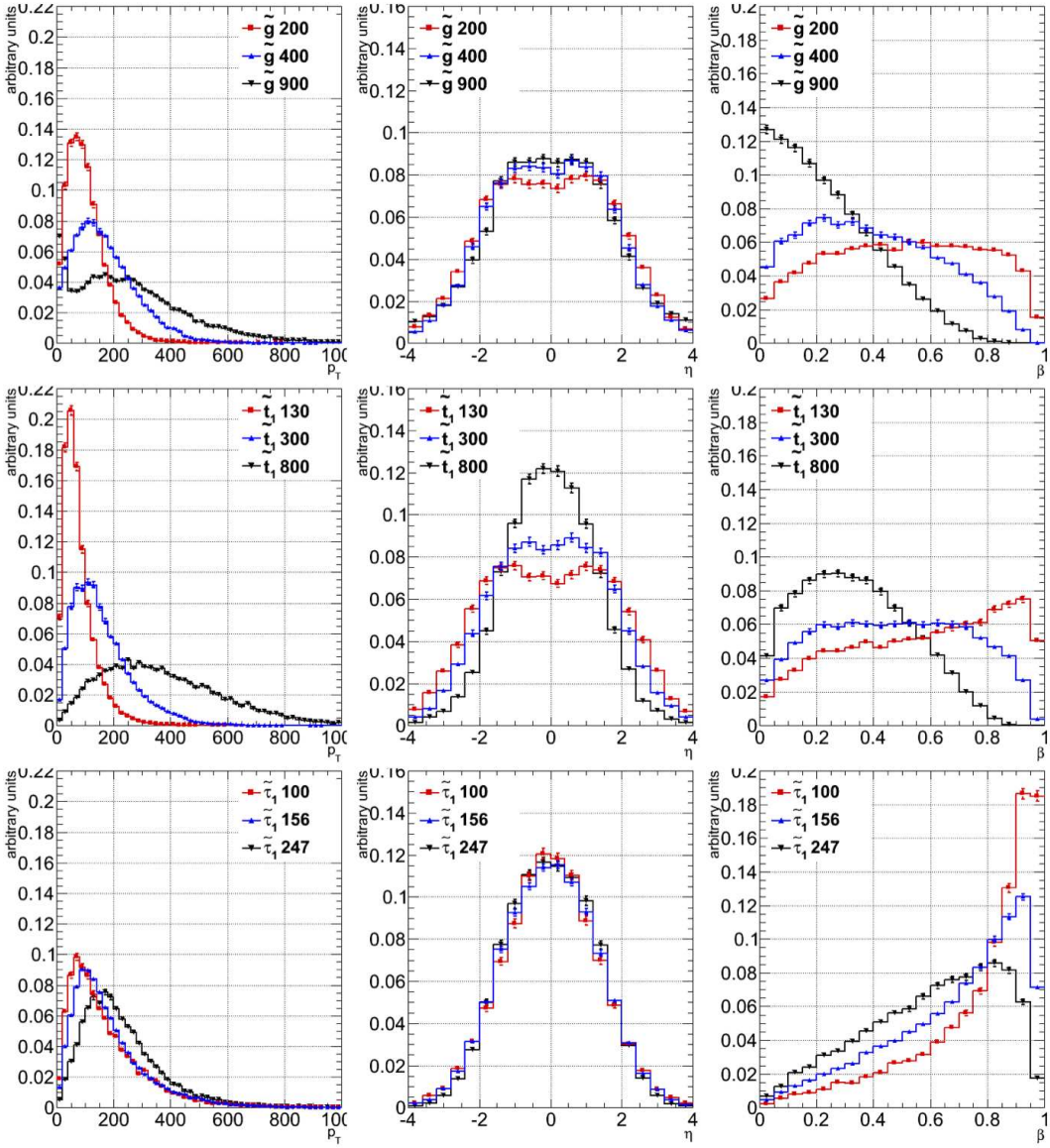

Figure 2.6: Distributions of the transverse momentum, pseudorapidity η, and velocity β. Models illustrated are gluinos (top), stops (middle), and staus (bottom), and several masses are considered for each [27].

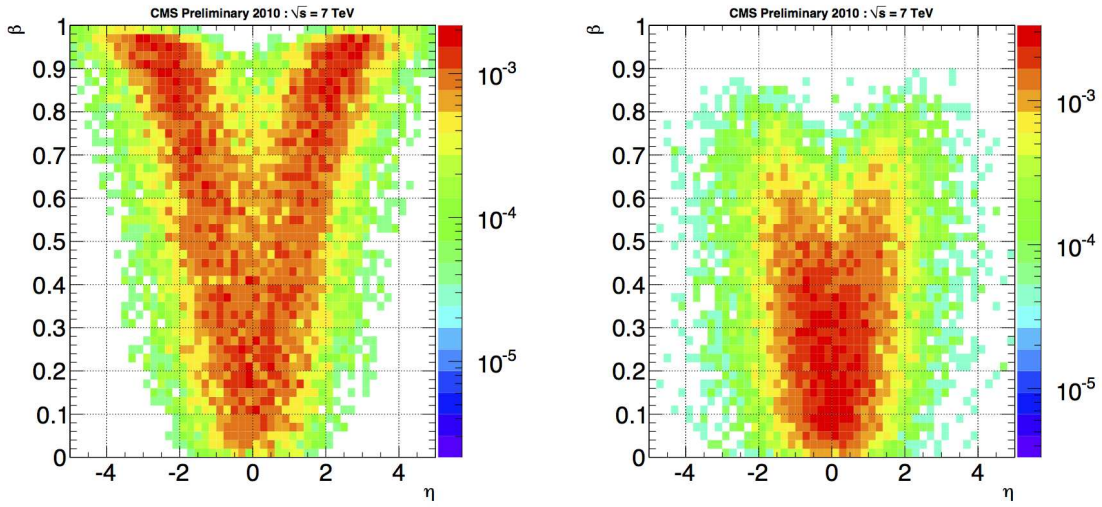

Figure 2.7: Velocity (β) vs. pseudorapidity (η) for two stops, of mass 130 GeV (left) and 800 GeV (right) [28].

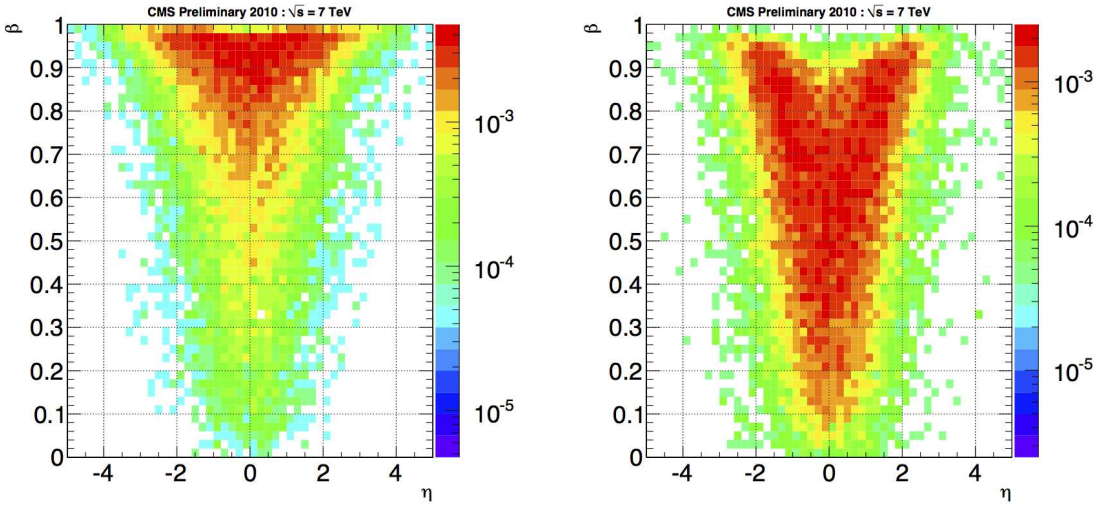

Figure 2.8: Velocity (β) vs. pseudorapidity (η) for two staus, of mass 100 GeV (left) and 247 GeV (right) [28].

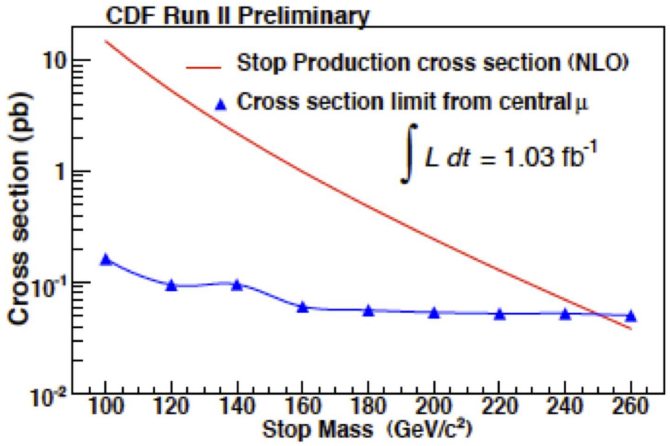

Figure 2.9: Theoretical cross section and observed cross section for stops plotted by mass. A lower mass limit of 240 GeV is set [29].

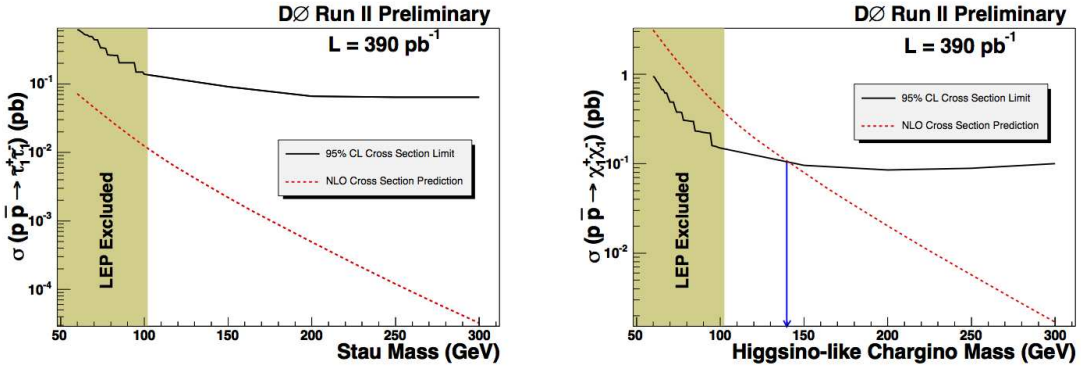

Figure 2.10: Observed (solid line) and calculated (dotted line) cross sections for stau and Higgsino-like chargino production as a function of mass. A lower limit on the chargino mass (both Higgsino- and wino-like) of 174 GeV is set [29].

Chapter 3

The LHC and the CMS Detector

The Large Hadron Collider (LHC) is a superconducting particle accelerator, located at the CERN lab near Geneva, Switzerland. It is designed to deliver proton-proton collisions at high energy and high luminosity, allowing for a comprehensive search not only for the Higgs boson, but also for signs of other new particles. Higher precision measurements of Standard Model parameters will also be undertaken. Capturing the collision products are massive detectors, which are situated in underground caverns along the beam line. The Compact Muon Solenoid (CMS) is one of four main detectors at the LHC. Two of the four, LHCb and ALICE, are specialized for particular types of measurements, while the other two, CMS and ATLAS (A Toroidal LHC ApparatuS), can perform a wide variety of measurements and searches [30] [31] [32].

3.1 Large Hadron Collider

The Large Hadron Collider (LHC) [33] was constructed in the 26.7 km circumference tunnel used for the CERN LEP machine, lying between 45 m and 170 m underground. Traversing the Swiss-French border, the tunnel consists of eight straight sections and eight arcs and is slightly inclined towards *Lac Léman*, or southwest. A diagram of the LHC layout is shown in Figure 3.1. There are eight possible interaction points where the beams may cross, but only four of these are used, one for each of the four main LHC experiments. Figure 3.2 shows a photo taken from the Jura Mountains in France featuring *Lac Léman* and the Alps in the background. Since the LHC collides protons

with protons, there are two separate rings with counter-rotating beams contained in a single magnet structure. The main goal of the LHC is to detect the Higgs boson, thereby lending additional support to the Standard Model. However, the high center of momentum energy allows the creation of other particles with masses on the order of 1 TeV, a key prediction of many models of new physics beyond the Standard Model, including Heavy Stable Charged Particles (HSCP).

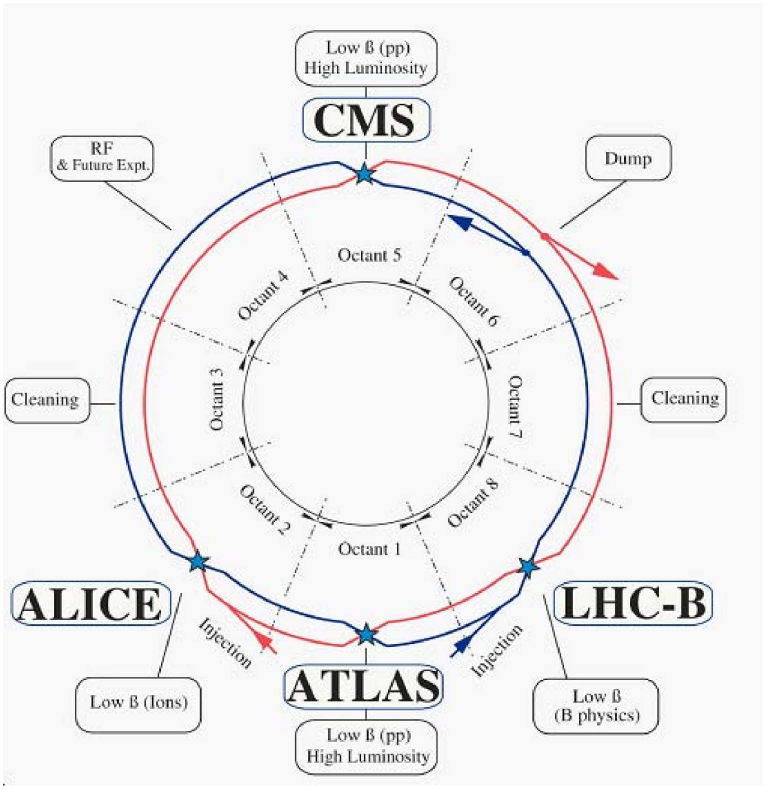

Figure 3.1: The layout of the LHC with the interaction points of the four main experiments shown [33].

3.1.1 Design Considerations

The LHC event rate is defined as

$$N_{event} = L\sigma_{event} \tag{3.1}$$

Figure 3.2: Photo of the Geneva area, with the LHC ring superimposed in red. *Lac Léman* and the Alps are visible [34].

where L is the luminosity and σ_{event} is the cross section of the event. The luminosity for a Gaussian beam profile is given as

$$L = \frac{N_b^2 n_b f_{rev} \gamma_r}{4\pi \epsilon_n \beta^*} F \tag{3.2}$$

where N_b is the number of particles per bunch, n_b is the number of bunches per beam, f_{rev} is the revolution frequency, $\gamma_r = \sqrt{1-\beta^2}$ is the relativistic gamma, ϵ_n is the transverse beam emittance, β^* is the beta function at the beam collision point, and F is the luminosity reduction factor due to the crossing angle at the collision point. The factor F arises from a purely geometric effect, which assuming round beams, equal beam parameters for both beams, and $\sigma_z \ll \beta$ is given by

$$F = \left(1 + \left(\frac{\theta_c \sigma_z}{2\sigma^*}\right)^2\right)^{-1/2} \tag{3.3}$$

where θ_c is the full crossing angle at the collision point, σ_z is the root-mean-square bunch length, and σ^* is the transverse root-mean-square beam size at the collision point. Searching for rare events, i.e., those with low σ_{event}, requires maximizing the luminosity, which implies a high beam intensity. The LHC design peak luminosity is $10^{34}\text{cm}^{-2}\text{s}^{-1}$ for proton-proton collisions. Taking the proton-proton total cross section of about 70 mb, peak instantaneous luminosity corresponds to just under 10^9 events per second. In addition, an average of 20 inelastic collisions will occur at each beam crossing, i.e., every 25 ns, giving rise to 1000 charged particles. This leads to an experimental challenge of triggering on and reading out only the "interesting" events, as will be discussed below. The peak luminosity performance is intended for ATLAS and CMS. LHCB (B physics) and TOTEM (small-angle inelastic scattering) operate at lower luminosities, and in the case of TOTEM, fewer bunches [31] [35]. The LHC can also accelerate and collide heavy ions such as lead. ALICE is purpose-built to take maximum advantage of the ion beams, but ATLAS and CMS participate as well.

The high peak luminosity in proton-proton mode requires a high beam intensity, which means that antiproton beams cannot be used. This is unlike the Tevatron at Fermilab near Chicago, Illinois, USA, which collides protons and antiprotons [36]. Colliding protons necessitates two separate proton rings with separate vacuum chambers and magnetic fields. Space constraints inside the tunnel led to the adoption of a single

magnet structure containing both beam pipes inside it. Figure 3.3 shows a photo of an assembled dipole, with the two beampipe structure visible. To achieve the nominal center-of-momentum (COM) energy of 14 TeV, the LHC makes use of superconducting magnets, cooled by superfluid liquid helium to below 2 K, for a nominal magnetic field above 8 T. The LHC has 1232 main dipole magnets for beam steering, each about 16.5 m long, and other magnets to correct the orbits and focus the beam, such as quadrupoles. Table 3.1 shows some of the LHC design parameters. Table 3.2 shows some of the collision parameters at the CMS interaction point.

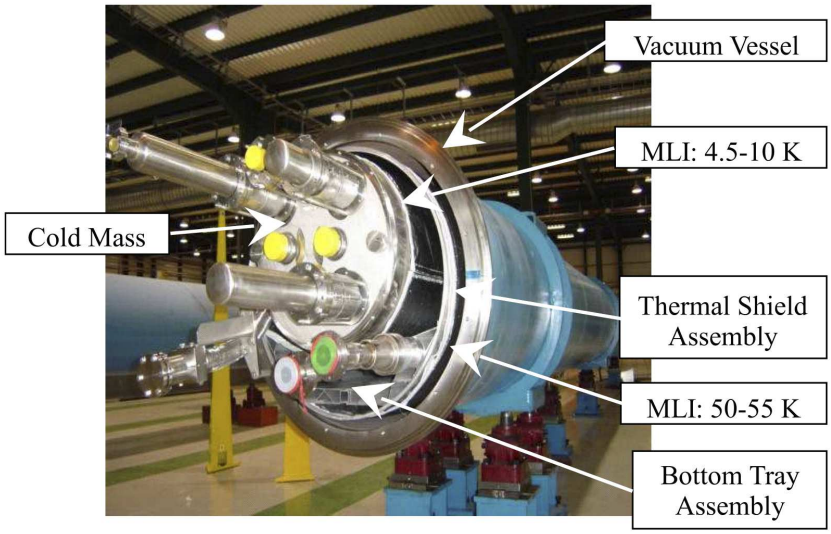

Figure 3.3: Photo of an assembled LHC dipole, with the two beampipes visible in yellow at the center. Some parts of the assembly, such as the multilayer insulation (MLI) are labeled [33].

3.1.2 Injection Chain

The LHC was designed to use the existing accelerator chain at CERN. Figure 3.4 is a diagram of the acceleration process for protons and heavy ions. The full chain must meet the challenges of the LHC design, which means bunches with low emittance and high intensity, spaced at 25 ns intervals. The beams must also be suitable for transferring

	Value	**Unit**
Luminosity	10^{34}	$\mathrm{cm}^{-2}\mathrm{s}^{-1}$
Proton energy	7	TeV
Dipole magnetic field at 7 TeV	8.3	T
Stored energy in beams	362	MJ
Normalized transverse emittance	3.75	μm
Bunch spacing	24.95	ns
Bunch length σ_z	7.5	cm
Number of bunches	2808	
Protons per bunch	$1.15\mathrm{x}10^{11}$	

Table 3.1: Selected LHC Design Parameters for pp collisions [33].

	Value	**Unit**
$\beta^* = \beta-$value at IP	0.55	m
RMS beam radius at IP σ^*	16.7	μm
Crossing angle (full) θ_c	285	μrad
Luminosity lifetime	15	hr
Collisions per crossing	$\sim$20	
Geometric luminosity reduction factor F	0.84	

Table 3.2: Selected CMS collision parameters [37].

between injectors, e.g., small longitudinal emittance, and satisfy many other requirements. Starting with the linear LINAC2 accelerator, the protons attain 50 MeV kinetic energy. Then in the proton synchrotron booster, this increases to 1.4 GeV. Exiting the proton synchrotron (PS), the protons are at 25 GeV, and finally, the super proton synchrotron (SPS) brings them up to 450 GeV for injection into the LHC. The PS had to undergo a series of upgrades to various components and be equipped with new radio frequency acceleration systems in order to increase the bunch intensity and change the bunch spacing. After injection into the LHC, the protons are accelerated over a period of 20 minutes to nominal energy, as the magnets ramp up to full field. A 400 MHz system located at Point 4 captures and stores the beam using superconducting cavities, each with a field strength of 5.5 MV/m, or 2 MV of accelerating voltage [33].

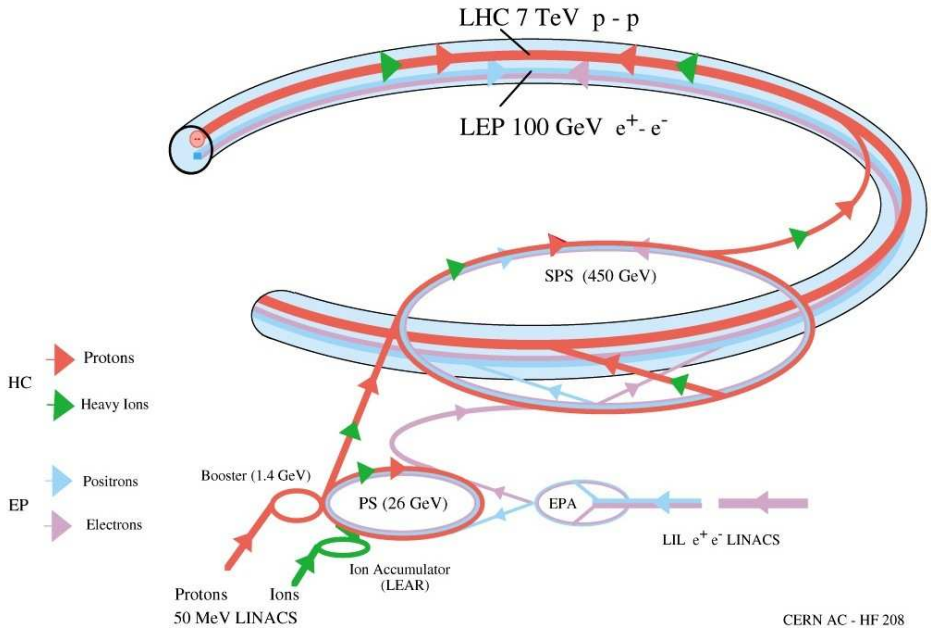

Figure 3.4: The LHC injection chain for protons and heavy ions (HC). Also shown is the former LEP chain for electron-positron collisions. Diagram adapted from [38].

3.1.3 Commissioning

The LHC was scheduled to start up in September 2008. Initial results were promising. However, during a high-current dipole magnet test, a "resistive zone" developed in the

interconnect bus bars, which caused failure of the interconnect and electrical arcing, damaging the helium enclosure. The resulting shock wave triggered by the release of the pressurized helium damaged a 400 m long region of the LHC magnet and vacuum system. Thirty-nine dipole magnets and 14 quadrupole magnets had to be completely replaced. Over 200 magnet interconnects needed partial or full repairs, and 4 km of beam pipe had to be cleaned. In addition to adding helium pressure relief values, the magnet protection system was upgraded and the resistance of each bus bar interconnect was measured. Due to the limited precision of the measurement, only significant outliers could be detected and fixed, and it was likely that interconnects with higher resistance than optimal remained in the machine. It was therefore decided to run the LHC at a lower energy to limit the amount of current flowing in the interconnects until they can be measured with higher precision. The operating energy was set to 3.5 TeV per beam for 2010 and 2011. In November 2009, after months of repairs, beam was circulating in the machine. On March 30, 2010, the LHC produced the first collisions at 7 TeV center-of-momentum energy for a worldwide media audience [39]. After this success, over the course of 2010 many machine parameters were commissioned and tuned, including higher intensity bunches and lower β^*. The end of the 2010 proton run featured 2.07×10^{32} $\mathrm{cm}^{-2}\mathrm{s}^{-1}$ instantaneous luminosity, with 368 bunches per beam, 348 colliding in ATLAS and CMS, and about 6 pb^{-1} delivered in one day. In 2011, the LHC came back online quickly, achieving 10^{32} $\mathrm{cm}^{-2}\mathrm{s}^{-1}$ peak luminosity in March, and went on to accumulate the integrated luminosity goal for the entire year before July. The β^* was 1.5 m in ATLAS and CMS. The LHC moved to 50 ns spacing of bunches and the number of bunches was gradually increased to 1380. Reducing the emittance and increasing bunch intensity yielded an instantaneous luminosity of 2.4×10^{33} $\mathrm{cm}^{-2}\mathrm{s}^{-1}$ with over 90 pb^{-1} delivered in one day [40]. A plot of the integrated luminosity over time for CMS is shown in Figure 3.5. The luminosity is measured with the forward calorimeters of CMS [41].

3.2 The CMS Detector

Similar to the detectors located at the Tevatron, the Compact Muon Solenoid (CMS) is built as a "4π" structure completely surrounding the collision region, with an inner

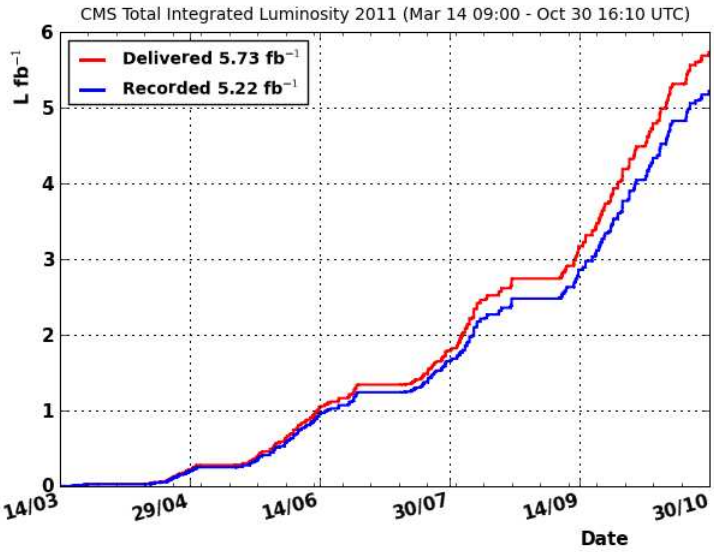

Figure 3.5: LHC delivered and CMS recorded luminosity vs. time [42]

tracking system on the inside and a large muon detector on the outside [43]. It is located underground at interaction point 5, near Cessy, France. Over 3500 scientists from more than 40 countries participate in the operation of the detector and analysis of its data. CMS was designed with the search for the Higgs boson in mind, but it has features that make it useful for other tests of the Standard Model and many searches for physics beyond the standard model. A photo of the CMS Detector in its underground cavern is shown in Figure 3.6.

3.2.1 Detector Requirements

In order to search for the Higgs boson, supersymmetry, new particles, and to test the standard model, the detector must be able to identify and measure particles produced in the LHC collisions. The basic requirements are: a tracking system that allows excellent momentum resolution and reconstruction efficiency of charged particles, in addition to accurate measurement of interaction vertices; an electromagnetic calorimeter with excellent energy and position resolution and large geometric coverage for photons and

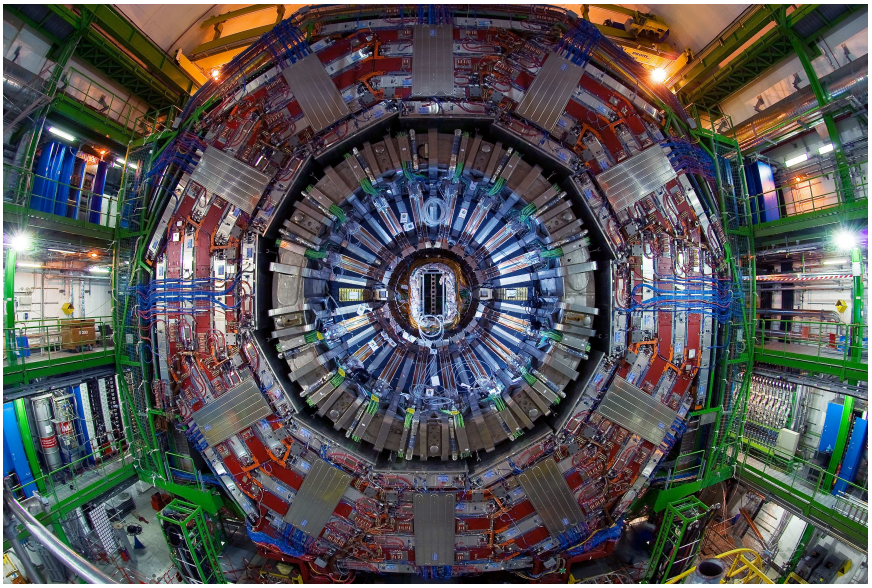

Figure 3.6: Photo of the CMS detector in its underground cavern [44].

electrons; a hadronic calorimeter with good energy resolution and even larger geometric coverage to measure jets and missing energy; and a muon system that can identify and measure the momentum of muons with high precision over a large momentum range. In addition, the high rate and intensity of the LHC imposes challenges for the trigger and readout system. Overall, CMS consists of subdetectors arranged in layers surrounding the collision region. Combining the different measurements from each subdetector, the collision products can be reconstructed.

The innermost part of CMS is the 100% silicon tracking system, consisting of pixel and strip layers. Outside of the tracking system are the two calorimeters, the electromagnetic (ECAL), and outside of it, the hadronic (HCAL). All of the above is contained inside the bore of the 3.8 Tesla solenoid magnet. Outside the magnet is the muon system, composed of cathode strip chambers (CSCs), resistive plate chambers (RPCs), and drift tubes (DTs). Close to the beampipe but outside of the muon system lie the very forward calorimeter and the detector from another experiment, TOTEM [35]. A diagram of the detector is shown in Figure 3.7 and some detector parameters are given in Table 3.3. The CMS coordinates used here are defined as follows. With the origin at the collision point, the y-axis points vertically upward and the x-axis points towards

the center of the LHC ring. The z-axis is aligned with the beams and pointed at the Jura mountains, or in the counterclockwise direction, creating a right-handed system. Two angles are also defined, ϕ starting from the x-axis and increasing in the x-y plane, and θ, starting from the z-axis and increasing in the z-y plane. The pseudorapidity is given by $\eta = -\ln(\tan(\theta/2))$ and the transverse energy E_T and momentum P_T are given as $E_T = E\sin(\theta)$ and $P_T = P\sin(\theta)$.

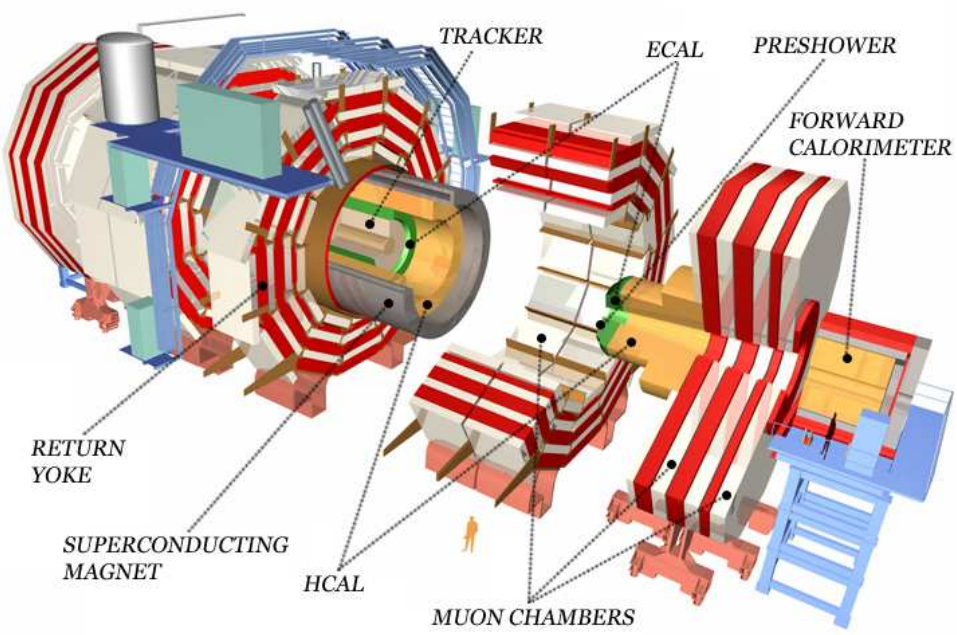

Figure 3.7: The CMS detector (adapted from [42]).

	Value	**Unit**
Total weight	14000	t
Overall length	28.7	m
Diameter	15.0	m
Magnetic field	3.8	T

Table 3.3: Selected CMS detector parameters [37].

3.2.2 Superconducting Solenoid Magnet

The momentum resolution of a charged particle as measured in a magnetic field goes as $1/BL^2$ where B is the magnetic field and L is the radial extent of the tracking detector. Then for a fixed detector size, the magnetic field must be increased to improve the momentum resolution. In particular, the design of the CMS tracker to measure muons at 1 TeV transverse momentum with a resolution of 10% or better necessitates a high magnetic field of about 4 Tesla. Thus, a superconducting magnet is necessary, and in the case of CMS, a solenoid was chosen. In order to minimize energy loss from interactions with detector material, which degrades the calorimeter energy resolution, it was necessary to design a solenoid large enough to house the tracking system and the calorimetry. The CMS solenoid is 6.3 m in diameter, 12.5 m long, and 220 t in mass, with a stored energy of 2.6 GJ and nominal current of about 19 kA. The dimensions are very large compared to previous detector magnets. Returning the magnetic flux is a 10000 t steel yoke. The muon stations are sandwiched in between layers of yoke, and thus, the magnetic field for the muon system, outside the solenoid, is in the opposite direction as the field inside, in the central η region. In this way muons are bent in the opposite direction after passing through the solenoid coil.

3.2.3 Inner Tracking System

The tracking system is designed to measure the momentum of charged particles and reconstruct primary and secondary vertices from collisions. Due to the immense particle flux at the LHC design luminosity, about 1000 charged particles per bunch crossing (25 ns), fast response and high granularity are required. The detector must also be tolerant enough of this high radiation to last about 10 years. These factors led to the adoption of a 100% silicon based system. The tracker features a pixel detector with three barrel layers and a microstrip detector with 10 barrel layers, supplemented by two pixel and 12 strip layers in each endcap. The total amount of silicon used dwarfs that of other experiments, making up 66 million pixels and 11.4 million silicon strips for an area of 214 m^2. A diagram of the tracker layout is shown in Figure 3.8.

Close to the interaction region, pixels must be used to keep the occupancy around 1%. The three barrel pixel layers are cylindrical in shape and are located at 4.4, 7.3 and

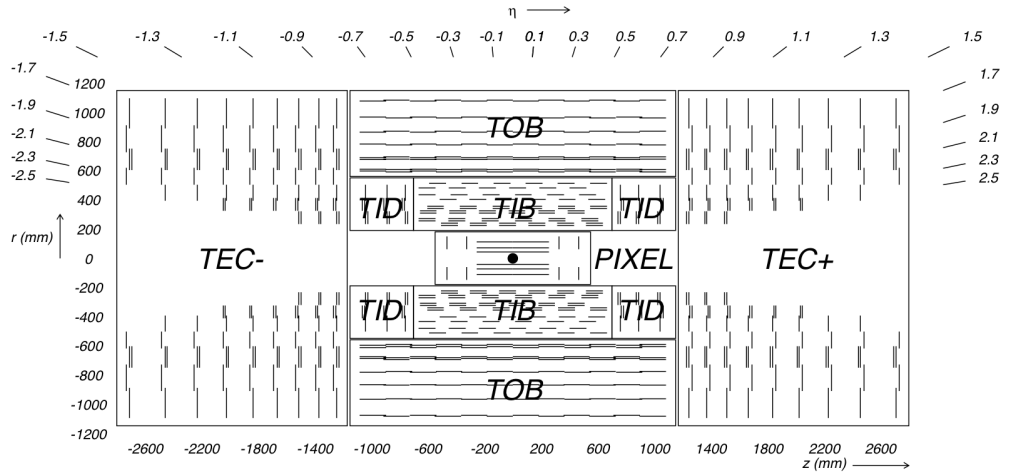

Figure 3.8: The CMS tracker layout, including pixel detector, tracker inner barrel (TIB), tracker inner disk (TID), tracker outer barrel (TOB), and tracker endcap (TEC) [43].

10.2 cm from the interaction point. There are two pixel disks which increase coverage to $|\eta| < 2.5$, and the pixel detector yields 3 spatial measurements for each charged particle, in r-ϕ and z. The pixel size is 100×150 μm^2 in the barrel and forward sections. Outside of the pixels, silicon microstrips with typical sizes of 10 cm $\times$ 80 μm are used, with the strip pitch increasing as the radius increases. Starting closest to the pixel detector, there are 4 barrel layers of strips aligned parallel to the beam axis (TIB) and 3 disks per endcap with strips aligned radially (TID), with the TIB yielding up to 4 r-ϕ measurements (3 in TID). The TIB and TID are situated between 20 and 55 cm away from the interaction point. Outside of the TIB/TID is the tracker outer barrel (TOB) extending to 116 cm in radius and consisting of 6 barrel layers, providing up to 6 r-ϕ measurements. To cover higher η tracks, the tracker endcaps (TEC+/-) extend from 124 to 282 cm in z and 22.5 to 113.5 cm in r. Each TEC has 9 disks consisting of radial microstrips, yielding up to 9 measurements in ϕ-z. Several layers and rings are stereo, containing two strip modules, thus providing measurements of z in the barrel and r in the disks. This layout guarantees about 9 hits in the strip tracker in the full $|\eta| < 2.4$ coverage with at least 4 stereo hits. Figure 3.9 shows the number of hits as a function of η. In general, the strip sensors in the outer region are increased in thickness

to 500 μm from 320 μm in the inner region in order to keep the signal to noise ratio high with longer strip length. The single-cell occupancy at high luminosity is designed to be less than 3% depending on the subdetector [45]. The transverse momentum resolution is expected to be 1-2% for tracks with momentum above 100 GeV in the region of $|\eta|$ <1.6. Though not expressly designed for this purpose, the tracker sensors can also measure the amount of charge deposited by a traversing charged particle. This makes measuring dE/dx possible, a feature that is utilized in the search for Heavy Stable Charged Particles.

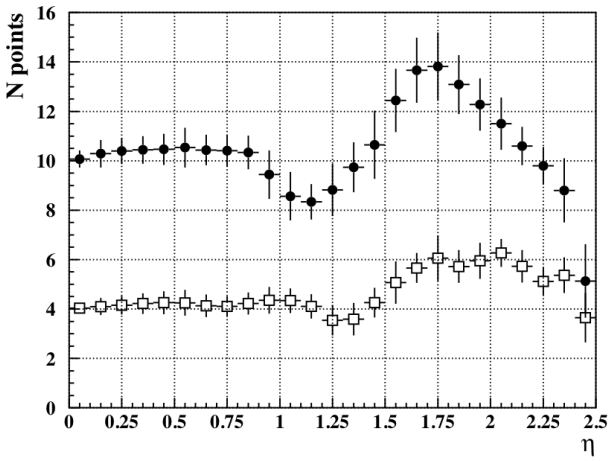

Figure 3.9: Hits in the tracker as a function of η. Open squares represent the number of stereo layers and filled circles show the total number of hits [43].

3.2.4 Electromagnetic Calorimeter

The CMS electromagnetic calorimeter (ECAL) is designed to accurately measure the energy of impacting photons and electrons. To ensure containment of showers from high energy particles, a material of high density must be chosen with a short radiation length and small Molière radius. In addition, using the same material for both absorption and scintillation minimizes unmeasurable energy losses in detector materials. For this reason, lead tungstate ($PbWO_4$) scintillating crystals were chosen to serve as the heart of ECAL, and about 80000 of them are used in total. Lead tungstate has a density of 8.28 g/cm^3, a radiation length of 0.89 cm and a Molière radius of 2.2 cm, allowing

construction of a compact detector, in addition to fast scintillation response, with 80% of the light emitted in 25 ns. One disadvantage is the low light output; roughly 4.5 photoelectrons per MeV are collected in the photodetectors, which in the barrel have a quantum efficiency of about 75% and cover 1/8 the area of the crystal rear face. The crystals are radiation hard, the main effect of irradiation being the formation of color centers which impact the crystal transparency only and not the scintillation mechanism. This damage can thus be tracked and corrected using a laser system.

ECAL has two main sections: barrel (EB), covering $|\eta| < 1.479$ and 360° in ϕ, and endcap (EE), covering $1.479 < |\eta| < 3.0$. A third section, the preshower (ES) is a lead-silicon detector located in front of EE, which is designed to distinguish showers from π^0 decays from those due to a single photon. The overall layout of the ECAL detector is shown in Figure 3.10 while a more geometric view is shown in Figure 3.11. The remainder of this section will focus on EB and EE.

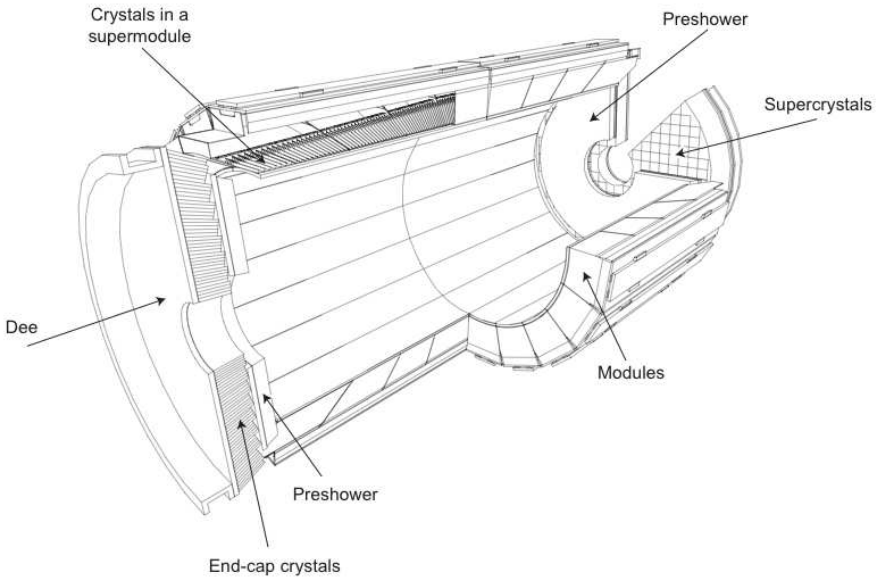

Figure 3.10: Overview of the CMS ECAL layout [43].

The EB is constructed in 36 supermodules of 1700 crystals each, totaling 61200 crystals. Each EB crystal measures approximately 2.2 cm $\times$ 2.2 cm at the front face and is 23 cm long, about 25.8 radiation lengths, allowing excellent energy containment for

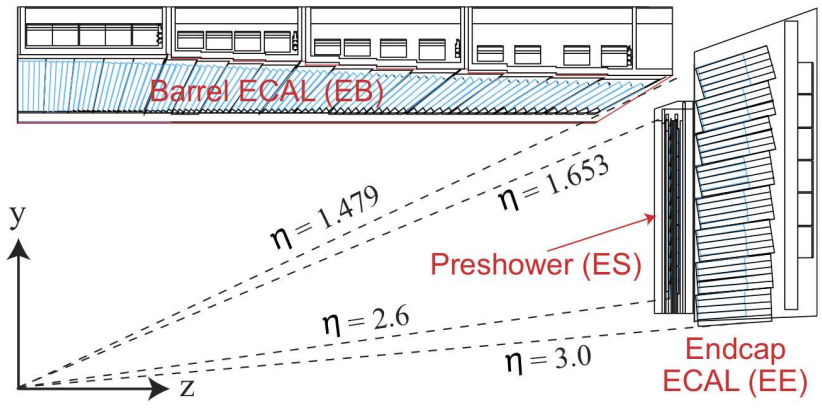

Figure 3.11: Geometric diagram of the CMS ECAL, adapted from [37].

electrons and photon showers. The face area corresponds to 0.0174 × 0.0174 in η-ϕ, with the shape varying slightly with η position. The rear face is 2.6 cm × 2.6 cm at the rear face, giving a truncated pyramid or tapered shape to the crystal as a whole. The crystals are off-pointing with respect to the center of the detector by 3° so that intercrystal gaps do not align with particle trajectories, and their front faces are 1.29 m away from the beam axis. The scintillation light is collected by avalanche photodiodes (APDs) in EB. As the scintillation mechanism and the APD amplification are strongly temperature dependent, a water cooling system is used which keeps the operating temperature at (18 ± 0.050)° C. The APDs are required to be radiation hard, and after testing and screening, are expected to see only an increase in the dark current with irradiation, i.e., an increase in noise. The APD gain directly affects the ECAL energy resolution, and thus the high voltage system must be stable on the order of tens of mV. Operating at a gain of 50 implies a bias voltage between 340 and 430 V. Pairs of APDs with a mean gain of 50 at their operating voltage are mounted on the rear face of each crystal and are read out together.

The EE is built from 5 × 5 crystal units called supercrystals, making up 4 dees (2 per endcap) holding 3662 crytals each. Each dee has 138 standard supercrystals and 18 partial units to refine the shape of the inside and outside edges. The crystal size increases in EE to a front face of 2.862 cm × 2.862 cm with a length of 22 cm, or 24.7 radiation lengths, with a rear face of 3.0 cm × 3.0 cm. The off-pointing angles vary

from 2° to 8°, as the crystals are pointed 1300 mm past the interaction point, nominally 315.4 cm from the crystal front faces with magnetic field applied. For readout the EE uses vacuum phototriodes (VPTs) instead of APDs due to the increased particle flux in their region of coverage. Irradiation leads to an increase in the anode current, i.e., noise, but no other ill effects. The VPT dynode and anode are biased at +600 V and +800 V respectively, and the photocathode is held to ground. As the operating voltages are close to saturation, the voltages do not have to be controlled as precisely as the APD voltages. The VPTs have shown evidence of a rate dependency of the gain, and though this effect is suppressed in the magnetic field, an LED pulser system was incorporated to keep the rate constant.

The ECAL electronics readout is separated into on-detector and off-detector sections. The on-detector section is composed of very front end cards, each connected to up to 5 crystals, and front end cards, each hosting up to 5 very front end cards, or up to 25 crystals in total. Transmission of the data is accomplished via gigabit optical hybrid (GOH) connections running at 800 Mb/s. From the photodetector, the analog signal is preamplified and shaped by a multi-gain preamplifier (MGPA). The MGPA has a shaping time of about 40 ns and outputs three analog signals with gains of 12, 6 and 1. These are digitized in parallel by a 40 MHz 12-bit analog to digital converter (ADC), which selects the highest gain non-saturated signal and outputs the 12-bit digital representation. The data are buffered in the front end cards and transmitted via one GOH to the off-detector trigger concentrator card, which prepares the crystal data for usage in the CMS Level-1 trigger processor. If a Level-1 trigger is fired, anywhere in CMS, the data are transmitted through the second GOH to the off-detector data concentrator card for readout and storage. A third off-detector card, the clock and control system, generates and distributes fast and slow control functions to the very front end and front end cards. A diagram of the on-detector readout process is shown in Figure 3.12.

The main figure of merit from the ECAL is its energy resolution. For energy $<$ 500 GeV, where rear energy leakage is not significant, the resolution can be expressed as

$$\left(\frac{\sigma}{E}\right)^2 = \left(\frac{S}{\sqrt{E}}\right)^2 + \left(\frac{N}{E}\right)^2 + C^2 \tag{3.4}$$

where S is the stochastic term, N is the noise term, C is the constant term, and E

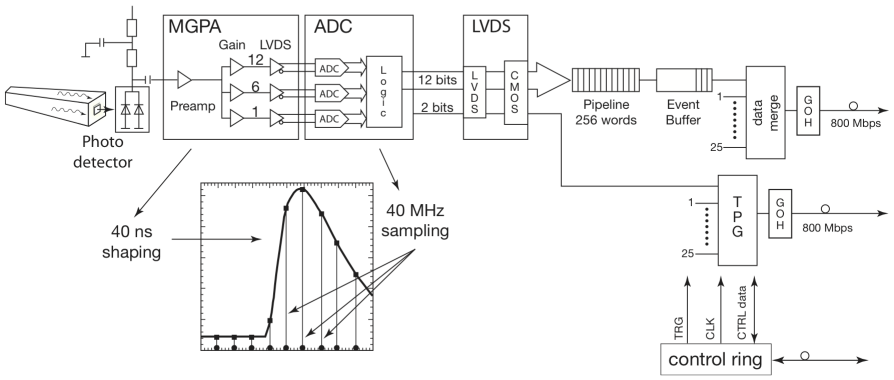

Figure 3.12: Diagram of the CMS ECAL readout chain. First, the signal from the photodetector is preamplified and shaped by the MGPA. Then the highest gain non-saturated signal is selected by the ADC. Finally, the data are buffered and transferred to the off-detector electronics [43].

is the particle energy deposited. The stochastic term arises from photostatistics and fluctuations in lateral shower containment and energy deposited vs. measured in the preshower. The noise term includes electronics and digitization noise, and pileup noise. The constant term includes non-uniformity of light collection, intercalibration errors, and energy leakage from the crystal rear face. The terms were measured from test beam data to be: $S = 2.8\%(\sqrt{\text{GeV}})$, $N = 12\%(\text{GeV})$, and $C = 0.3\%$ [46].

3.2.5 Hadron Calorimeter

The hadron calorimeter (HCAL) contributes to measuring jets and missing energy from neutrinos or new particles. The CMS HCAL is a sampling calorimeter composed of layers of scintillator sandwiched between absorbing materials. As the barrel section must fit into the magnet bore, it lies in between the ECAL ($R = 1.77$ m) and the magnet ($R = 2.95$ m), limiting the amount of material absorbing hadronic showers in the radial direction. An extra detection layer is located outside the solenoid, using the magnet material to increase the amount of absorber. The endcaps are located behind the ECAL endcaps. Forward calorimeters (based on Cherenkov light collection) located 11.2 m from the interaction point extend pseudorapidity coverage up to $|\eta| = 5.2$. They

measure both electromagnetic and hadronic components of showers, but are historically categorized as a part of HCAL. An overview of the HCAL component layout (with the exception of the forward calorimeters) in the CMS detector is shown in Figure 3.13.

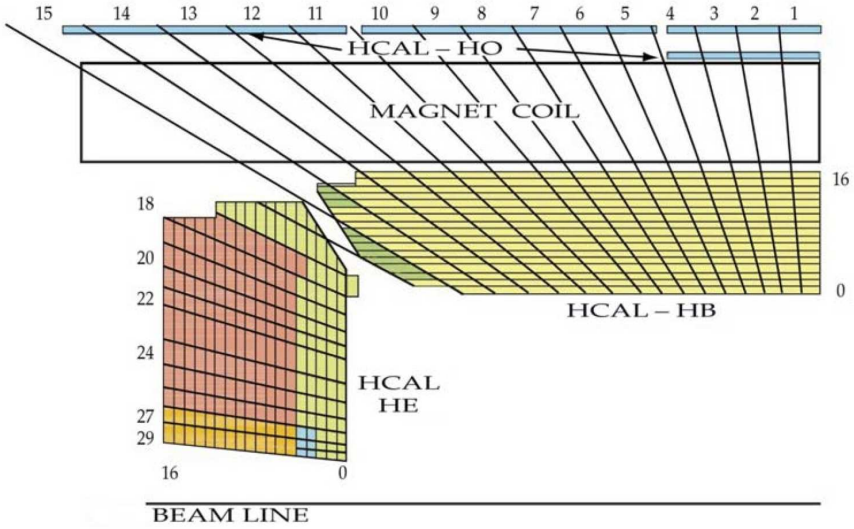

Figure 3.13: HCAL barrel (HB), endcap (HE) and outer (HO) layout for one fourth of the detector [43].

The HCAL barrel (HB), similar to the ECAL barrel, is divided into 36 sections of 20° in ϕ, 18 on the plus z side and 18 on the minus z size, and has coverage $|\eta| < 1.3$. Each section has 4 ϕ segmentations. The absorber is made out of a 40 mm thick steel plate, 8 brass plates 50.5 mm thick, 6 brass plates 56.5 mm thick, and a 75 mm thick steel plate. The steel plates are used for increased mechanical strength. This amounts to 5.82 interaction lengths at $|\eta| = 0$, increasing to 10.6 interaction lengths at $|\eta| = 1.3$. The ECAL barrel in front corresponds to about 1.1 interaction lengths. Between the absorber plates are plastic scintillators, segmented into 16 η sections. The resulting HCAL granuality is $\Delta\eta \times \Delta\phi = 0.087 \times 0.087$. The HCAL scintillator tiles are read out using wavelength shifting fibers fed into silicon-based hybrid photodiodes (HPDs). For most of HCAL, all longitudinal sections sharing the same η and $|phi$ coordinates are read out together. The HCAL endcaps (HE) extend the pseudorapidity coverage to $|\eta| = 3.0$.

The HE absorber layers are 79 mm thick with 9 mm gaps which house the scintillators. HE contains 20916 scintillator tiles, and the granularity is about $\Delta\eta \times \Delta\phi = 0.17 \times 0.017$ in this region. HCAL has about 70000 tiles in total.

The outer calorimeter (HO) was motivated by the limited amount of material inside the magnet bore, which does not absorb hadronic showers adequately in the central pseudorapidity region. To remedy this, the solenoid coil is used as an absorber and additional scintillators (HO) are placed outside the bore. HO is thus constrained by the muon system, and has granularity matching that of HB. Finally, the two forward calorimeters (HF) further extend the coverage to $|\eta|$ of 5.2. Due to the harsh radiation environment, quartz fibers were chosen as the active material. One thousand kilometers of fibers are used in the two HF systems. Particles above threshold generate Cherenkov light in the fibers, which is read out by shielded photomultipliers. The calorimeter front face is 11.2 m from the interaction point, and is made up of $\Delta\eta \times \Delta\phi = 0.175 \times 0.175$ towers in 36 wedges. Steel absorber plates house the fibers in grooves, half of the fibers lining the full depth and half starting 22 cm after the front face. The dual-fiber system allows the distinguishing of hadron showers from electromagnetic showers, which have significantly less depth. The 240 t HF lies on a table, and can be aligned to within 1 mm of the rest of CMS.

The pion energy resolution for the ECAL and HCAL combined has been studied in test beam. It can be given as:

$$\left(\frac{\sigma}{E}\right)^2 = \left(\frac{S}{\sqrt{E}}\right)^2 + C^2 \tag{3.5}$$

where the terms were found to be $S = 1.2$ and $C = 0.095$ [47].

3.2.6 Muon System

Muons are expected to be produced in many interesting ways, for example, in the decay of the Standard Model Higgs boson. In addition, beyond the standard model physics, such as those predicting Heavy Stable Charged Particles, also focus on muons or muon-like objects. Therefore the CMS detector has been designed to measure muons effectively. The layout of the muon system is constrained by the magnet to have a barrel and two endcap regions. In addition, to maximize the coverage and for radiation

hardness, gaseous detectors were chosen. The overall muon system layout for one quarter of CMS is illustrated in Figure 3.14.

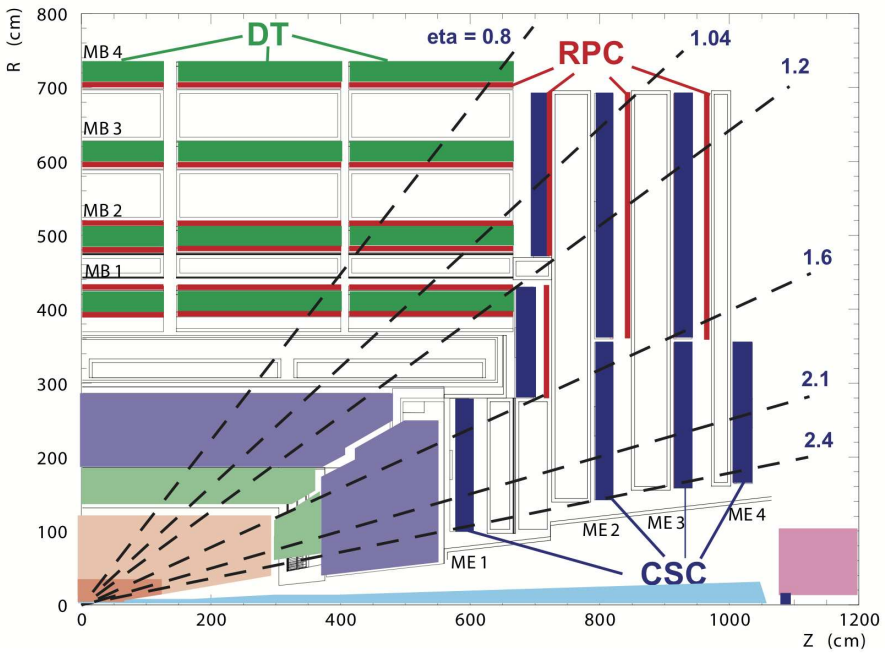

Figure 3.14: The CMS muon system for one fourth of the detector [37].

In the barrel, covering $|\eta| < 1.2$, drift tube (DT) chambers are grouped into wheels, with muon stations sandwiched in between layers of the magnet flux return yoke. There are 5 wheels along the z-axis in the barrel, each divided into 12 sectors about ϕ. Each sector contains its own 4 muon stations, each having 8 or 12 layers of DTs affixed to RPCs. Stations 1-3 host 2 groups of 4 chambers, measuring in the r-ϕ plane, and 4 chambers measuring the z direction. The last station contains only the 8 r-ϕ coordinate-measuring chambers. The chambers can be used to measure timing with good resolution. Each station is made up of 2-3 superlayers containing 4 layers of drift chambers. Signals from passing muons are combined from different stations into a single track. Figure 3.15 shows a schematic view of one DT muon station. The DTs in each station are overlapping in the radial direction to minimize dead regions as can be seen in Figure 3.15. In total, 250 DTs are used, with 2.4 m wire length and 21 mm chosen as the transverse dimension. The target $r - \phi$ resolution was 100 μm attained with 8 track

points measured by the $r - \phi$ chambers.

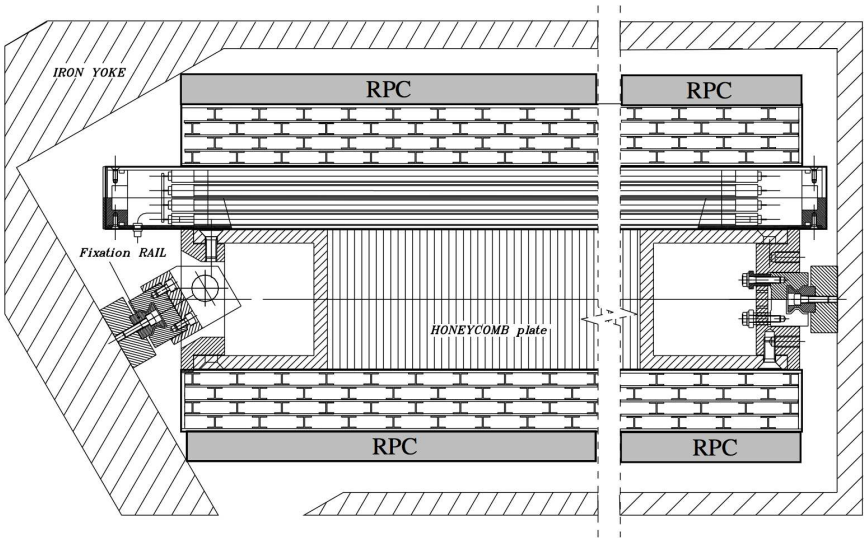

Figure 3.15: A view in the $r - \phi$ plane of a muon station with drift tube chambers organized into two superlayers [43].

In the endcap region, covering $0.9 < |\eta| < 2.4$, 468 cathode strip chambers (CSCs) are used. The choice of CSCs was driven by the non-uniform magnetic field and higher radiation rate in the endcaps. Each endcap contains 4 stations of CSCs, in between layers of return yoke, like the DTs. The CSC is a multiwire proportional chamber with 7 cathode strip panels and 6 anode wire layers inside gas gaps. The cathode strips are aligned along r and measure ϕ. The anode wires, aligned perpendicularly to the strips, measure η and the time. Six layers in each chamber allow use of pattern recognition to reject background and like the DTs, matching of hits to other parts of the detector. The largest CSCs measure 3.4 m in the strip direction and 1.5 m in the wire direction. In each endcap, there are 4 disks of CSCs, with each disk divided into 2 concentric rings. Figure 3.16 shows a cutaway view of an individual CSC along with its response to a passing charged particle. The r-ϕ resolution for the chamber closest to the interaction region (ME1/1b), situated just behind the HCAL, was required to be about 75 μm. A study performed on cosmic ray muons measured a resolution of about 50 μm in this chamber. The resolutions of the other chambers were worse than their design values. This was

attributed to high voltage settings below their design values in order to maximize the chambers' lifetime [48].

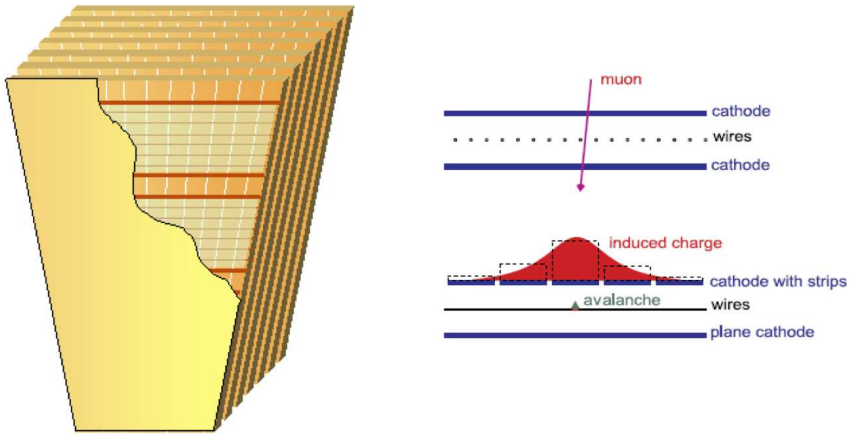

Figure 3.16: Left: A view of a cathode strip chamber, showing some cathode strips and anode wires. Right: Response of the anode and cathode to a passing muon [49].

Offline reconstruction efficiency of the complete muon system is over 95%. The momentum resolution is about 9% for central η and transverse momentum under 200 GeV, increasing to 15-40% at 1 TeV transverse momentum, varying with η. Combining with the inner tracker, the 1 TeV transverse momentum resolution is about 5% [50].

Both CSC and DT systems can also be used as muon triggers for CMS. However, a resistive plate chamber (RPC) system is present in barrel and endcap regions ($|\eta| < 1.6$) to provide independent triggering, even if the background rate increases. They have excellent time resolution but worse position resolution than the DTs or CSCs, and are operated in avalanche mode. The RPCs are incorporated into the muon stations in the barrel and endcap, with barrel stations 1-2 hosting 2 RPC layers and stations 3-4 hosting 1 RPC layer, making six layers in total. Stations 1-3 in the endcap contain one RPC layer each.

3.2.7 Trigger and Data Acquisition

The high collision rate of the LHC, 40 MHz, in addition to its high instantaneous luminosity, and therefore, multiple interactions per bunch crossing, yields too many

collision events to store and process. At the same time, such a high rate is necessary in order to produce particles from rare physics processes. As a result, a system must be implemented to reduce the rate of events that are kept from the collisions, selecting more "interesting" or rare events to keep, ignoring the rest from more common and well-known processes. The CMS trigger system is separated into two parts, Level-1 (L1) trigger and High-Level Trigger (HLT). The L1 trigger is based on hardware, whereas the HLT is software running on a farm of computers. The combined L1-HLT rate reduction is designed to be no less than 10^6. The L1 trigger uses calorimeter and muon system information in a limited way, while the event's full data is kept in buffers. At HLT, more complicated algorithms similar to those used for a physics analysis can be utilized, such as tracking.

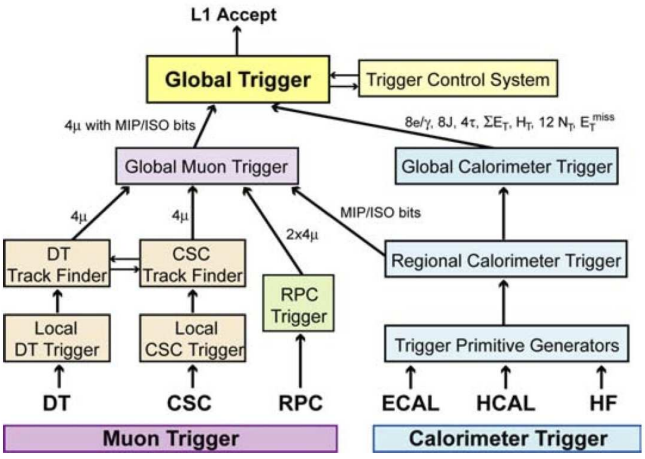

Figure 8.1: Architecture of the Level-1 Trigger.

Figure 3.17: Layout diagram of the CMS Level-1 trigger system [43].

The Level-1 trigger takes as a starting point energy deposits in calorimeter towers ($\Delta\eta \times \Delta\phi = 0.087 \times 0.087$ at $|\eta| < 1.74$) and track segments in muon chambers. These raw data are combined to construct trigger objects such as electrons/photons, jets, or muons. Calorimeter information is also used to construct the missing and total transverse energy. The trigger objects are ranked and sorted based on energy, momentum, and quality. Finally, these inputs are fed to the L1 Global Trigger, which decides

whether to accept the event. On an L1 accept, the full event is read out by the electronics and transferred to the HLT farm. The L1 maximum output rate is 100 kHz. Due to the fact that the L1 trigger must consider every bunch crossing, its decision time is only 3.2 μs. An overview diagram of the CMS Level-1 trigger is shown in Figure 3.17.

The HLT must further reduce the L1 rate from 100 kHz to about 100 Hz, or a factor of 1000. On an L1 trigger accept, the approximately 75 million channels of CMS are read out and collected by about 600 Front End Driver boards. This output is then built into a single event by the Event Builder, utilizing a Builder Network consisting of Builder Units in parallel. Events are built at the 100 kHz maximum L1 accept rate. The built event is then fed to the Filter Systems, made up of Filter Units. Algorithms such as finding and reconstructing jets or particle tracks are run at this stage to make the accept/reject decision. Events accepted by the HLT are forwarded to the Storage Manager for writing. An overview of the CMS HLT and data acquisition architecture is depicted in Figure 3.18.

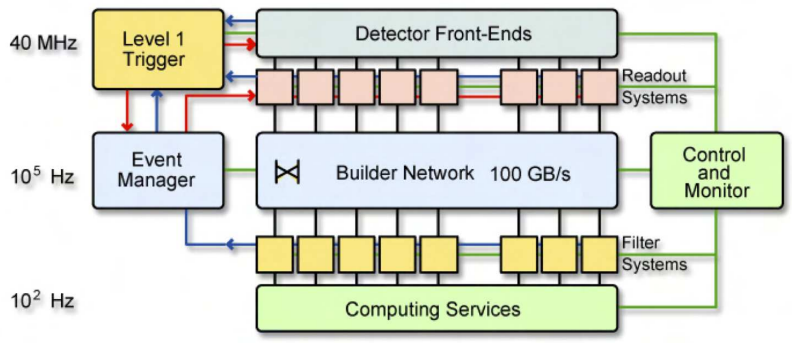

Figure 3.18: Overview of the CMS High-Level Trigger and data acquisition architecture [37].

Chapter 4

Timing Reconstruction and Performance of the CMS ECAL

The CMS Electromagnetic Calorimeter (ECAL) is primary designed for high-precision energy measurement. The resolution goal for unconverted photons in the barrel is 0.5% for energies above 50 GeV, and test beam studies suggest that this is attainable [51]. In searching for the Standard Model Higgs boson, this performance is exploited to obtain high discovery significance in the diphoton decay channel. A 5σ discovery can be made with 10 fb^{-1} at 14 TeV center of momentum (COM) energy for a 120 GeV Standard Model Higgs boson [52]. Recent results using the 2011 7 TeV COM energy dataset (about 4.76 fb^{-1}) have indicated a small excess of about 1σ significance for a Higgs mass of about 124 GeV, while 95% confidence level exclusion is possible at 1.5 to 2 times the Standard Model cross section for a Higgs mass in the range of 110 to 140 GeV [53].

Additionally, the timing of the energy deposit can be measured with high resolution, due to the fast front end electronics and short scintillation timescale of lead tungstate (80% of the light emitted in 25 ns) [54]. This can be utilized in two ways: rejecting background, such as cosmic rays and noise; and identifying particles such as the Heavy Stable Charged Particles described in Chapter 2 and photons decaying from long-lived particles. These particles will travel more slowly and therefore arrive at the calorimeter later than a photon, electron, or other Standard Model particle. A benchmark model

of neutralinos decaying to photons suggests that a time resolution of better than 1 ns is necessary for the timing measurement to have a significant impact. As an added benefit, amplitude reconstruction improves with good knowledge of the readout timing of all channels [55]. In this section, the timing reconstruction, calibration, and performance of the CMS ECAL for single crystals is examined.

4.1 Time Measurements with ECAL

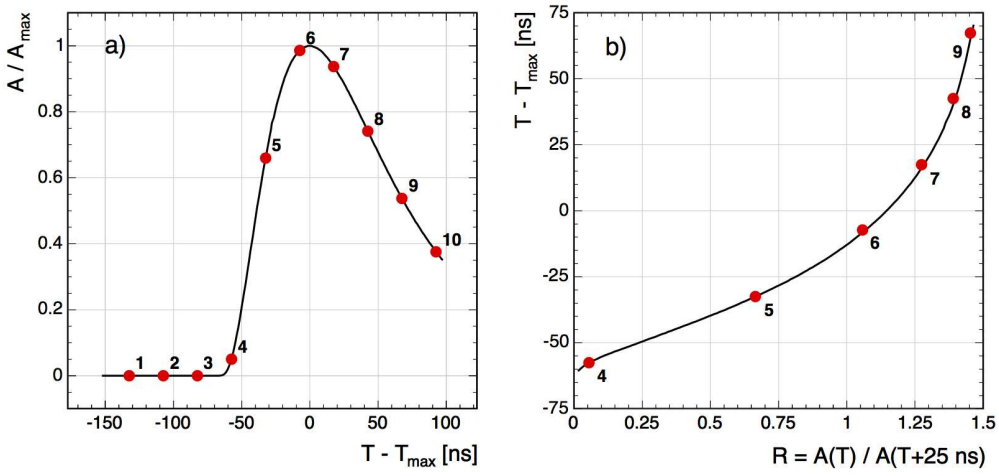

Figure 4.1: Left: An average pulse shape measured in an ECAL crystal as a function of time minus the time of the maximum pulse height (black line). The red dots depict the typical timing readout of the ten amplitude samples of the pulse from the front end digitization. Right: The timing of the pulse as a function of the amplitude ratio of two neighboring samples [56].

The ECAL front-end electronics were described in Chapter 3. Briefly, the scintillation light is amplified and shaped into a pulse, illustrated in Figure 4.1 (left), where the pulse height is shown as a function of the time minus $T_{\max}$, $T_{\max}$ being the time at which the pulse height is maximal. As the timing constants of the front end electronics are identical and the scintillation component decay times are the same for all ECAL crystals, the pulse shape is very similar for all channels. After the (analog) pulse shaping, a 12-bit voltage sampling analog-to-digital converter digitizes the pulse at 40 MHz.

This results in a series of ten pulse amplitude measurements in 25 ns intervals, which are stored in a buffer, awaiting a trigger to transfer these samples to the CMS event data. The ten samples are fixed to the collision time with a known phase. The goal of the ECAL time reconstruction is to measure $T_{\max}$ relative to the collision time using the ten input samples, which are indicated in Figure 4.1 (left). It can be seen that the values of the ten samples depend on the pulse height, the position of $T_{\max}$ between samples, or "phase," and the shape of the pulse produced by the front end electronics. As shown in Figure 4.1 (right), the pulse can also be represented using the amplitude ratio of two consecutive samples, $R(T) = A(T)/A(T + 25\,\text{ns})$. The ratio variable does not depend on the maximum pulse height under the assumption that the pulse shape is independent of amplitude. In order to address small variations of the pulse shape between different crystals, the ratio representation is fitted to a polynomial whose parameters are determined from test beam data for a sample of barrel and endcap crystals separately. These fits are then applied to all crystals in the barrel and endcap.

By using the ratio variable, each pair of neighboring samples yields a measurement of $T_{\max}$, defined as $T_{\max,i} = T_i - T(R_i)$, where T_i is the time of sample i and $T(R_i)$ is the time obtained from the ratio variable using the polynomial parameterization. The uncertainty on each $T_{\max,i}$ can be calculated as the derivative of $T(R)$ multiplied by the uncertainty on R_i. Noise, uncertainty on the pedestal value, and truncation from digitization contribute to the uncertainty on R_i [55]. Ratios with large uncertainties and those from very small amplitudes are not used in the calculation of $T_{\max}$. The others (typically 4 or 5 for in-time particles) are combined into an average weighted by $1/\sigma_i^2$ where σ_i is the uncertainty on each $T_{\max,i}$. By using the simple weighted mean, it is assumed that the ratios R_i are uncorrelated, while in fact, neighboring ratios are anticorrelated since they share a common amplitude sample. This tends to overestimate the uncertainty on the total $T_{\max}$ by about 20% [56]. Noise correlations between samples are a negligible contribution.

Like the energy resolution, the time resolution can be expressed as the quadratic sum of noise, stochastic, and constant terms:

$$\sigma^2(t) = \left(\frac{N\sigma_N}{A}\right)^2 + \left(\frac{S}{\sqrt{A}}\right)^2 + C^2 \tag{4.1}$$

A is the reconstructed amplitude, σ_N the individual sample noise, and N, S, and C are

the noise, stochastic, and constant terms. The noise term was estimated at 33 ns from Monte Carlo simulations, for σ_N of 42 MeV in the barrel and 140 MeV in the endcap. The stochastic term arises from photostatistical fluctuation in light collection inside the crystals, and is estimated to be negligible. The constant term contains effects such as differences in the pulse shape between different channels, as well as uncertainty on the shower initiation point. Time calibration between channels also contributes directly to the constant term, and thus is a vital component which will be discussed below.

4.2 Timing Calibration

Each ECAL channel has reconstructed $T_{\max}$ approximately the same for all Standard Model particles originating from the interaction point (IP), since this is determined by the time of flight to the crystal. However, the time of flight varies across the detector by a few nanoseconds, and each channel has its own intrinsic signal delay, making a channel-to-channel synchronization necessary. This is typically referred to as timing synchronization or calibration, interchangeably. The calibration can be done in two stages, hardware and software. In the hardware, the ECAL front end electronics can adjust the phase of the clock by steps of 25/24 ns in groups of 25 crystals (or fewer in the endcap section), corresponding to a front end card. However, the value of $T_{\max}$ must be measured and adjusted to fine precision to reduce the constant term in the resolution as much as possible. Therefore an additional level of calibration is done offline in the software using physics events. Because the selection is done offline, energy deposits corresponding to only certain particles such as photons or electrons can be used. This may remove systematic effects arising from the inclusion of energy deposits from showering muons, for example. In practice, for the calibrations determined so far, any energy deposit above a given threshold is included to derive the calibration for each channel.

4.2.1 Timing Calibration Using Splash Events

To produce the first calibrations used for 2010 data taking, muons produced from "beam splash" events are used. The first beams circulating in the LHC in 2008 and 2009 were occasionally dumped onto closed collimators located 150 m away from the CMS detector.

The protons, upon impact with the collimators, produced pions and kaons, which then decayed into muons. These muons moved almost parallel to the beam direction in the z axis, at nearly the speed of light. The proton bunch length in the z direction was about 6 cm, or 200 ps of intrinsic time width. The arrival time of the splash to each crystal can therefore be approximated as dependent only on the crystal's position. Several muons cross each crystal in a typical splash event, which together deposit around 5 GeV, and every crystal receives significant energy. The reconstructed energy in each crystal for a single splash event in shown in Figure 4.2.

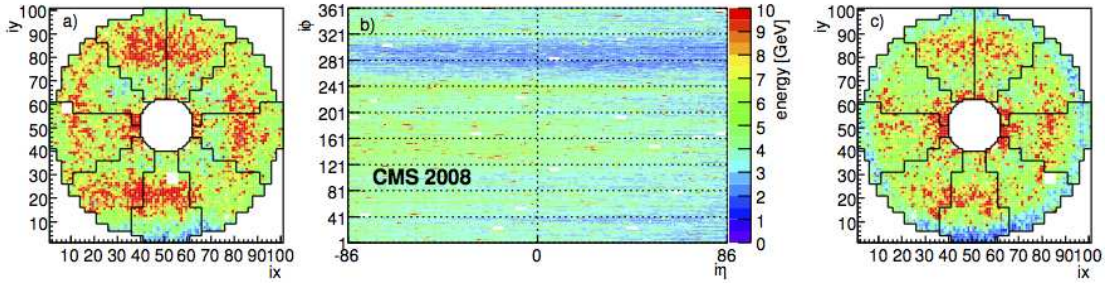

Figure 4.2: Energy per crystal reconstructed from a beam splash event. (a) and (c) Minus and plus endcaps, respectively, where ix and iy are the horizontal and vertical crystal coordinates. (b) Barrel, where iη and iϕ are the η and ϕ crystal coordinates. In all cases, white regions represent channels masked in the readout at the time of the event, less than 1%. Many channels have since been recovered [56].

For the splash calibration, a sample of events from Autumn 2009 was used for the channel-to-channel ECAL timing calibration. The performance difference when including the offline timing calibration is shown in Figure 4.3, comparing the average reconstructed time of all crystals from collision events, including hits above 0.6 GeV.

Particles from beam splash travel as a plane wave, as described above, and do not come from the interaction region. In order for the times obtained from the splash events to be applicable to particles traveling from the interaction region, a transfer function must be applied. This is done using the geometrically predicted difference in time of flight between particles coming from the interaction region and those from the splash. This difference depends on the muon direction (plus or minus z) and the crystal position. Crystals with the same η coordinate have a common predicted time of flight.

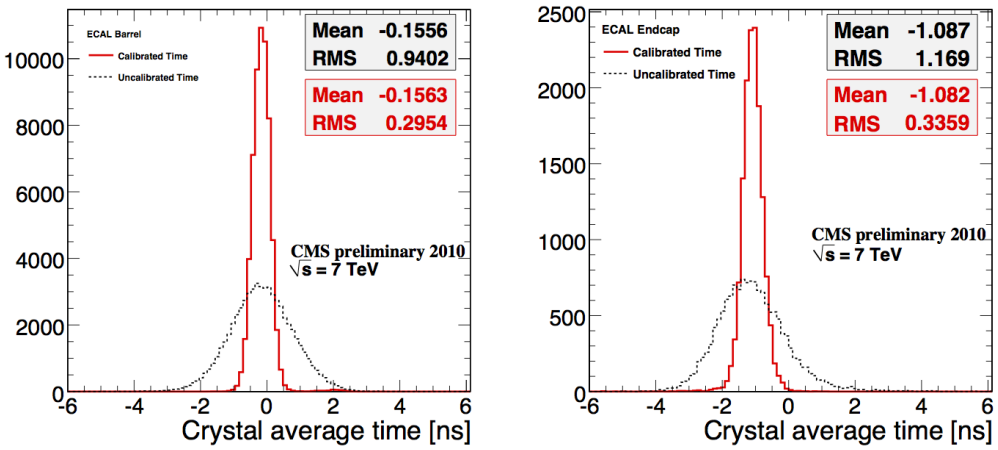

Figure 4.3: Average reconstructed time for ECAL crystals with hardware calibration only (dashed gray line) and including software calibration determined from 2009 beam splash events (solid red line) [57].

4.2.2 Timing Calibration for 2010 Data Taking

For the 2010 run, in order to minimize geometric effects from using splash data and applying the transfer function, rings of crystals with the same η coordinate were realigned using LHC collision data from early 2010. Defined in this way, there are 170 rings of 360 crystals each in the barrel. The choice to realign in rings as opposed to doing a full crystal by crystal calibration was taken chiefly because of the lack of high energy hits in the given data. In the endcaps and barrel, the average time was realigned as well. Hits above 2.5 GeV reconstructed energy were used in all cases with high-quality data certified by detector experts. The resulting calibrations were validated by looking at their effect of the reconstructed time on statistically independent collision data.

The result of this alignment by rings in the barrel is shown in Figure 4.4. Using collision events, it is necessary to limit the effect of anomalous energy deposits (see below). This was done by imposing a loose time window on the times used to calibrate each channel.

For the remainder of 2010, it was possible to create a calibration for each crystal using the collision data itself. This was done by using any energy deposit hitting a crystal above a threshold of several GeV and taking the timing measurement. After the

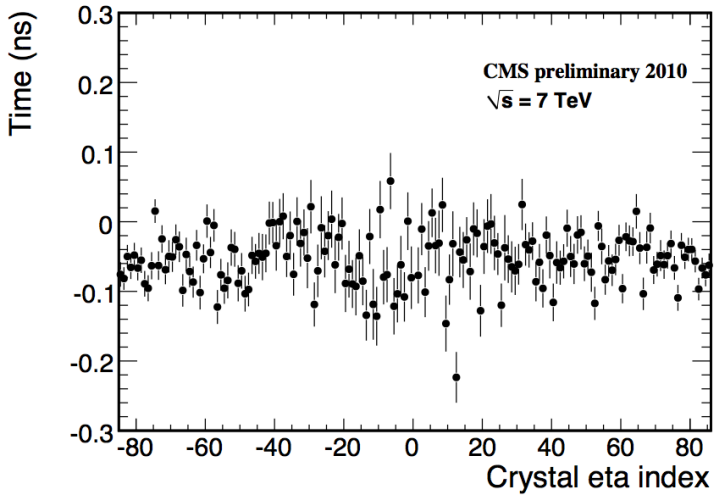

Figure 4.4: Average reconstructed time for ECAL crystals in the barrel sharing the same η index, as determined from early 2010 collision events [57].

removal of anomalous energy deposits and imposing the loose time window, the simple average of all the timing measurements is taken as the channel's calibration. During the 2010 run, it was necessary to perform the calibration process several times to account for interventions in the electronics. These interventions had been observed to cause shifts in the readout timing. In addition, during this period, a dependence of the average time on the reconstructed amplitude was observed, believed to be a result of the ratio reconstruction and the imperfect independence of the pulse shape with amplitude. A correction based on the measured deviations was implemented and validated. A final set of timing calibrations for the 2010 run was deployed in December 2010.

4.2.3 Timing Calibration in 2011

In the 2011 run, data came in rapidly and a timing calibration based solely on the 2011 collision data was deployed in July. Interventions with the ECAL electronics again caused occasional timing shifts to appear at the ∼25 crystal level, and adjusted sets of calibration constants were deployed to correct them. There were 17 sets of calibrations deployed to adjust for these changes and global shifts in the clock.

For 2011, the calibration tools were updated for better ease of use and integration

with the calibration database. In addition, the timing bias as a function of amplitude was extended to higher amplitudes and included in the reconstruction. With the increased luminosity available, the calibration dataset could be limited to events firing the ECAL or HCAL triggers for which the timing measurement would be most appropriate, and datasets such as events with Z candidates could be used to validate and study the timing performance (see below). Finally, each set of calibrations was also tested on the original dataset from which it was derived (closure). There were no major changes to the calibration procedures.

4.3 ECAL Timing and Anomalous Energy Deposits

During data taking in 2010, isolated high energy deposits were observed in the ECAL barrel. These deposits are believed to be caused by particles passing though the APD and directly ionizing the sensitive volume. The rate of these events is approximately 10^{-3}, looking at minimum bias events, which scales with the center of momentum energy, consistent with the creation of more charged particles at higher $\sqrt{s}$ [58]. To identify these deposits, also known as "spikes," shower topology and timing can be used. A deposit in which 95% or more of the cluster energy is located inside a single crystal is determined to be anomalous and is flagged. Thus by comparing the energy deposited in a crystal to that of its neighbors, a spike can be flagged.

The reconstructed timing can also distinguish between spikes and normal showers. The pulse shape of a normal shower is a convolution of the scintillation pulse shape and the electronics shaping, whereas for spikes, only the electronics shaping is involved. Reconstructing the different spike pulse shape with the shape expected for normal showers causes a bias in the measured time. Figure 4.5 illustrates this bias by showing the reconstructed time of the highest energy hit in each event for minimum bias data at $\sqrt{s}$ =7 TeV. The time for normal showers is distributed around zero, whereas the time for the spikes peaks around -10 ns, due to the steeper rising edge in their pulse shape. The long positive tail is believed to be due to slower particles such as low momentum neutrons ionizing the APD. For each hit, using the expected timing resolution at that energy, a flag is set if the difference between the measured and expected time is greater

than 5 standard deviations. It can be seen from Figure 4.5 that about 8% of the anomalous deposits with transverse energy greater than 3 GeV are flagged as out of time but pass the topological selection, as shown by the dashed line. The spikes that are in time but not tagged topologically make up less than 1%, which illustrates the power of the using both timing and topological cuts together. ECAL timing has thus already served an important role by helping to reject these anomalous deposits, which can contaminate high energy jets and large missing energy events.

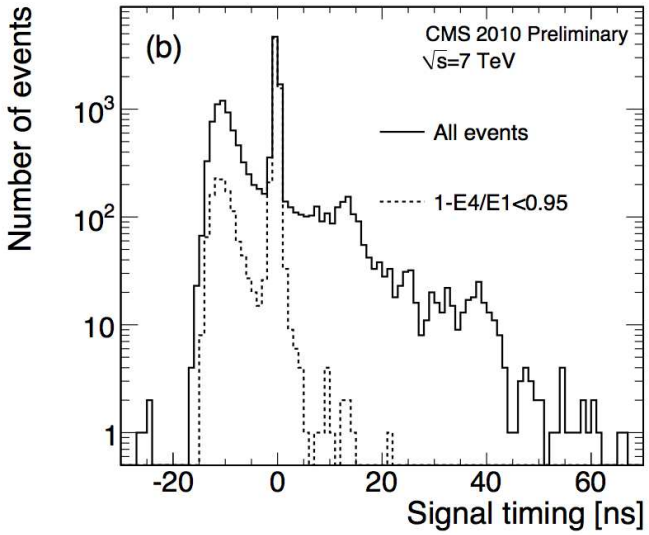

Figure 4.5: Reconstructed timing of the highest energy hit in each event from minimum bias data, shown for all hits (solid line) and those which are not topologically flagged as anomalous (dashed line). Of those in the latter category, about 8% with transverse energy greater than 3 GeV are flagged as out of time [57].

4.4 Time Resolution Performance

In calibrating the ECAL timing, one must keep in mind the expected performance of the timing, in particular, the time resolution. While the time offset (or bias) is also important, it is more difficult to minimize the time resolution spread due to systematic effects arising in the calibration process. The spread of the calibrations drives the constant term of the time resolution, which dominates the entire time resolution at high

energies (see Equation 4.2). One can determine the ECAL performance in an idealized scenario, such as test beam, as well as that observed in a more typical physics situation, like the times of two electrons from a Z boson decay. These studies are presented in the following sections.

4.4.1 Time Resolution From Test Beam Data

A study on the time resolution was completed with electron test beam data in 2008 using fully assembled barrel and endcap modules. The modules were exposed to electrons with energies between 15 and 250 GeV at the H2 and H4 beam facilities at CERN. Using an adjustable table to hold a module, the beam was aimed onto each crystal of the module in turn, allowing electrons to impact crystals at different points, and the fraction of energy deposited in a crystal to vary. These modules were subsequently inserted into the CMS detector [51].

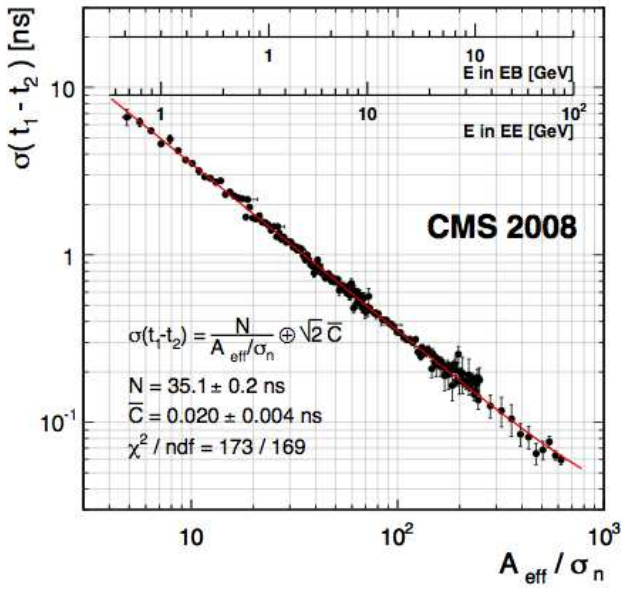

Figure 4.6: Width of the time difference between two neighboring crystals in electron test beam, taken from Gaussian fit. The beam energy varied between 15 and 300 GeV; the single crystal energy scale is shown at the top [56].

The time resolution itself was measured from the difference of the time between two crystals sharing the same shower and registering similar energies. This technique minimizes the C term, since systematic effects, such as crystal-to-crystal synchronization, tend to cancel. For this study, the polynomial ratio parameterization was calculated for each crystal used, suppressing effects from slightly differing pulse shapes. The time difference at all energies considered is observed to have a Gaussian shape with only small tails. Therefore, the spread is obtained from a Gaussian fit to the distribution and parameterized as:

$$\sigma^2(t_1 - t_2) = \left(\frac{N\sigma_N}{A_{\text{eff}}}\right)^2 + 2\bar{C}^2 \tag{4.2}$$

Here $A_{\text{eff}} = A_1 A_2/\sqrt{A_1^2 + A_2^2}$, t_1, t_2, A_1, A_2 are the times and amplitudes measured in the two crystals, and $\bar{C}$ is the remaining constant term. The parameterized width $\sigma^2(t_1 - t_2)$ is shown in Figure 4.6. It can be seen that $\sigma(t)$ decreases to less than 100 ps for A_{eff}/σ_N over 400. Thus, with good control over the calibration and synchronization, this resolution is attainable with large energy deposits, for example, over 20 GeV in a signal crystal in the barrel.

4.4.2 Time Resolution From 2010 LHC Collision Data

The time resolution was studied using collision events from the 2010 run using a procedure similar to that described above. While neighboring crystals sharing the same shower were still used to compute the time difference, in this case the ratio parameterization was performed on a subset of crystals first, and this single result used for all crystals. The ratio parameterization was performed separately for EB and EE. The resolution obtained from this procedure is shown in Figure 4.7. The noise terms for EB and EE are consistent with the test beam expectations. The constant term of about 300 ps (200 ps in EE) is the lower limit on the time resolution achievable at high energy. In practice, the time resolution for a single channel is higher, due to the fact that in this study systematic effects tend to cancel. For instance, the crystals connected to the same front end card experience a common delay, and these crystals are always neighboring in the barrel, and often neighboring in the endcaps. A study relaxing these constraints (and which is therefore more realistic) is described below.

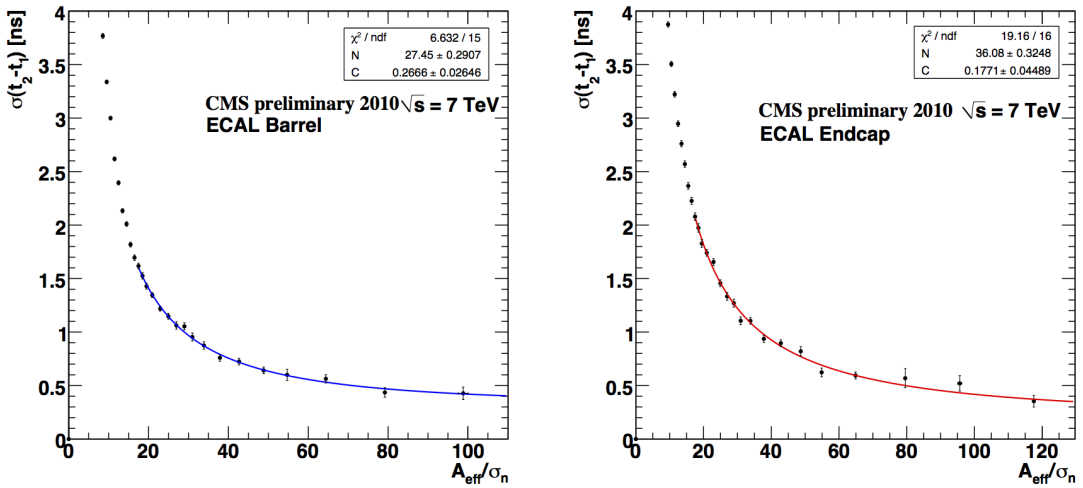

Figure 4.7: Width of the time difference between two neighboring crystals from 2010 collision data, taken from Gaussian fit, in the ECAL barrel (left) and endcap (right) regions. The fit is to the parameterized time resolution given in Equation 4.2, with $\bar{C}$ replaced by C. Energies up to 4.5 GeV are examined in the barrel, and up to 18 GeV in the endcap.

4.4.3 Time Resolution From Dielectrons In 2011 LHC Collision Data

Another study undertaken in 2011 examined the ECAL time resolution based on dielectron events originating from Z boson decays. Here, 1.1 fb^{-1} were used, selecting particles with transverse momentum over 10 GeV and requiring the reconstructed mass of the two particle system to be within 20 GeV of the nominal Z boson mass. In addition, cuts on simple variables such as the shape of the shower were used to select electrons at the 80% efficiency level [59]. Additionally, both electrons were required to be in the barrel, and there was an upper energy cut to limiting the hits to the first electronics gain. The time of the highest energy crystal associated to each electron is used to represent the reconstructed time of the electron. The two electron times are subtracted and the width is determined from a Gaussian fit. The result is shown in Figure 4.8 using the 2010 timing calibrations (left) and the 2011 calibrations (right). While not a parameterized result using the energy as shown before, it nonetheless yields an estimate of the expected time resolution for a typical electron in the barrel. The spread is about 300 ps for the 2010 calibrations, and about 200 ps for the 2011 calibration. Since the two crystals are

no longer neighboring, this is a result more appropriate for a typical physics use case of measuring the time of a given electron.

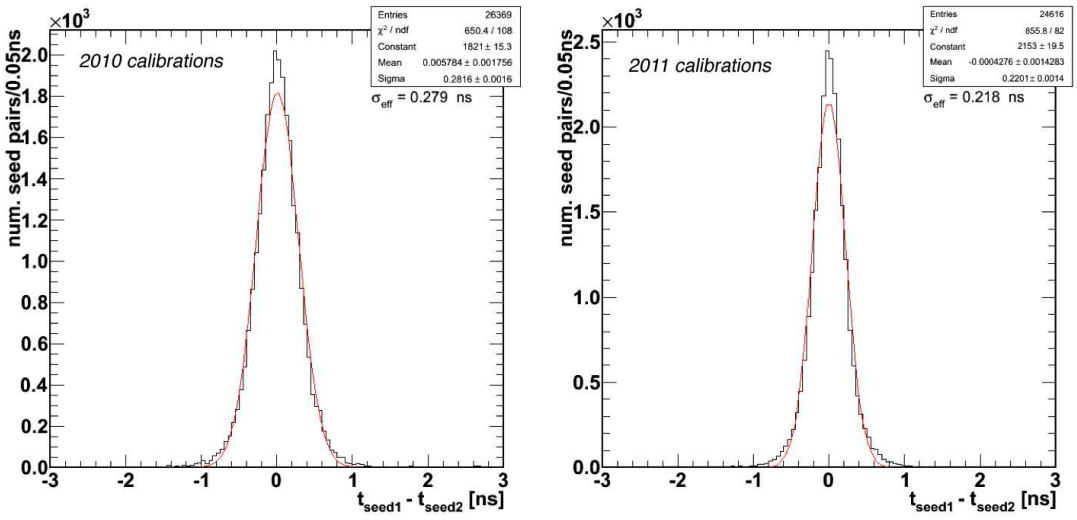

Figure 4.8: Width of the time difference between the seed crystals of two Z candidates from 2011 collision data. The σ_{eff} is defined as half of the interval containing the 68.3% of the entries. The left plot uses timing calibrations derived from 2010 data, while the right plot uses the most recent time calibrations as derived from 2011 data.

Chapter 5

LHC Satellite Bunch Search with ECAL Timing

In 2010, an effort was started to look for evidence of satellite bunches in the LHC, which incorporated the use of precise ECAL timing. A satellite bunch is defined as beam particles contained in the same 25 ns (40 MHz) slot in the beam structure, but not in the nominal radio frequency (RF) bucket. This can occur as a result of particles leaking into neighboring RF buckets in the accelerators upstream of the LHC, or leakage in the LHC itself. For example, the Super Proton Synchrotron, used as part of the LHC injection chain, has a 200 MHz accelerating system, or 5 ns slots. The LHC itself uses a 400 MHz accelerating system, or 2.5 ns slots [33]. Thus the structure of any such leakage can be indicative of its origin.

5.1 Luminosity Calibration and Bunch Current Normalization

The importance of these satellite bunches comes into play when trying to measure the absolute luminosity. A precise value of the luminosity is needed to make cross section measurements and perform searches like that described in this thesis. In some cases the uncertainty on the luminosity dominates the total systematic uncertainty, and therefore it is essential to reduce the luminosity uncertainty as much as possible. The luminosity

L for two bunches is

$$L = f N_1 N_2 \sqrt{(\mathbf{v_1} - \mathbf{v_2})^2 - \frac{(\mathbf{v_1} \times \mathbf{v_2})^2}{c^2}} \int \rho_1(\mathbf{x}, t)\rho_2(\mathbf{x}, t) d^3x dt \tag{5.1}$$

where the density functions of beam 1 and beam 2 are $\rho_1(\mathbf{x}, t)$ and $\rho_2(\mathbf{x}, t)$, and the velocity of the particles in the bunches from beam 1 and beam 2 are $\mathbf{v_1}$ and $\mathbf{v_2}$, assumed to be identical for all particles in the bunch. The bunch population in each beam is given by N_1 and N_2, i.e., the number of protons in each bunch contributing to the luminosity, and f is the revolution frequency.

In order to calibrate the luminosity at each interaction point (IP), a van der Meer scan can be performed [60]. Another method was also used to calibrate the luminosity at the LHC, but will not be discussed here. In the van der Meer scan, the beams are moved along the transverse axis and the collision rate is measured as a function of the displacement. Integrating the rates over the displacements yields the overlap integral, the integral in Equation 5.1. The bunch populations N_1 and N_2 must be determined in a separate measurement. In a preliminary analysis, the dominating uncertainty on the final luminosity came from this bunch current normalization. As part of the effort to characterize and reduce the uncertainty on the bunch current normalization, and through it, the uncertainty on the luminosity, satellite bunches and "ghost" charges needed to be measured. This effort was organized as the Bunch Current Normalization Working Group (BCNWG), and involved representatives of CMS, ATLAS, LHCb, ALICE, and the LHC machine.

The luminosity calibration was performed at two times in the 2010 run, once in April and May, and again in October. For the April-May scan, $\beta^* = 2$ m, implying a beam size of 45 μm, assuming the nominal transverse emittance of 3.75 μm. There was no crossing angle. For the October scan, $\beta^* = 3.5$ m, and there was a 100 μrad crossing angle at IP5, where CMS is located. More details can be found in two notes released by the working group in 2011 [61][62].

To measure the bunch current, the LHC has eight current transformers, two direct current current transformers (DCCTs) and two fast beam current transformers (FBCTs) for each beam. The DCCT yields a measurement of the total beam current, while the FBCT measures the population of each bunch in each 25 ns beam slot. The FBCT sum over all the bunches is normalized to the total current from the DCCT, so any

information about charge which does not contribute to the luminosity is lost. The satellite bunches are one example of such non-luminous charge, and therefore their contributions must be estimated by another means. They are then taken into account in the luminosity calibration.

5.2 Satellite Bunch Measurement Using ECAL

ECAL timing in CMS was one method used to detect and measure the satellite bunches. In particular, satellite bunches can result in collisions that are out of time and displaced along the z or beam axis. For example, a bunch trailing the nominal RF bucket by 5 ns can collide with the main bunch in the other beam at about $\pm$75 cm along z away from the nominal interaction point (+75 cm if the satellite is in beam 2, -75 cm if the satellite is in beam 1). For the case of a satellite in beam 1, where collisions with the main bunch occur at about -75 cm along z, collision products will be delayed by about 5 ns for a detector on the positive side ($z > 0$) of the interaction point, but will appear with nominal time in a detector on the negative side. The ECAL time is defined as nominal for particles emerging from the two main bunches colliding at the interaction point. For satellites leading the main bunch by 5 ns, the signal will appear early in the detector closer to the displaced collision. The collision with the mean bunch will occur at about +75 cm for a leading satellite in beam 1 and about -75 cm for a leading satellite in beam 2.

To search for evidence of these signals displaced in time, the two ECAL endcap (EE) calorimeters were used. There is one endcap on each side of the interaction point, EEP on the $z > 0$ side and EEM for the $z < 0$ side. All events firing the minimum bias trigger were used in the analysis, as were all energy deposits (clusters) having a seed crystal registering at least 4 GeV. This energy requirement allowed the timing precision to be kept to less than 1 ns; see Chapter 4. To see the impact of ghosts on the bunch current normalization, data from the LHC fills during which the van der Meer scan was performed was examined.

5.3 Results for the April-May and October van der Meer Scans

The following plots show the reconstructed time of EE clusters, where a time of zero corresponds to that expected for particles emerging from collisions of the two main bunches at the nominal interaction point. Clusters from the EEP detector are shown on the left, and those from the EEM detector on the right. A cluster with time of +5 (-5) ns in EEM is interpreted as the result of a collision between the main bunch of beam 1 and a satellite bunch in beam 2 trailing (leading) the main bunch by 5 ns. Likewise, for EEP, a cluster with time of +5 (-5) ns is interpreted as the result of a collision between the main bunch of beam 2 and a satellite bunch in beam 1 trailing (leading) the main bunch by 5 ns. Figure 5.1 shows the reconstructed times of EE clusters for LHC fill 1089, taken as part of the April-May 2010 van der Meer scans. One can see an indication of satellite bunches trailing the main by 5 ns in both beam 1 and beam 2, i.e., clusters with reconstructed time of +5 ns, and evidence of additional satellites is visible. In some cases evidence of an out of time peak was note clear, and in those cases upper limits on the satellite bunch population were determined. The figures for all fills under investigation are given in [61].

To quantify the satellite particle population, the satellite peak in the plot was fitted with a Gaussian, representing the signal, summed with an exponential of a third-order polynomial, representing the background. The result of the fit for the Gaussian part determined the yield for the satellite peak, $R_{\pm 5ns}$ which was then compared with the yield of the nominal peak at 0 ns, R_{0ns}. The displaced collision yields must be corrected for the change in the β function near the interaction point. This "hourglass" effect should cause the rate to scale as the inverse of $\beta(z) = \beta^*(1 + (z/\beta^*)^2)$ and reflects a change in the transverse beam size. After this correction, assuming that the same orbits and shapes apply for all bunches and zero crossing angle, the ratios $S_{\pm 5ns,0}$ and $S_{0,\pm 5ns}$ give the trailing or leading (+5 or -5 ns) satellite bunch population relative to the main bunch population, where the first index is for beam 1, and the second one for beam 2.

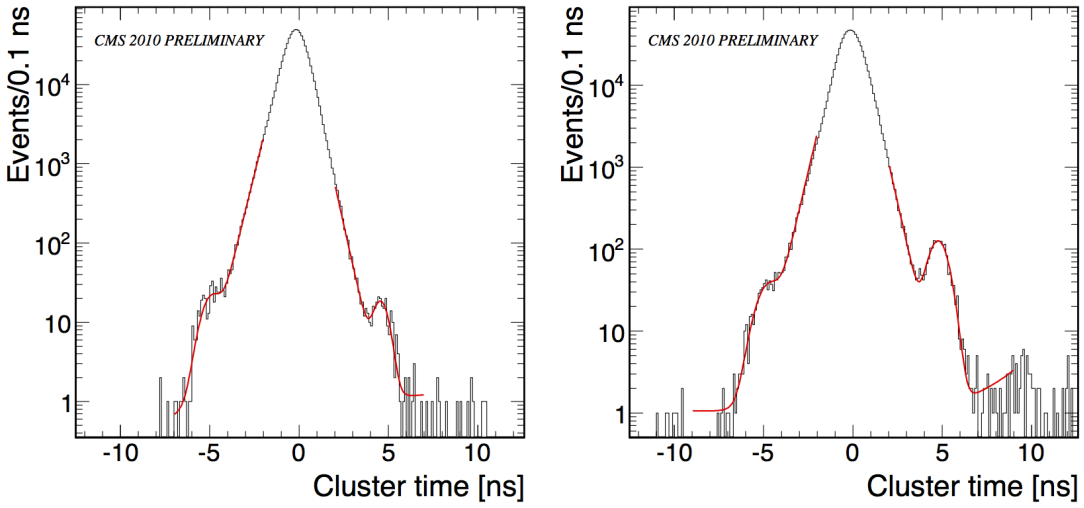

Figure 5.1: Reconstructed time of clusters in the ECAL endcap for LHC fill 1089, part of the April-May 2010 van der Meer scans. Left: EEP detector ($z > 0$). Right: EEM detector ($z < 0$). Evidence of satellites can be seen in the peaks at $\pm$ 5 ns and at +10 ns away from the nominal time of 0 ns [61].

The ratios are defined as follows:

$$\begin{aligned} S_{0,+5ns} &= 2\left[\frac{R_{+5ns}}{R_{0ns}}\frac{\epsilon_{0ns}}{\epsilon_{+5ns}}\frac{A_{0ns}}{A_{+5ns}}\right]_{EEM} \qquad S_{+5ns,0} = 2\left[\frac{R_{+5ns}}{R_{0ns}}\frac{\epsilon_{0ns}}{\epsilon_{+5ns}}\frac{A_{0ns}}{A_{+5ns}}\right]_{EEP} \\ S_{0,-5ns} &= 2\left[\frac{R_{-5ns}}{R_{0ns}}\frac{\epsilon_{0ns}}{\epsilon_{-5ns}}\frac{A_{0ns}}{A_{-5ns}}\right]_{EEM} \qquad S_{-5ns,0} = 2\left[\frac{R_{-5ns}}{R_{0ns}}\frac{\epsilon_{0ns}}{\epsilon_{-5ns}}\frac{A_{0ns}}{A_{-5ns}}\right]_{EEP} \end{aligned} \tag{5.2}$$

The ratio $\epsilon_{0ns}/\epsilon_{\pm 5ns}$ is a correction for the selection efficiency due to the bias of the reconstructed amplitude due to late arriving hits. These late hits are reconstructed with slightly less amplitude than in time hits, causing some of them to fall under the amplitude selection threshold. This bias is known [55]. To measure the effect, the amplitude selections were changed and the ratios of the resulting yields were calculated. The correction factor was thus obtained as 1.058 $\pm$ 0.02. The ratio A_{0ns}/A_{-5ns} accounts for the geometric change in acceptance for collisions closer to or farther from the detector along z. To evaluate this effect, first, the new pseudorapidity range was calculated geometrically assuming the displaced collision point. For collisions closer to the detector along z, the pseudorapidity coverage is effectively lowered from its minimum value, while for collision farther from the detector along z, the pseudorapidity range is

effectively increased from its maximum value. In the first case, the barrel is used to estimate the change in acceptance, while in the second case, the pseudorapidity distribution is extrapolated from the original. The number of clusters in these two altered pseudorapidity ranges is then compared with that in the original range to estimate the acceptance corrections. Intuitively, the hole in the endcap is effectively increased in solid angle for closer collisions, leading to an acceptance decrease, which must be corrected upwards, while the opposite is true for collisions farther from the detector. Applying the procedure bears out this reasoning, as the corrections obtained were 1.205 ± 0.07 for collisions closer to the detector and 0.61 ± 0.07 for collisions farther from the detector. The trigger efficiency was assumed to be equal for all scenarios considered here.

The ratios in Equation 5.2 can be combined in order to obtain the total satellite bunch population at a distance of ± 75 cm along z, S_{+75cm} and S_{-75cm}. This also enables comparison with the other analysis methods used to measure the satellite bunch populations. S_{+75cm} and S_{-75cm} are defined as

$$\begin{aligned} S_{+75cm} &= S_{-5ns,0} + S_{0,+5ns} \\ S_{-75cm} &= S_{0,-5ns} + S_{+5ns,0} \end{aligned} \tag{5.3}$$

The results are shown in Table 5.1.

Fill	$S_{+5ns,0} \cdot 10^3$	$S_{0,-5ns} \cdot 10^3$	$S_{-75cm} \cdot 10^3$
1058	< 0.007	< 0.013	< 0.021
1059	< 0.079	< 0.127	< 0.206
1089	$1.53 \pm 0.068 \pm 0.26$	$0.390 \pm 0.053 \pm 0.066$	$1.919 \pm 0.086 \pm 0.326$
1090	$0.498 \pm 0.103 \pm 0.085$	$0.225 \pm 0.077 \pm 0.038$	$0.724 \pm 0.123 \pm 0.123$
Fill	$S_{-5ns,0} \cdot 10^3$	$S_{0,+5ns} \cdot 10^3$	$S_{+75cm} \cdot 10^3$
1058	< 0.040	< 0.004	< 0.044
1059	< 0.085	< 0.068	< 0.152
1089	$0.828 \pm 0.152 \pm 0.141$	$0.155 \pm 0.025 \pm 0.026$	$0.983 \pm 0.154 \pm 0.167$
1090	$0.270 \pm 0.103 \pm 0.046$	$0.175 \pm 0.048 \pm 0.030$	$0.446 \pm 0.144 \pm 0.076$

Table 5.1: ECAL timing results for the ± 5 ns (lagging/leading) satellite bunch populations relative to the main bunch for the LHC fills used in the April-May 2010 van der Meer scans. Uncertainties are first statistical, then systematic [61].

For the October 2010 van der Meer scans, the LHC was using 150 ns bunch trains, in addition to the different β^* of 3.5 m and the crossing half-angle of 100 μrad. Due to this crossing angle, when the satellite and main bunches interact, in addition to the

collision's displacement along z as before, there is now a transverse separation of $2z\tan\phi$, where ϕ is the crossing half-angle. The transverse separation reduces the luminosity by $e^{-\frac{d^2}{2\Sigma_w^2(z)}}$, where d is the transverse separation, $\Sigma_w(z)$ is the effective beam size at the z position, given by the "hourglass" effect formula $\sigma(z) = \sigma(0)\sqrt{1+\left(\frac{z}{\beta^*}\right)^2}$. Taking into account the transverse separation and the hourglass effect yields a factor of 0.178 for CMS at $z = 75$ cm [62]. Thus the measured yields were corrected by a factor of $1/0.178 \sim 5.62$. The beam and bunch intensities were also higher than in the April-May scan.

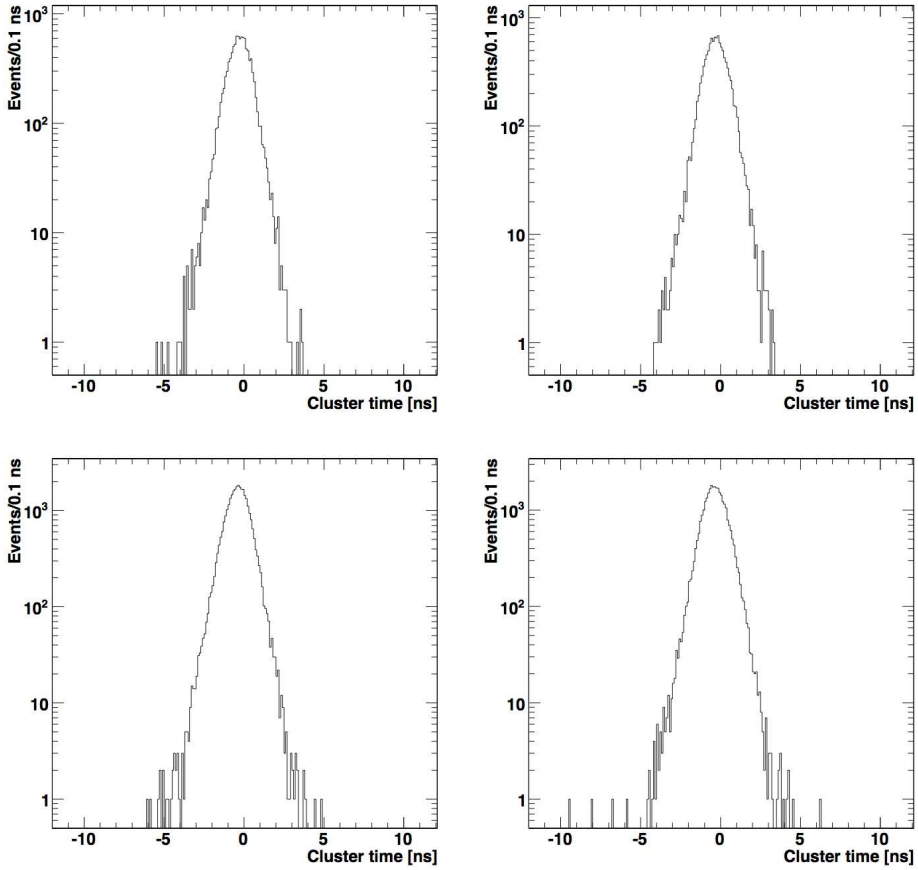

Figure 5.2: Reconstructed time of clusters in the ECAL endcaps, for the two fills comprising the October 2010 van der Meer scans. Left: EEP detector ($z > 0$). Right: EEM detector ($z < 0$). Top: LHC fill 1386. Bottom: LHC fill 1422. No evidence of satellites can be seen at $\pm$ 5 ns away from the nominal peak and upper limits are set [62].

The search for satellites using ECAL timing was conducted in much the same way as it was for the April-May scan. Zero-bias triggers were used, and data during the LHC fills for the van der Meer scans, but excluding the scans themselves, was analyzed. The fill numbers were 1386 and 1422, and the plots of the reconstructed time in the ECAL endcaps is shown in Figure 5.2. The main peak timing is shifted from zero to about -0.3 ns due to a shift in the overall timing synchronization. As can be seen from the plots, no evidence of satellites was found. Studying the tails of the main peak using separate data showed that the few events present in this sample are consistent with a background-only expectation. Due to different trigger conditions, however, this study could not be used to reliably estimate the background under the signal peaks. Therefore a $\pm$ 1 ns window around -5.3 and 4.7 ns was used, whereby all clusters falling in the window were attributed to signal and used to set 95% confidence level upper limits. These corrected upper limits are shown in Table 5.2.

Fill	$S_{+5ns,0} \cdot 10^3$	$S_{0,-5ns} \cdot 10^3$	$S_{-75cm} \cdot 10^3$
1386	< 0.94	< 6.97	< 7.87
1422	< 2.03	< 3.04	< 4.82
Fill	$S_{-5ns,0} \cdot 10^3$	$S_{0,+5ns} \cdot 10^3$	$S_{+75cm} \cdot 10^3$
1386	< 3.69	< 2.87	< 6.03
1422	< 1.00	< 1.90	< 2.69

Table 5.2: ECAL timing results for the $\pm$5 ns (lagging/leading) satellite bunch populations relative to the main bunch for the two fills comprising the October 2010 van der Meer scans [62].

The ECAL timing measurement was thus able to contribute effectively to the LHC satellite bunch measurements. Along with the ECAL timing, tracking system measurements in CMS and ATLAS were also used. The ECAL results were in good agreement with the tracking system measurements, as detailed in the BCNWG notes.

Chapter 6

Measurement of dE/dx and Mass Reconstruction

As noted in Chapter 2, the signature of an HSCP is a high momentum, slowly moving track, which should behave similarly to a muon, aside from R-hadron charge flipping effects. The low β feature of the particle will lead to high specific ionization and prolonged time of flight with respect to a Standard Model particle. To measure the mass of the particle, a measurement of the β is combined with a measurement of the momentum. In the case of specific ionization, the Bethe-Bloch equation is linearized directly to compute the mass, as explained below. As the momentum measurement is the designed function of the tracking system, it will not be discussed further here. The momentum measurement performance is described in Chapter 3. The following sections will describe the specific ionization measurement and mass reconstruction in detail.

6.1 The Bethe-Bloch Equation

The interaction of an HSCP in matter is dominated by ionization. The Bethe-Bloch equation (with several corrections) describes the mean energy loss due to ionization in matter [63]

$$-\frac{dE}{dx} = Kz^2\frac{Z}{A}\frac{1}{\beta^2}\left[\frac{1}{2}\ln\frac{2m_e c^2\beta^2\gamma^2 T_{\max}}{I^2} - \beta^2 - \frac{\delta(\beta\gamma)}{2}\right] \tag{6.1}$$

where z is the charge of the particle (in units of e, the fundamental charge), Z is the atomic number of the absorber, A is the atomic mass of the absorber, m_e is the electron mass, $\gamma = 1/\sqrt{1-\beta^2}$ is the Lorentz gamma factor, $T_{\max}$ is the maximum kinetic energy transfer to a free electron in a single collision, I is the mean excitation energy for the absorber, $\delta(\beta\gamma)$ is the density correction, and $K = 4\pi N_A r_e^2 m_e c^2$, with $r_e = e^2/4\pi\epsilon_0 m_e c^2$ being the classical electron radius and N_A being Avogadro's number. The Bethe-Bloch equation describes the mean energy loss within a few percent for $\beta\gamma$ between 0.1 and about 1000, which corresponds to about 0.001 to 100 GeV momentum for a muon. At higher values of $\beta\gamma$ radiative effects contribute increasingly to the energy loss, while at lower values, additional effects must be taken into account. These regimes are shown in Figure 6.1. Figure 6.2 shows the energy loss of particles as a function of $\beta\gamma$ in different materials.

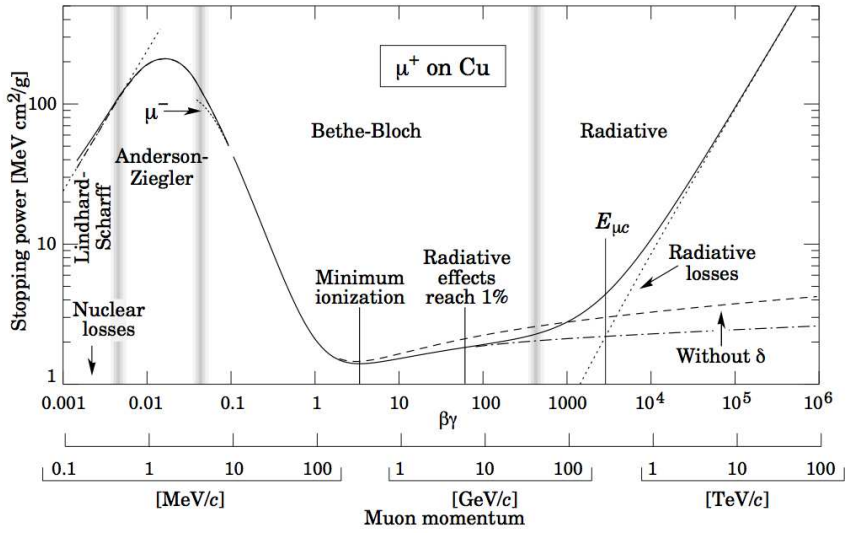

Figure 6.1: The stopping power (dE/dx) of muons in matter as a function of $\beta\gamma$. A restricted region inside the Bethe-Bloch regime is used in the HSCP search [63].

For relativistic particles, the mean energy loss is typically close to the minimum in the Bethe-Bloch regime, so they are often called minimum ionizing particles (MIPs). However, for non-relativistic particles, the energy loss curve increases roughly as the inverse square of β. In this regime, below the MIP minimum energy loss, the β can be measured by measuring the dE/dx since given an absorber, and a particle momentum,

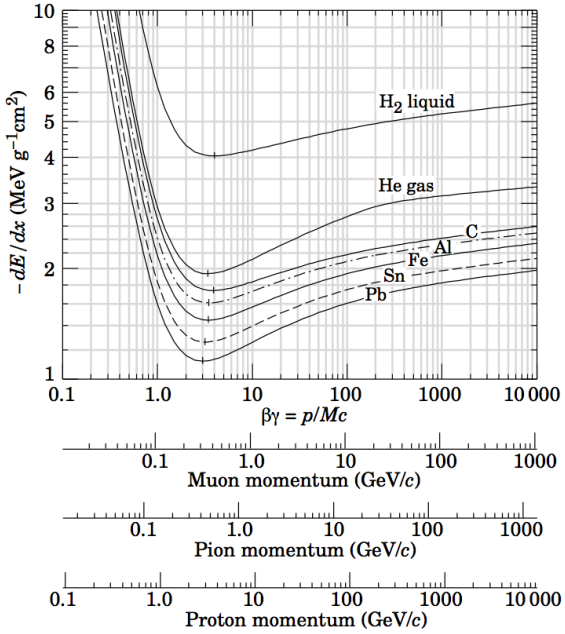

Figure 6.2: The mean energy loss for particles in different absorbers as a function of $\beta\gamma$. The corresponding momentum ranges for muons, pions, and protons are shown [63].

the mean energy loss is determined only by the particle's β. There is a lower limit, however, since particles with too low $\beta\gamma$ will arrive too late to trigger and/or be accurately reconstructed. Above the MIP minimum, the Bethe-Bloch dE/dx is changing slowly, such that the energy loss is similar for particles with quite different $\beta\gamma$, making it hard to discriminate between them. Therefore the range of $\beta\gamma$ considered is restricted to about 0.2-0.9. At CMS, low momentum hadrons such as pion and protons can have $\beta\gamma$ values in this restricted range, providing a useful check of the β measurement and mass reconstruction ability. Heavy Stable Charged Particles as well can have $\beta\gamma$ values in this range, given their slow-moving nature. In addition, their specific ionization or $\frac{dE}{dx}$ will be larger compared to that of a Standard Model particle at the same momentum.

6.2 Linearized Approximation of the Bethe-Bloch Equation

In the region of $0.2 < \beta\gamma < 0.9$, the Bethe-Bloch equation can be simplified to [64]:

$$\frac{dE}{dx} = K\frac{m^2}{p^2} + C \tag{6.2}$$

Here K and C are constants which depend on the absorber details, such as thickness, and in practice they are determined by fitting the measured ionization energy loss distribution from protons. Equation 6.2 is within a few percent of the full Bethe-Bloch equation in the restricted $\beta\gamma$ range. It should be noted that the dE/dx values obtained by measurement in a thin absorber are the most probable values of the dE/dx as following a Landau distribution (or Landau-Vavilov-Bichsel distribution) as opposed to the average value given by the Bethe-Bloch formula [63].

In CMS, the tracking system can be used to measure the dE/dx by way of calibrating the charge of each silicon module. The dE/dx is taken as $\Delta E/(\Delta L \mathrm{sec}(\theta))$, where ΔE is the calibrated charge of the cluster (the set of neighboring strips measuring the particle crossing point), ΔL is the effective active layer thickness of the silicon module traversed, and θ is the angle of the track with respect to the normal of the module. Both the pixel and the strip detectors can contribute to the measurement, which yield around 15 measurements of the dE/dx. With such a low number of points, the goal becomes measuring the dE/dx more robustly by suppressing the tail of the Landau-Vavilov-Bichsel distribution, which can easily bias the arithmetic mean. Using all clusters from all parts of the tracking system requires that the each silicon module be calibrated so as to produce the same most probable value for a MIP track. The calibration was accomplished using collision data early in the 2011 run.

6.3 dE/dx Estimators

To obtain a robust overall dE/dx measurement for a track, the individual dE/dx measurements can be combined in different ways, known as estimators. Previous studies examined the performance of different estimators, including the median value, keeping only the lowest 60% of the measurements (truncated 40), and the harmonic squared

average [65]. The harmonic squared average is defined as [64]

$$I_h = \left(\frac{1}{N} \sum_i c_i^k \right)^{1/k}, k = -2 \tag{6.3}$$

where c_i is a particular $\Delta E/\Delta L$ measurement, also referred to as a dE/dx hit. A plot of the performance of the three on 900 GeV collision data and Monte Carlo is shown in Figure 6.3. The median cannot be relied upon when there are only a small number of measurements, as it is easily biased. The truncated 40 is more stable but useful information is lost. The harmonic squared average I_h suppresses the effect of higher dE/dx hits due to the negative weight. This suppression of higher dE/dx hits can be seen in the larger tail at lower dE/dx values for I_h in Figure 6.3. However, for the HSCP search, this is a desired property as tracks from Standard Model particles will have hits that fluctuate upward in dE/dx, and these must be distinguished from tracks that have many high dE/dx hits. Therefore I_h is chosen as the preferred dE/dx estimator for the HSCP search. An updated plot using 7 TeV collision data showing the I_h estimator only is shown in Figure 6.4.

6.4 Mass Reconstruction

Using equation 6.2, the mass of a particle can be reconstructed given a measurement of both its momentum and dE/dx. Of course, the equation is still only valid in the limited range $0.2 < \beta\gamma < 0.9$. In order to use the equation, the constants K and C must first be obtained. For particles traveling through the same absorber and having the same charge, these parameters should be the same and so can be measured by fitting the measured dE/dx data for particles with a known mass. For the most probable value of dE/dx, a triple Gaussian fit is used on data in a small momentum window, 0.96-1 GeV, as shown in Figure 6.5 (left). Here, the proton peak is used, as it exhibits higher dE/dx and is therefore more separated from the minimum-ionizing particles than the kaon peak, as can be seen in the figure. After this is done is different momentum slices, the result can be plotted as a function of momentum and fitted with equation 6.2, where K and C are the free parameters and the proton mass is fixed to its known value of 0.938 GeV. Figure 6.5 (right) shows the result of this procedure. The fit is only done in a restricted range due to saturation effects on the low momentum end (see Section

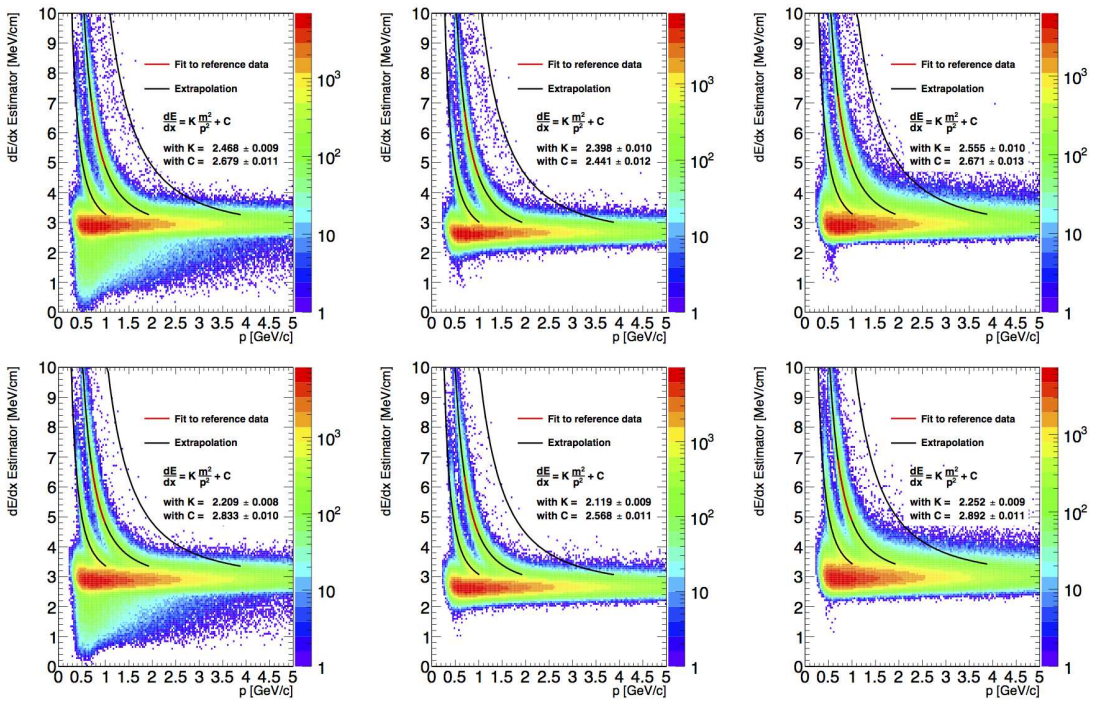

Figure 6.3: Estimate of dE/dx vs. momentum for 900 GeV collision data (December 2009). Shown from left to right are the harmonic squared average, truncated 40, and median estimators. The red line is a fit in a restricted momentum range assuming the proton mass, and the black lines are extrapolations with the fitted values of the parameters. The three lines are considered to be from kaon, proton, and deuteron tracks [65].

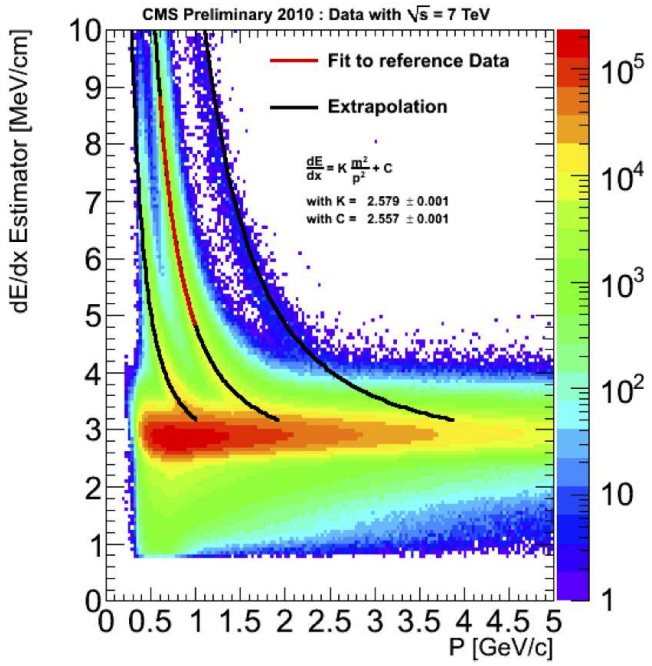

Figure 6.4: Harmonic squared mean estimator of dE/dx vs. momentum for 7 TeV collision data. The red line is a fit in a restricted momentum range assuming the proton mass, and the black lines are extrapolations with the fitted values of the parameters. The three lines are considered to be from kaon, proton, and deuteron tracks [66].

6.7), and difficulty of the triple Gaussian fit to identify the proton peak on the high momentum end, as the dE/dx decreases. Figure 6.4 shows that the constants extracted for the proton work well for kaons and deuterons also.

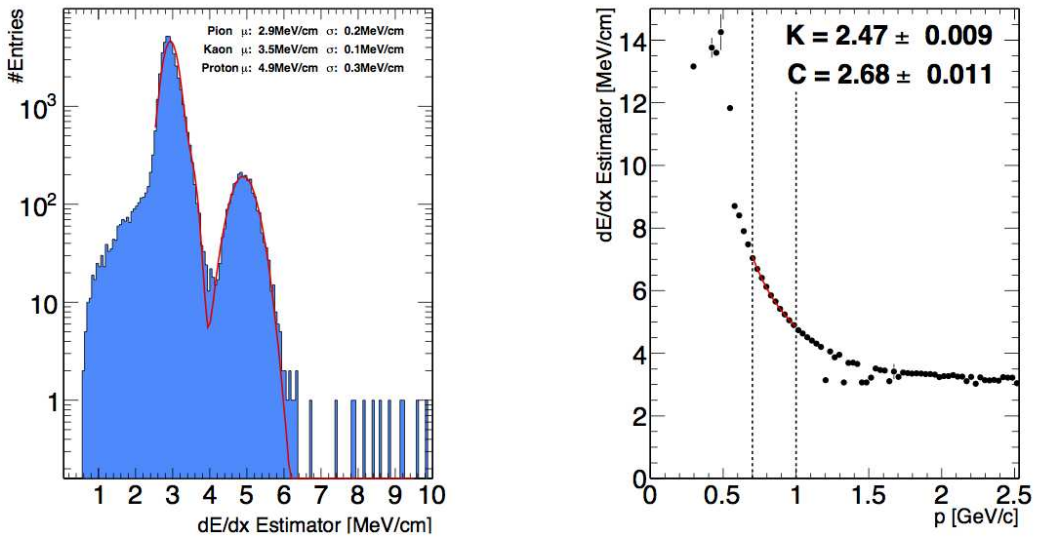

Figure 6.5: Left: Harmonic squared mean dE/dx estimator I_h for tracks in the momentum range 0.96-1 GeV, with triple Gaussian fit. The fitted mean of each Gaussian is used to extract the most probable I_h value for each particle species. Right: Proton most probable I_h as a function of momentum, fitted using equation 6.2 with the mass fixed to the proton mass of 0.938 GeV [65].

Once K and C have been measured, the mass of any particle can be reconstructed. Figure 6.6 shows the reconstructed mass for good quality tracks, compatible with a vertex, having $I_h > 5$ MeV/cm, and $p < 2$ GeV, from 7 TeV collisions for data and Monte Carlo. The kaon, proton, and deuteron mass peaks can be seen in the data. In this version of the Monte Carlo, deuterons were not generated, and thus only the kaon and proton peaks are visible.

6.5 dE/dx Discriminators

Another way to use the $\Delta E/\Delta L$ measurements or dE/dx hits is to combine them into an object called a discriminator. The discriminator tests the compatibility of a measured series of dE/dx hits with the minimum ionizing particle (MIP) hypothesis. This can be

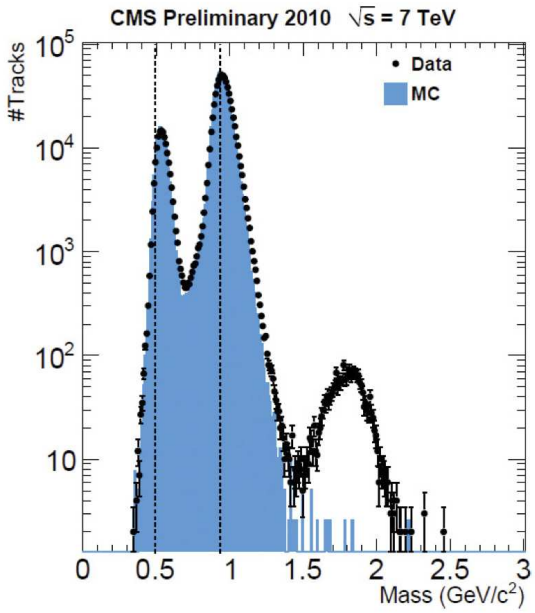

Figure 6.6: Reconstructed mass of tracks with $I_h > 5$ MeV/cm and $p < 2$ GeV from 7 TeV collision data. Vertex compatibility and good reconstruction quality were required on each track [66].

done by constructing the probability density function (PDF) of dE/dx hits for MIPs and then using it to compute the hit-by-hit probability P_h that a MIP would have the same or less dE/dx. There are several effects that are ignored by the dE/dx estimators described above that can be addressed by the discriminator. The path length of the particle through the silicon modules varies due to the differing silicon module thickness in the tracking system as well as the different traversal angles for particles arising from their pseudorapidity and transverse momentum. There is also a small nonlinear dependence of the most probable dE/dx as a function of path length: $\Delta_p/x \sim a \ln x + b$ [63]. This can be taken into account by binning the PDF in terms of the path length. Finally, the electronics saturation also plays a role (see below). The discriminator takes these effects into account [65].

There are several ways to combine the P_h values. First they are sorted in ascending order and then one of the following definitions is used to constructed a discriminator value. The Product discriminator is given by

$$I_p = \left(\prod_{h=1}^{N} P_h \right)^{1/N} \tag{6.4}$$

The Smirnov-Cramer-von Mises discriminator is defined as

$$I_d = \frac{3}{N} \times \left(\frac{1}{12N} + \sum_{h=1}^{N} \left[P_h - \frac{2h-1}{2N} \right]^2 \right) \tag{6.5}$$

The Asymmetric Smirnov-Cramer-von Mises discriminator is written as

$$I_{as} = \frac{3}{N} \times \left(\frac{1}{12N} + \sum_{h=1}^{N} \left[P_h \times \left(P_h - \frac{2h-1}{2N} \right)^2 \right] \right) \tag{6.6}$$

Since each P_h probability ranges from 0 to 1, so do the discriminators themselves. However, their properties differ in important ways. For the product discriminator I_p, a value close to 1 signifies incompatibility with the MIP hypothesis due to high ionization, while a value close to 0 signifies incompatibility due to low ionization. MIPs have values near 0.5.

The Smirnov-Cramer-von Mises discriminator I_d is similar to a Kolmolgorov-Smirnov test in that it measures the difference between a measured and an expected distribution. Typically an empirical distribution is obtained from measurements and compared to a

given cumulative distribution. Here the dE/dx hits are tested for compatibility with the PDF determined from MIPs. In this case, a discriminator value of 0 implies compatibility with the MIP hypothesis, and a value of 1 implies incompatibility. Since in the definition the difference between the distributions is squared, there is no information on whether a high discriminator value is due to an excess or deficit of ionization.

The Asymmetric Smirnov-Cramer-von Mises discriminator I_{as} is a modification of the Smirnov-Cramer-von Mises discriminator such that the probability itself is used as a weighting factor. This modification makes the discriminator have high values only when there is an excess of ionization. Therefore particles depositing more energy than a MIP have higher values, while particles depositing the same or less energy have lower values.

A plot of the values of the different discriminators from 900 GeV data and Monte Carlo is shown in Figure 6.7. The correlation of the different discriminators vs. momentum is shown in Figure 6.8, where the low momentum hadrons can be seen clearly. Due to the sensitivity to ionization excess only, the Asymmetric Smirnov-Cramer-von Mises discriminator is used for the HSCP search.

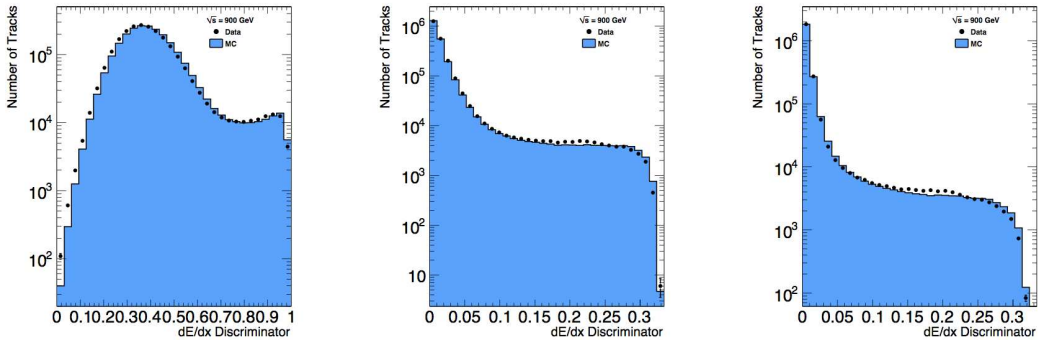

Figure 6.7: Values of the discriminator calculated from particle-calibrated 900 GeV collision data and Monte Carlo. The Monte Carlo is normalized to the data. Left: Product discriminator. Middle: Smirnov-Cramer-von Mises discriminator. Right: Asymmetric Smirnov-Cramer-von Mises discriminator [65].

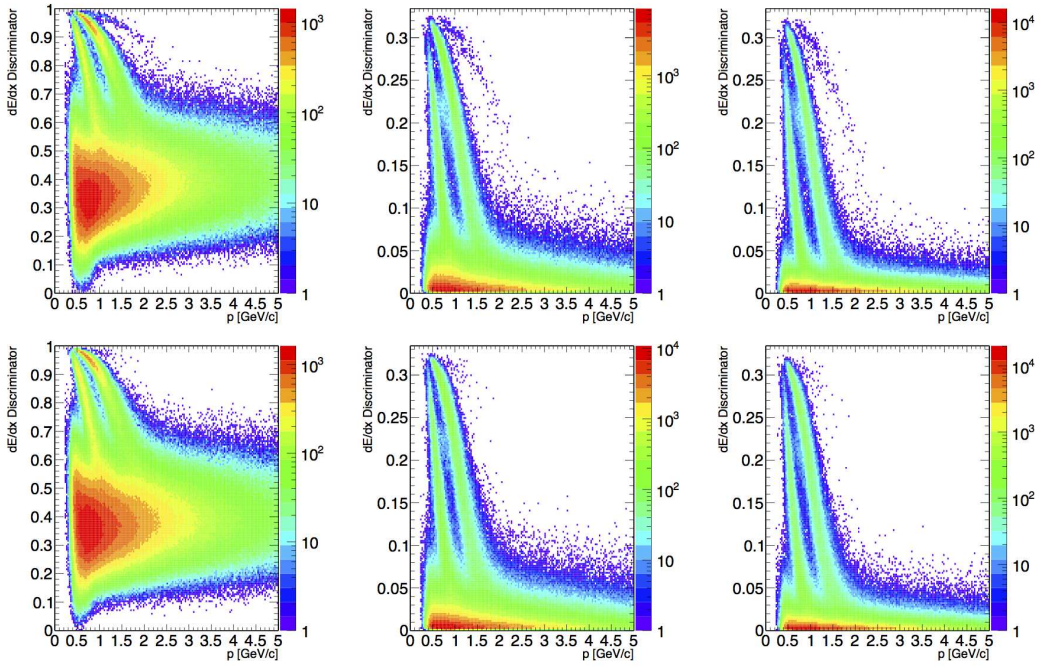

Figure 6.8: Values of the discriminator calculated from particle-calibrated 900 GeV collision data (top) and Monte Carlo (bottom). Left: Product discriminator. Middle: Smirnov-Cramer-von Mises discriminator. Right: Asymmetric Smirnov-Cramer-von Mises discriminator [65].

6.6 Cluster Cleaning

Care must be taken to remove high dE/dx measurements which are due to instrumental effects and not from the incident particle. Such measurements can occur because of overlapping tracks, nuclear interactions, or delta rays impacting the silicon modules. These effects tend to give a anomalous shape to the clustered group of hits. Clusters are checked to make sure that they do not contain more than one maximum and that the maximum does not occur on the edges of the clusters. Strips in the clusters are also checked to make sure that their charges are compatible with noise plus the expected charge, based on the strips carrying the largest fractions of the charge. Any cluster flagged by this check is ignored in the dE/dx computation. The results are shown in Figure 6.9 for I_{as} on data and an HSCP signal sample for tracks passing preselections: $P_T > 5$ GeV, relative P_T uncertainty less than 0.15, transverse and longitudinal impact parameters with respect to the primary vertex less than 1 and 10 cm, respectively, "high purity" selection [67] and at least 3 clusters used for the dE/dx measurement. As can be seen in Figure 6.9, the cleaning reduces the high I_{as} background with only minimal impact on the signal.

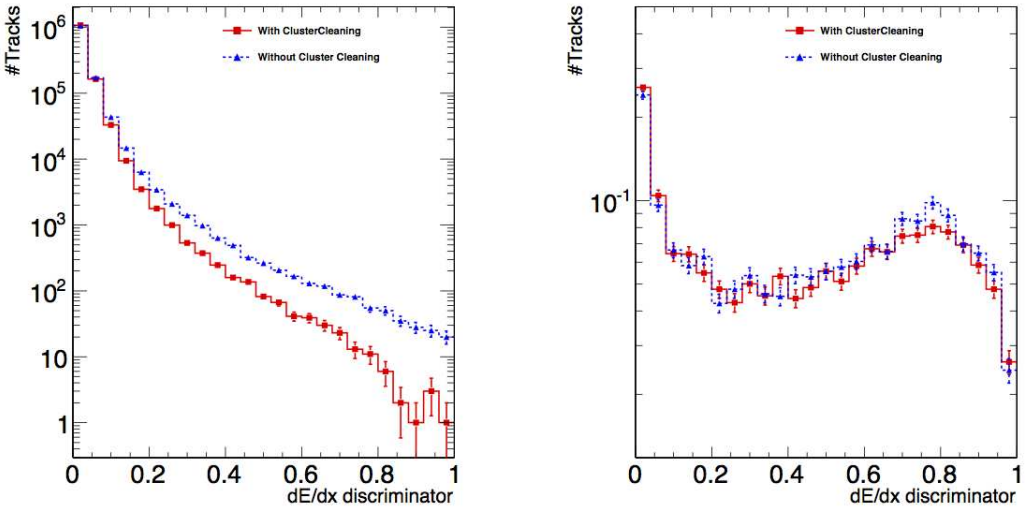

Figure 6.9: I_{as} for candidates passing a preselection with and without cluster cleaning. Left: Tracks from collision data at 7 TeV. Right: HSCP signal model of 200 GeV gluino, normalized to the integrated luminosity of the data [68].

6.7 Silicon Readout Electronics Saturation

An effect mentioned above but not yet discussed is that of saturation in the front end electronics. The dynamic range of the strip tracker electronics is 10 bits, but only 8 bits of information are read out. Thus when the charge is digitized, there is a maximum value of 253 ADC counts, beyond which saturation occurs. The 254 ADC count value corresponds to a charge between 254 and 511 ADC counts, and a value of 255 corresponds to a charge between 512 and 1024 ADC counts. The saturation thresholds depend on the path length and therefore the pseudorapidity of the particle, as well as the thickness of the silicon module. This saturation introduces a bias for highly ionizing particles like HSCPs. By convention, the most probable value of the dE/dx released is 300 ADC/mm after intercalibration. The saturation threshold can be calculated using the amount of energy needed to create an electron-hole pair in silicon at the CMS operating temperature of -10° C, 3.61 eV, and the absolute energy scale of 262 electrons/ADC. Also here only clusters from one strip are assumed. Then the energy deposited by a MIP is [27]:

$$300(\text{ADC/mm}) \times 262(\text{electrons/ADC}) \times 3.61(\text{eV/electron}) = 2.8\,(\text{MeV/cm})$$

The saturation energy is:

$$254(\text{ADC/mm}) \times 262(\text{electrons/ADC}) \times 3.61(\text{eV/electron}) = 0.24\,\text{MeV}$$

Taking the active portion of the silicon module, 30 μm less than nominal thickness, this energy corresponds to 4.9 MeV/cm in 500 μm thick modules, and 7.6 MeV/cm in 320 μm thick modules. This is only about 1.8 and 2.9 times the energy of a MIP, but in general, the clusters are spread over multiple strips. For straight tracks like those from HSCPs, the number of strips in the cluster will be small, however, so the assumption of one strip per cluster is not too far from reality.

Chapter 7

Searching for HSCPs in CMS

This chapter examines a search for Heavy Stable Charged Particles (HSCPs) in the CMS detector. The search was previously done as a counting experiment [64]. The analysis technique described here instead uses shape information to perform a maximum likelihood fit to the data, using background and signal models. In addition, the data is sliced in bins of number of dE/dx measurements (NoM), and pseudorapidity η. These modifications are expected to yield a significant improvement in the sensitivity with respect to the counting experiment method. The complete search technique, along with the results, are presented in this chapter.

7.1 HSCP Properties in CMS

As detailed in Chapter 2, HSCPs are expected to manifest themselves as high momentum, slowly traveling charged particles which make their way through the entire detector before decaying. Thus, measuring the particle's velocity β as significantly less than 1 can distinguish it from a Standard Model (SM) particle. This low β results in high specific ionization or dE/dx and a long time of flight. Combining β with a measurement of the momentum p, the mass can be reconstructed. This was shown in Chapter 6 using dE/dx as an indirect measurement of β. In addition, the dE/dx can also be used to calculate a discriminating variable I_{as} based on the combined likelihood of each dE/dx measurement coming from a minimum ionizing particle (MIP), also discussed in Chapter 6.

7.2 Trigger and Data Selection

High transverse momentum (P_T) muon and missing transverse energy (E_T^{miss}) triggers were used to collect collision data at 7 TeV center of momentum energy at the LHC during the 2011 data taking run (March - October 2011). As the instantaneous LHC luminosity increased, the muon P_T threshold had to be increased from 30 to 45 GeV. The missing transverse energy trigger was at a threshold of 150 GeV throughout the run, based on the particle flow reconstruction [69]. In this technique, each particle is reconstructed separately using information from multiple subdetectors and then clustered into jets. The E_T^{miss} trigger includes HSCPs which are not directly triggered on with the muon trigger, either because they become neutral after interacting with detector materials or simply because they fail to be identified as muons. The events collected by either trigger constitute the data examined here. The trigger efficiency for gluinos and GMSB staus is shown in Figure 7.1. As can be seen in the Figure, the E_T^{miss} trigger contributes negligibly in the case of the leptonic staus, while it provides an important extra contribution to the R-hadron gluino models. The muon trigger efficiency is dependent upon the β of the HSCP in that very slow HSCPs arrive too late to the muon system to be triggered. This can be seen in the decrease in trigger efficiency as the gluino mass increases. In general, due to neutral R-hadron production, the muon trigger path is not as efficient for R-hadrons as for lepton-like HSCPs.

After certifying the data, the total integrated luminosity was 4976/pb. The first 355.227/pb were taken using a tighter Level-1 RPC muon trigger, and therefore have slightly lower signal efficiency. After this first period of data taking, this trigger was opened such that tracks crossing the muon system one bunch crossing late could also be fired. Two different simulated signal samples are used and reweighted by the integrated luminosity of each period two account for this change in the trigger.

7.3 Offline Selection

After events triggered by the muon or E_T^{miss} are selected, a series of quality requirements and other cuts used to eliminate cosmic ray muons and other backgrounds are imposed:

- Tracker track must have quality at least 2 ("high purity"); this involves selections

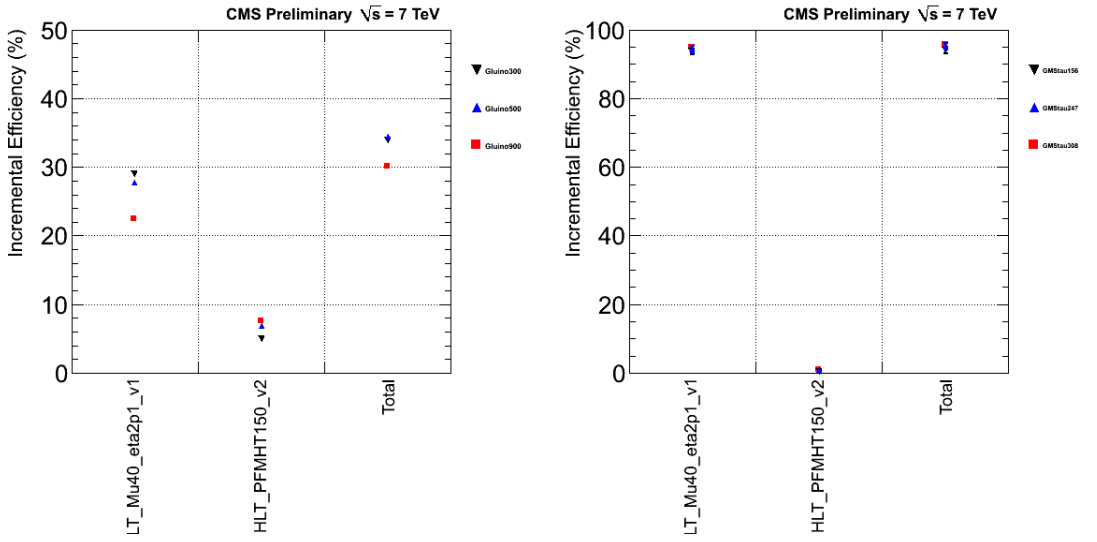

Figure 7.1: Trigger efficiencies for gluinos (left) and GMSB staus (right) of various masses. Mu40 indicates the single muon trigger with $P_T > 40$ GeV, and PFMHT150 indicates the particle flow trigger with $E_T^{miss} > 150$ GeV. Overlaps are excluded. Adapted from [28].

on the transverse and longitudinal impact parameters as well as the normalized χ^2 (of the overall fit) at each iterative step of the tracking based on the number of layers impacted [70]

- Tracker track must have at least 11 hits (see Figure 3.9 showing the number of hits vs. pseudorapidity)
- Tracker track must have at least 2 hits in the pixel detector (out of 3 possible)
- Tracker track must have at least 80% valid hits; invalid or fake hits are created during track reconstruction, accounting for cases where a track did not leave an actual hit on that layer [71]
- Tracker track much have at least 5 I_h measurements after cluster cleaning (see Section 6.6)
- Tracker track much have at least 5 I_{as} measurements from the strip tracker after cluster cleaning (see Section 6.6)

- Tracker track must have normalized $\chi^2 < 5$, where χ^2 is calculated with respect to the track hits and the predicted track parameters [71]
- Tracker track must have $\sigma_{Pt}/P_T < 0.25$; this rejects overlapping tracks in energetic jets with poorly measured P_T
- Tracker track must have $|\eta| < 1.5$; one can see that the HSCPs (especially those with low β) are produced at low $|\eta|$ from Figures 2.6, 2.7, and 2.8
- Track isolation must be less than 50 GeV (defined below)
- Calorimeter isolation must be less than 0.3 (defined below)
- V_{3D} must be less than 0.5 cm where $V_{3D} = \sqrt{d_z^2 + d_{xy}^2}$, d_z and d_{xy} being the longitudinal and transverse impact parameters with respect to the primary vertex minimizing d_{xy}
- Tracker track must have $dE/dx < 2.8$ MeV/cm or $dE/dx > 3.0$ MeV/cm to reduce the size of the sample due to the MIP peak
- Transverse track momentum must be at least 20 GeV

The last two requirements are applied at the "skimming" level, before the other offline requirements. The tracker isolation requirement is intended to reject overlapping tracks from MIPs that may be reconstructed as a high dE/dx track. This can happen, for example, in an energetic jet. To compute the track isolation, the P_T of all tracks in a cone of $\Delta R = \sqrt{(\Delta\phi)^2 + (\Delta\eta)^2} < 0.3$ are summed, excluding the candidate track. This sum is the isolation variable, which must be less than 50 GeV. For calorimeter isolation, the energy from each ECAL and HCAL tower within $\Delta R < 0.3$ from the candidate track is divided by the candidate momentum. That quantity must be less than 0.3. This cut selects only those high momentum particles which do not leave significant energy in the calorimeter, i.e., HSCP behavior. There is no minimum cut on the P_T, I_h, or the like (besides that at the skimming level) in order to increase the statistics in the sideband region of the data. This is necessary because of the background prediction procedure done in slices of η and number of dE/dx measurements; see Section 7.6 below.

	data	**800 GeV $\tilde{g}$**	**200 GeV $\tilde{\tau}$**
Initial candidates	8.76M	124	95
NoM Ih	96.72%	100%	100%
Number of tracker hits	93.05%	98.39%	98.95%
Valid fraction	98.00%	100.0%	100.0%
Pixel hits	98.34%	99.18%	100.0%
NoM Ias	99.97%	96.69%	98.94%
Quality Mask	99.99%	100.0%	100.0%
Chi2/Ndf	99.98%	100.0%	100.0%
η	99.99%	100.0%	100.0%
Pt error	99.97%	97.44%	100.0%
V3D	99.94%	100.0%	100.0%
Track isolation	85.30%	100.0%	98.92%
Calorimeter isolation	68.63%	100.0%	98.91%
All Preselection	50.71%	91.94%	95.79%
Final candidates	data	114	91

Table 7.1: Table of preselection efficiencies for data and two selected signal models, 800 GeV $\tilde{g}$ and 200 GeV $\tilde{\tau}$. The top row denotes the number of candidates passing the trigger selection only. The last row is the number of candidates passing all preselections. For comparison purposes, the signal samples here are scaled to the integrated luminosity used for the data.

7.4 Signal Monte Carlo Samples

In order to study the behavior of HSCPs in the detector, a series of simulated signal samples are needed. The generation details were discussed in Chapter 2. After generation, the particle interactions in the detector must be modeled. The matter interaction model used is taken from [72]. A later interaction model in which the R-hadrons always become neutral because of charge flipping was also implemented [19]. One important unknown free parameter in the hadronization model is the fraction of R-hadrons that are produced as neutral R-gluonballs ($\tilde{g}g$). Two values are used, 0.1 and 0.5, covering optimistic and pessimistic cases as in the previous analysis [73]. Figure 7.2 shows the P_T and I_{as} distributions for both 2011 data and gluino samples after the online and offline selections.

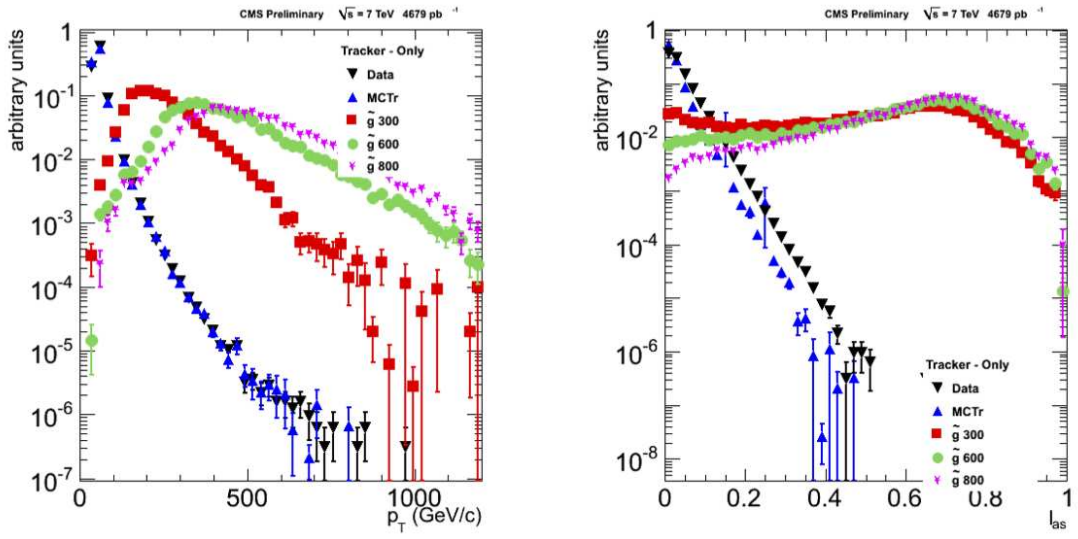

Figure 7.2: Transverse momentum P_T (left) and I_{as} (right) for 2011 data, background Monte Carlo MCTr (not used in this analysis), and several Monte Carlo gluino samples. There was an upward dE/dx shift over the course of 2011 data-taking, which qualitatively explains the Monte Carlo background and data disagreement. In all cases the tracks were required to pass preselection [28].

7.5 Changes from Previous Analysis

The online and offline selections used here are similar to those used in the counting experiment search [28]. At this point, however, there are several important improvements. The first improvement is to move from a counting experiment to a shape-based likelihood fit approach. Using the shape should lead to better sensitivity since it includes more information. Secondly, it can be observed that the dE/dx estimators and discriminator shapes have a strong dependence on both the pseudorapidity η and the number of measurements (NoM). Here the data is sliced in bins of those two variables and the I_{as} shape is determined in each bin. The P_T is still used as a selection variable as in the previous analysis. As the final step, the η/NoM slices are combined in the optimal way in a likelihood fit, maximizing the search sensitivity.

Figure 7.3 shows the I_h and I_{as} distributions in slices of pseudorapidity η. The most relevant effect in the I_{as} distribution is that the high dE/dx tail has a different slope depending on the η region. There is a less noticeable, but still significant effect on the high dE/dx tail of the I_h distribution as well. The dependence of the low I_h tail is observed to be large, but these tracks are below the MIP peak of just under 3 MeV/cm, and so do not enter into the search region. Some reasons for this dE/dx shape dependence include the variation in the number of measurements, which is correlated with η (see Figure 3.9); residual effects of the different particle path lengths; and a small correlation of the dE/dx with η, i.e., the relativistic Bethe-Bloch rise, occurring for background only.

Figure 7.4 shows the I_h and I_{as} distributions in slices of the number of dE/dx measurements. The number of dE/dx measurements is correlated with pseudorapidity as mentioned above, but it has its own effect on the tails of the dE/dx distributions: the higher the number of measurements the more the background's high dE/dx tail can be suppressed.

In addition, the previous analysis optimized the selections for an individual HSCP model in order to obtain the best expected discovery sensitivity, i.e., the minimum cross section at which a 5σ discovery could be claimed with at least 5 events is minimized. This calculation is based on the background level as predicted from the sideband data, and is therefore using the same data twice: once to optimize cuts and again to predict

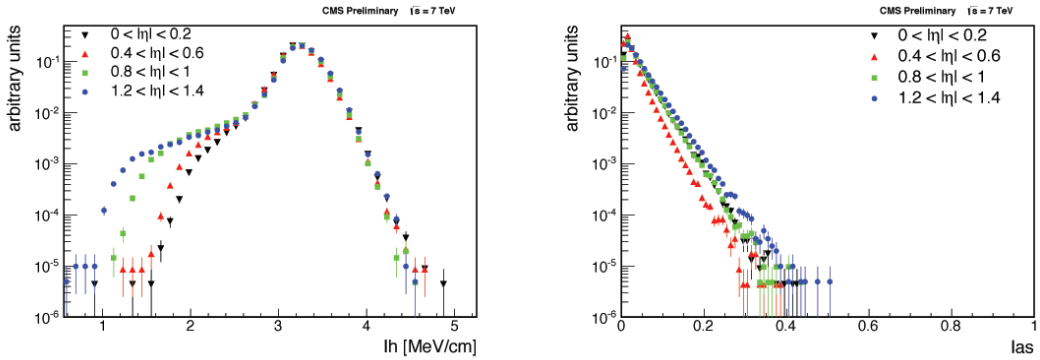

Figure 7.3: I_h (left) and I_{as} (right) in selected pseudorapidity slices for 2011 data passing preselection. Note that the dE/dx shape in general depends on the value of the pseudorapidity. Only the low momentum ($P_T < 50$ GeV) sideband was examined.

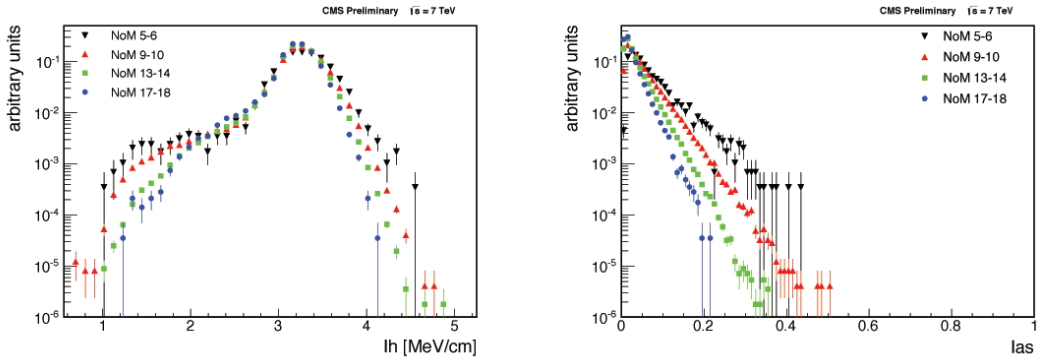

Figure 7.4: I_h (left) and I_{as} (right) in selected number of measurements (NoM) slices for 2011 data passing preselection. Note that the dE/dx tail is suppressed with increasing NoM. Only the low momentum ($P_T < 50$ GeV) sideband was examined.

the background level. This may make these optimized cuts difficult to justify if possible signal is found. Another effect of the optimization is that the sideband thresholds are allowed to change between models and mass points so that what was in the sideband for one model can be in the search region for another, and vice versa. Instead, this approach is done as a blind analysis, where one set of sideband thresholds are applied to all models and mass points. This also avoids the minor complication that the previous analysis' optimization can converge at selections which make little intuitive sense.

Finally, the background prediction procedure has been changed (see below). The prediction is done in each η/NoM slice by obtaining the dE/dx shape after applying a mass cut which is 2 sigma below the nominal HSCP mass. It can be noted that in the standard analysis, the η distribution was reweighted to correct for differences in the dE/dx shape owing to the η dependence shown above. Here, since the prediction is done in η bins, there is no need for such a reweighting.

7.6 Data-driven Background Prediction

The prediction of the I_{as} distribution for light and stable background particles is made using sidebands from the data in an extended "ABCD" method. The two selection variables used are P_T, which is used simply to define the sideband and search regions; and I_{as}, which is used to perform the likelihood fit, owing to its powerful separation of background particles with β near 1 from signal particles with lower β. Four regions are defined using loose P_T and I_{as} cuts:

- A, containing candidates below both thresholds: $P_T < 50$ GeV and $I_{as} < 0.1$
- B, containing candidates with $P_T < 50$ GeV but $I_{as} > 0.1$
- C, containing candidates with $I_{as} < 0.1$ but $P_T > 50$ GeV
- D, containing candidates above both thresholds: $I_{as} > 0.1$ and $P_T > 50$ GeV

Regions A, B, and C are sideband regions which can be used to compute the background prediction in the D region: BC/A. Region D remains hidden until the final stage of the analysis, in keeping with a blind analysis approach. Figure 7.5 illustrates the ABCD division with P_T and I_{as} as the selection variables.

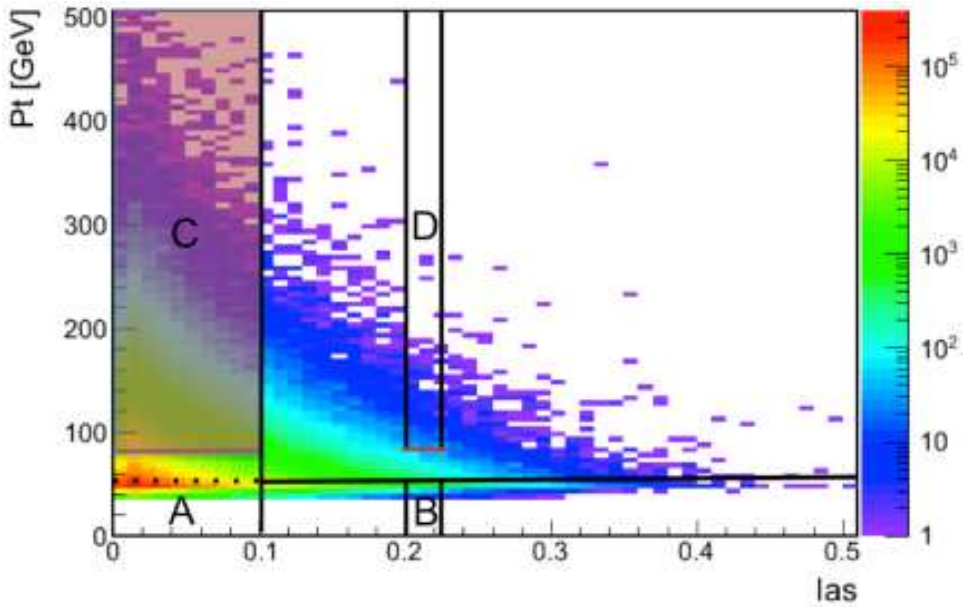

Figure 7.5: Transverse momentum P_T vs. I_{as} distribution for tracks from 2011 data after preselection. A, B, C, and D regions are shown, as is the C_k region (see below).

The ABCD method is altered to make the search region D even smaller, taking advantage of the fact that an HSCP signal will be concentrated in a band around its reconstructed mass in the P-I_h plane. This banding is shown in Figure 7.6 for the gluino of mass 600 GeV. Below the mass band, background is dominant and therefore a mass cut can be used to further reduce background. Figure 7.7 shows the reconstructed mass distribution, again for the gluino of mass 600 GeV.

The goal of the prediction is then to determine the I_{as} distribution in the D region after applying the mass cut, which we call the D' region. Since the minimum momentum to pass the mass cut (and hence, be in the D' region) is dependent on the I_{as} value, the prediction is done in each I_{as} bin, in a bin-by-bin ABCD method. The B region has bin width of 0.02 for each bin k, or 45 bins from I_{as} of 0.1 to 1. We assume $D'_k/B_k = C_k/A$, C_k being the number of events in the C region passing the same minimum momentum used to define D'_k. As I_{as} does not uniquely define an I_h value from which the mass can be calculated, the I_h for each track in B_k is used to calculate the lower momentum limit, defining the C_j region. The average C_j over all the B region tracks is taken as C_k. Then $D'_k = B_k C_k/A$. The mass cut is made 2σ below the nominal HSCP mass,

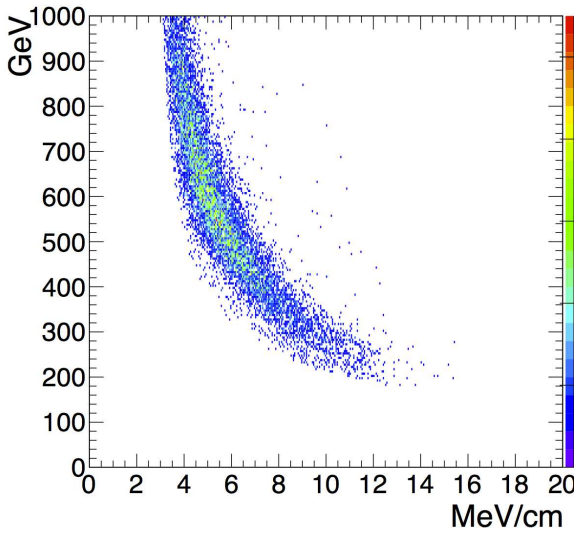

Figure 7.6: Momentum P vs. I_h distribution for gluino of mass 600 GeV from simulation. As shown, the reconstructed mass forms a band which can be used to define a mass cut. This further reduces the background.

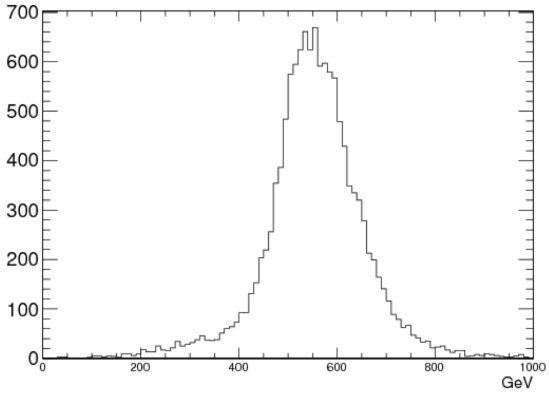

Figure 7.7: Reconstructed mass distribution from simulation for gluinos of mass 600 GeV. For this model, the mass cut is applied at 360 GeV.

where σ is the expected mass resolution (dominated by the dE/dx resolution).

The background prediction is made in each η/NoM bin, but since there is no reason for the momentum to depend on the NoM, the NoM slices in the C region are combined to improve the statistical power. This is important for large HSCP masses, when C_k can become small due to a high momentum requirement to pass the mass cut. In this case, the statistical error on C_k is not negligible. Figure 7.8 shows the momentum distribution in several different NoM regions, illustrating that it is independent of NoM. To further study how well the momentum shapes in different NoM slices agree, the following study was performed.

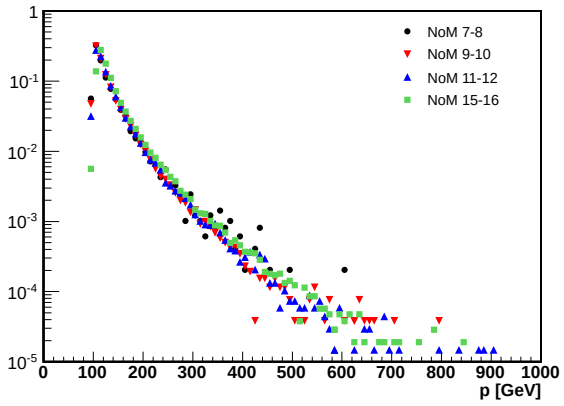

Figure 7.8: Momentum P distribution for tracks with $1.4 < |\eta| < 1.6$, from 2011 data after preselection. Several different NoM slices are shown, illustrating the independence of momentum from NoM. The peak at $P \sim 100$ GeV is due to the muon trigger threshold of about 45 GeV Pt, which becomes about 100 GeV at $|\eta| \sim 1.5$. There is correlation of the NoM with $|\eta|$ causing some variation in this peak value.

First, an exponential fit (binned maximum likelihood) was performed to the tail of the momentum distribution for all NoM slices combined. Figure 7.9 shows the binned maximum likelihood exponential fit to the all-NoM distribution in one η slice, that of $1.4 < |\eta| < 1.6$. The exponential fit is seen to be a good model of the tail of the all-NoM distribution. Next, the result of this all-NoM fit is used as a probability density function (PDF) for each individual NoM slice, where its normalization is allowed to vary. Two NoMs are combined per slice. Figure 7.10 shows the exponential PDF used with one NoM slice, NoM 13-14. Then, the maximum likelihood of the

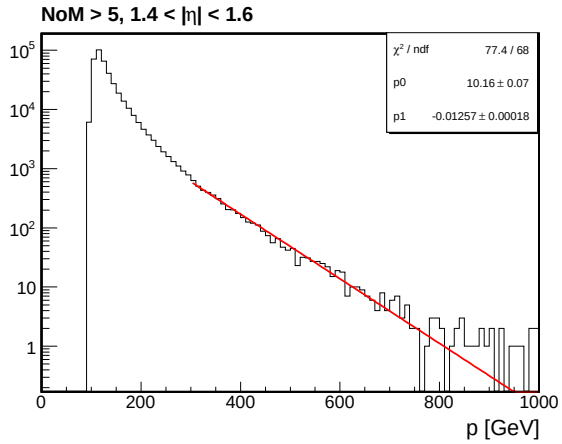

Figure 7.9: Momentum P distribution for tracks with more than five dE/dx measurements within $1.4 < |\eta| < 1.6$, from 2011 data after preselection. The red line is the result of an exponential fit to the tail.

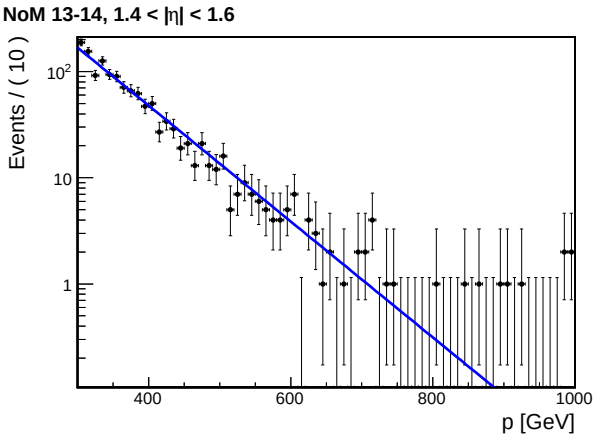

Figure 7.10: Momentum distribution for tracks with 13 or 14 dE/dx measurements within $1.4 < |\eta| < 1.6$, from 2011 data after preselection. The blue line is the normalized exponential PDF from the fit of the all-NoM distribution in Figure 7.9.

all-NoM fit along with that of the "saturated model" for each slice is computed, where the saturated model likelihood is a Poisson likelihood where the observed and expected values are equal in each bin. Taking the likelihood ratio constructed by dividing the likelihood of the exponential fit by that of the saturated model, a χ^2 distribution is asymptotically approached [74][75]. This "χ^2" divided by the number of bins is then taken as a measure of the goodness of fit of the all-NoM model to each individual NoM slice. Figure 7.11 shows the "χ^2" divided by the number of bins using the all-NoM model in each NoM slice. Every NoM slice exhibits a good fit of the all-NoM model. The worst fit is in NoM 13-14, shown in Figure 7.10. This result justifies combining all NoM slices in the C region, and likewise for the A region, in order to have the correct normalization C/A as used in the background prediction.

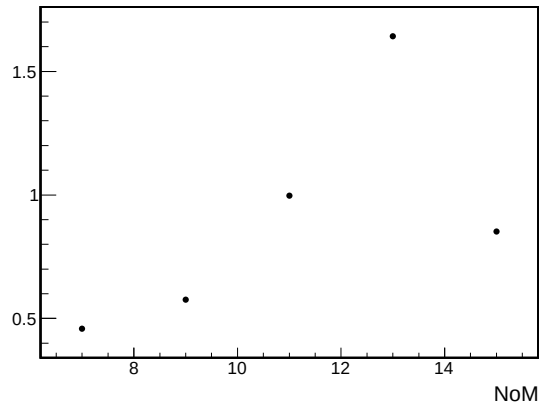

Figure 7.11: Plot of the saturated "χ^2" constructed from the ratio of the likelihood of the all-NoM exponential fit divided by the saturated model likelihood, normalized to the number of bins. The distribution is constructed from tracks passing preselection in 2011 data within $1.4 < |\eta| < 1.6$. This can be taken as the goodness of fit of the exponential all-NoM model to each slice.

To summarize the background procedure, each η/NoM slice defines a unique A and B region, regions A and C being sliced only in the pseudorapidity η. Each I_{as} bin B_k is examined, defining a minimum momentum to pass the mass cut, P_{min}. The P_{min} is used as the lower momentum bound on the C_k region. Then we assume $D'_k/B_k = C_k/A$ and calculate D'_k. For each B_k containing multiple I_h values we approximate $C_k =$

$\Sigma_j^{B_k} C_j / B_k$. Finally, using the approximation,

$$D'_k = \frac{B_k C_k}{A} = \frac{\Sigma_j^{B_k} C_j}{A} \tag{7.1}$$

where A and C are combined in NoM (sliced only in η). In this definition, the C region may overlap the A region but only for very low mass cuts, below those used in this analysis.

At high I_{as} values in each η/NoM slice, bins in the B region B_k are often empty. These bins are not expected to contain background events. However, in calculating the significance, the background-only model is used to calculate the likelihood for signal-like events which may populate these bins. To avoid the technical problem of zero background likelihood in these bins, we assume that the background likelihood falls exponentially in the high I_{as} region. The parameters of the exponential are determined by a binned likelihood fit of the last few nonzero I_{as} bins in the B region. Since the proper C_k region cannot be determined when B_k is zero, they are normalized in two ways. In the first approach, for limit-setting, the C_k is taken from the highest nonzero I_{as} bin. This will slightly underestimate the background, since C_k increases with I_{as}. Hence this will lead to less strict limits and is therefore conservative. In the second approach, for evaluation of the signal significance (discovery), the I_{as}/I_h correlation is taken from Minimum Bias triggered data and used to calculate C_k. If events are seen at high I_{as} values, discovery will be claimed regardless of the exact test statistic value, so this approximation is adequate. Finally, for high mass cuts, C_k can be zero as the minimum momentum to pass the mass cut is high. When C_k is zero, the background is taken as zero for the limit-setting case, again, being conservative. For the discovery case, C_k is taken to be 1. Figure 7.12 shows the data and the exponential fit in the B region in a single η/NoM slice for the GM Stau of mass 100 GeV, with a 20 GeV mass cut applied. The B region points and fit values are then scaled by C/A for the two cases, limit-setting and discovery, as described above. Figure 7.13 shows the prediction of the I_{as} distribution along with the data in the D' region for a sample η/NoM slice, both before and after a 20 GeV mass cut. In the case of such a low mass cut, a large background is present, and the background prediction is consistent with data containing no signal events, which validates the background prediction method. The agreement between data and prediction is good. After the I_{as} background

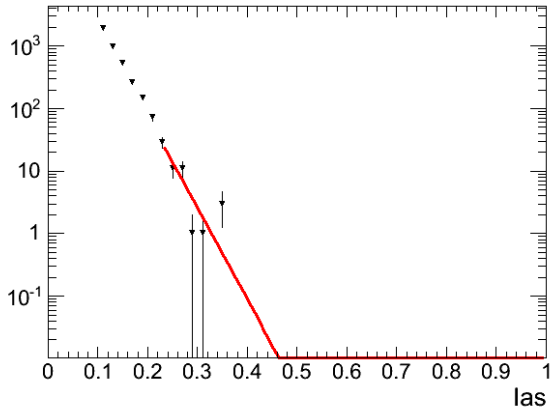

Figure 7.12: I_{as} distribution in the B region for a single η/NoM slice for the GM Stau of mass 100 GeV. The last few data points are used to fit an exponential (red) to obtain the distribution shape in the high I_{as} region.

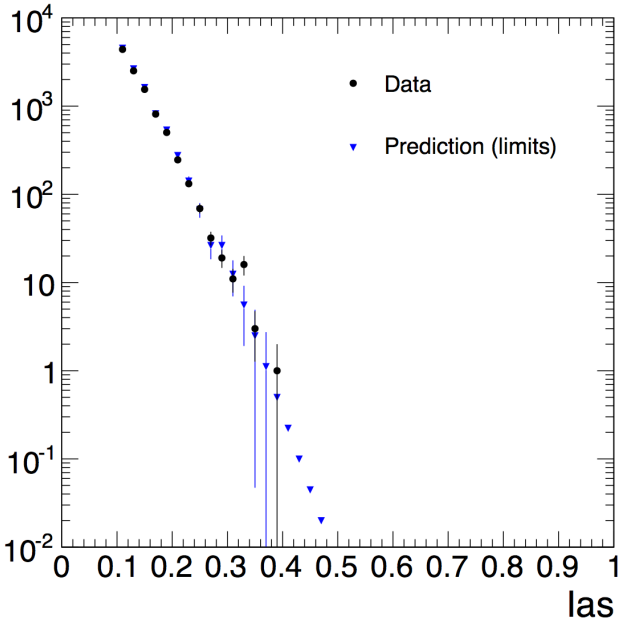

Figure 7.13: I_{as} prediction for limit setting and data in D' region for a single η/NoM slice. The loose mass cut of 20 GeV is here used as a loose cut to examine the agreement between prediction and observed data.

prediction has been constructed in each η/NoM slice, the I_{as} distribution for signal is created from the Monte Carlo simulation. Details of the datasets are given in [28]. The signal events are reweighted using the distribution of the number of primary vertices from the 2011 data. Because of the use of a tighter RPC Level-1 muon trigger during the first part of the 2011 run, two signal samples representing the two different data-taking periods are combined and weighted by the respective integrated luminosity. Figure 7.14 shows the I_{as} distributions from the prediction (discovery normalization) and the signal in one η/NoM slice for the GM Stau of mass 100 GeV.

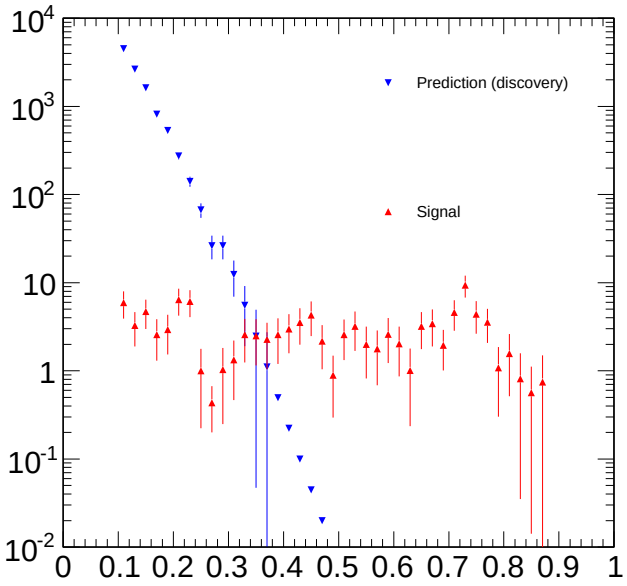

Figure 7.14: The I_{as} prediction for discovery and the signal in the D' region for a sample η/NoM slice. It can be seen that the background falls off rapidly, while the signal is very flat. The mass cut used is 20 GeV, corresponding to the GMStau of mass 100 GeV.

For use in the statistical tools, the distributions in each η/NoM slice are appended one after another into a single "unrolled" histogram. These signal and background histograms are then used by RooStats to set cross section limits and evaluate the potential signal significance as described below [76]. A RooStats model is constructed using the HistFactory tool, built into RooStats, which provides handling of overall and shape

systematic uncertainties, the latter via interpolation.

7.7 Likelihood Fitting and Results

For limit-setting, we use the profile likelihood ratio defined as:

$$\lambda(\mu) = \frac{L(B + \mu S, \hat{\hat{\boldsymbol{\theta}}})}{L(B + \hat{\mu} S, \hat{\boldsymbol{\theta}})} \tag{7.2}$$

Here μ is the trial signal cross section value and θ represents the nuisance parameters. The nuisance parameters are additional constraints on the likelihood function that typically result from studies of the systematic uncertainties, such as uncertainty on the background or signal prediction shape. The $\hat{\mu}$ and $\hat{\theta}$ are the μ and θ values which maximize the unconditional likelihood, and the double hat represents the nuisance parameter values which maximize the likelihood for a given μ (trial cross section). In order to perform a hypothesis test, one defines a critical region such that there is no more than a small probability of observing data there under the assumption of that hypothesis. The critical region can be constructed using a decision boundary defined using a test statistic. The observed value of the test statistic then determines whether one accepts or rejects the hypothesis. Here, we use a one-sided test statistic:

$$q_\mu = -2 \ln \lambda(\mu), \; \hat{\mu} \leq \mu \tag{7.3}$$

where q_μ is zero for $\hat{\mu} > \mu$. The tail-probability or p-value measures the agreement between the data and the trial μ value, also called the Confidence Level. For an observed value of $q_\mu = q_{\mu,\text{obs}}$:

$$CL_{s+b} = p_\mu = \int_{q_{\mu,\text{obs}}}^{\infty} f\left(q_\mu|\mu\right) \, dq_\mu \tag{7.4}$$

where $f\left(q_\mu|\mu\right)$ is the test statistic distribution under the background+signal hypothesis with trial cross section value μ. CL_b is defined in a similar way using the test statistic distribution under the background-only hypothesis.

To obtain the distributions f of the test statistic under the background-only and background+signal hypotheses, pseudoexperiments are generated as a function of the trial cross section value μ. Nuisance parameters are handled in a pure frequentist fashion, as global observables. Then the CL_s is calculated using the relation $CL_s =$

$CLs + b/CL_b$ [77]. Using the CL_s allows some protection against making an exclusion in a region where there is no sensitivity, i.e., when the test statistic distributions are highly overlapping in the background-only and background+signal cases. Figure 7.15 shows the test statistic distribution for the gluino model of mass 1000 GeV under the background-only (blue) and background+signal (red) hypotheses, with a trial cross section of 0.003 pb. The $CLs + b$ and CL_b regions are indicated by the red and blue shading, respectively. The black line indicates the observed value $q_{\mu,\text{obs}}$. In general this is calculated once from the real data, but to get the "expected" limits one assumes that the data will look like background, and so the $q_{\mu,\text{obs}}$ is taken as the median of the background-only test statistic distribution. The trial cross section at which

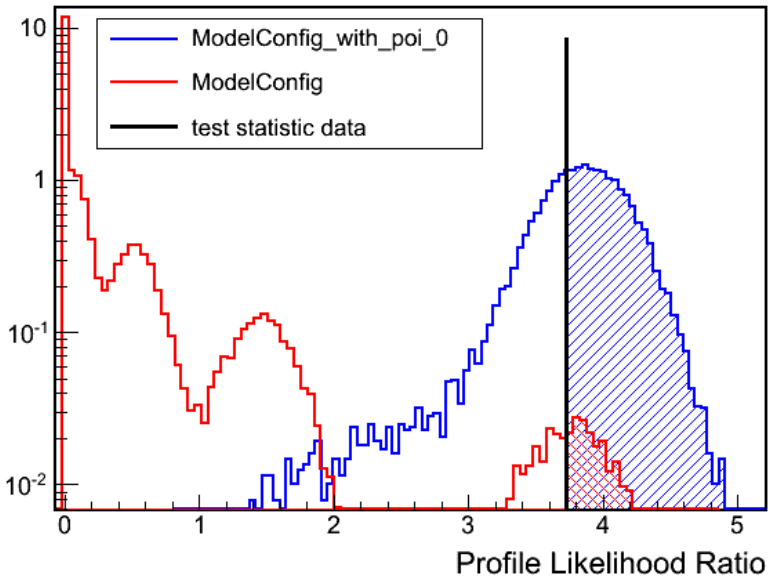

Figure 7.15: The test statistic distributions for the gluino model of 1000 GeV mass for the background-only (blue) and background+signal (red) hypotheses. A trial cross section of 0.003 pb is used. The CL_{s+b} is indicated by the red shaded region, while the CL_b is illustrated with the blue shaded region. The black line ("test statistic data") indicates the median value of the test statistic under the background-only hypothesis, which is used to calculate the "expected" limits.

the CL_s p-value is 0.05 is the 95% confidence level cross section upper limit. Figure 7.16 shows the CL_s p-value as a function of the trial cross section for the GMSB stau

of mass 432 GeV, and Figure 7.17 for the gluino of mass 1000 GeV.

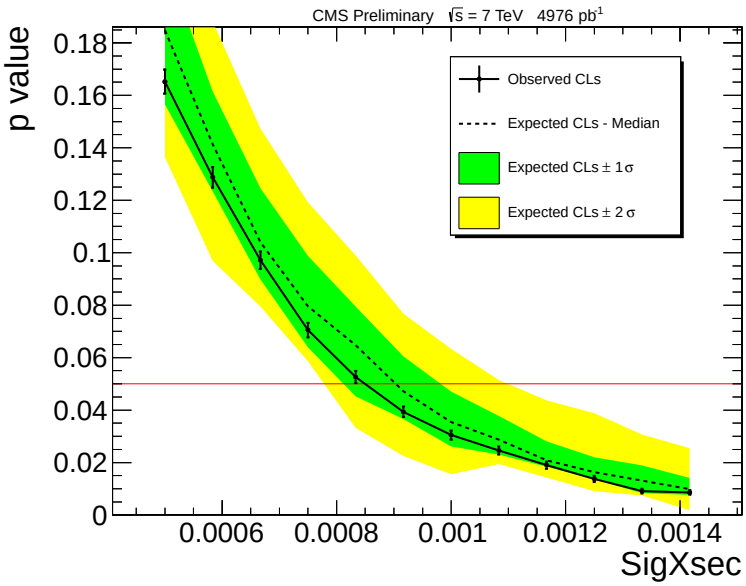

Figure 7.16: CL_s p-value vs. trial cross section ("SigXsec" in pb) for the GMSB stau of mass 432 GeV. For each trial cross section point, 40000 toy pseudoexperiments are generated to determine the distribution of the profile likelihood ratio test statistic under the background+signal hypothesis. The intersection of the p-value line at 0.05 with the CL_s curve yields the 95% confidence level upper limit on the signal cross section. The observed limit (solid line) and expected limit (hashed line) are shown along with the $\pm 1\sigma$ (green) and $\pm 2\sigma$ (yellow) uncertainty on the expected limit.

The limit-setting procedure is used to obtain the cross section upper limit for each point. A summary table with the results for all models considered is given in Tables 7.2 and 7.3.

The expected limits are better than the cut-and-count analysis by a factor of 1.1 to 1.4 for most mass points. A comparison for all models considered is listed in Tables 7.4 and 7.5.

The ratio of the cut-and-count analysis' expected 95% confidence level upper limits to those expected from the shape analysis is plotted as a function of the signal mass in Figure 7.18. The gain is largest for the 200 GeV mass points, where the I_{as} cut is high for the cut-and-count analysis, since for best results in the cut-and-count approach, the expected background must be decreased to close to 1 event. As the mass increases,

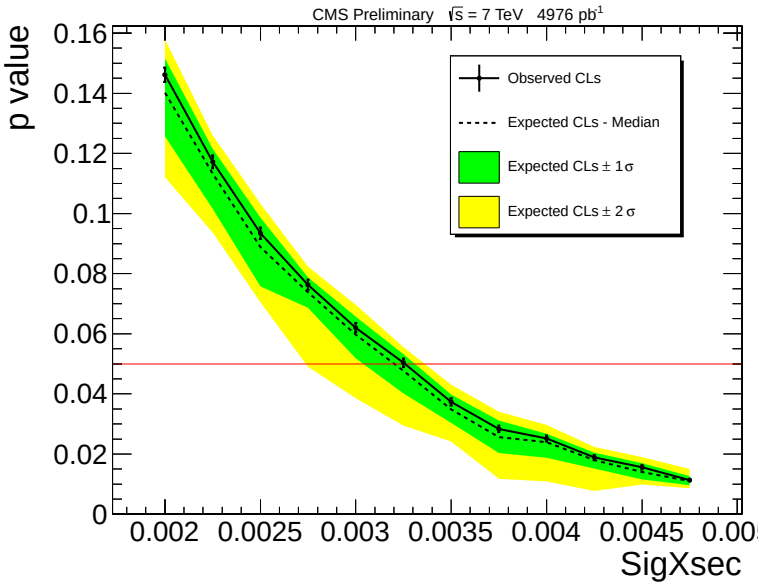

Figure 7.17: CL_s p-value vs. trial cross section ("SigXsec" in pb) for the gluino of mass 1000 GeV. For each trial cross section point, 40000 toy pseudoexperiments are generated to determine the distribution of the profile likelihood ratio test statistic under the background+signal hypothesis. The intersection of the p-value line at 0.05 with the CL_s curve yields the 95% confidence level upper limit on the signal cross section. The observed limit (solid line) and expected limit (hashed line) are shown along with the $\pm 1\sigma$ (green) and $\pm 2\sigma$ (yellow) uncertainty on the expected limit.

Model	$\mathbf{M_{reco}}$	**Sig. Eff.**	**Back. Exp.**	**Obs.**	**Th.** σ	**Exp.** σ	**Obs.** σ
$\tilde{g}$ 300	180	0.21	480.3±2.9	502	6.6E+01	3.3E-03	3.2E-03
$\tilde{g}$ 400	230	0.23	154.6±1.2	153	1.1E+01	2.9E-03	2.8E-03
$\tilde{g}$ 500	290	0.23	49.4±0.6	32	2.5E+00	2.7E-03	2.5E-03
$\tilde{g}$ 600	360	0.23	15.2±0.3	17	6.9E-01	2.6E-03	2.6E-03
$\tilde{g}$ 700	410	0.22	7.8±0.2	47	2.1E-01	2.5E-03	2.5E-03
$\tilde{g}$ 800	460	0.22	4.6±0.2	7	7.2E-02	2.6E-03	2.6E-03
$\tilde{g}$ 900	500	0.2	3.1±0.1	10	2.6E-02	2.8E-03	3.0E-03
$\tilde{g}$ 1000	540	0.18	2.2±0.1	7	9.9E-03	3.2E-03	3.3E-03
$\tilde{g}$ 1100	570	0.16	1.7±0.1	6	3.9E-03	3.6E-03	3.8E-03
$\tilde{g}$ 1200	600	0.14	1.2±0.1	7	1.5E-03	4.3E-03	4.5E-03
$\tilde{t}$ 200	130	0.2	1958.1±10.1	1949	1.3E+01	3.9E-03	3.8E-03
$\tilde{t}$ 300	190	0.23	376.3±2.4	643	1.3E+00	3.1E-03	2.9E-03
$\tilde{t}$ 400	250	0.25	103.9±0.9	127	2.2E-01	2.6E-03	2.5E-03
$\tilde{t}$ 500	310	0.29	34.5±0.5	38	4.8E-02	2.1E-03	2.1E-03
$\tilde{t}$ 600	360	0.3	15.2±0.3	20	1.3E-02	2.0E-03	2.0E-03
$\tilde{t}$ 700	410	0.3	7.8±0.2	16	3.6E-03	1.9E-03	2.0E-03
$\tilde{t}$ 800	450	0.31	5.0±0.2	11	1.1E-03	1.8E-03	1.9E-03
$\tilde{\tau}$ 200	120	0.58	2734.4±13.8	2747	1.2E-02	1.6E-03	1.7E-03
$\tilde{\tau}$ 247	150	0.64	1065.9±5.8	1058	3.4E-03	1.3E-03	1.2E-03
$\tilde{\tau}$ 308	190	0.68	376.3±2.4	384	9.8E-04	1.1E-03	1.0E-03
$\tilde{\tau}$ 370	230	0.71	154.6±1.2	153	3.5E-04	9.9E-04	9.6E-04
$\tilde{\tau}$ 432	260	0.73	85.8±0.8	68	1.4E-04	9.0E-04	8.5E-04
$\tilde{\tau}$ 494	300	0.77	41.2±0.5	28	6.2E-05	8.4E-04	7.9E-04

Table 7.2: Results of the analysis for gluinos, stops, and staus (masses in GeV): cut on reconstructed mass in GeV ("M_{reco}"), signal efficiency ("Sig. Eff."), number of candidates expected from background ("Back. Exp."), number of observed candidates ("Obs."), theoretical cross section ("Th. σ"), expected median 95% confidence level upper limit on cross section assuming the background-only hypothesis ("Exp. σ"), observed 95% confidence level upper limit on cross section ("Obs. σ"), expected minimum cross section to make a discovery of significance at the level of five standard deviations ("Disc. σ"). The units of cross section are pb.

Model	$\mathbf{M_{reco}}$	**Sig. Eff.**	**Back. Exp.**	**Obs.**	**Th.** σ	**Exp.** σ	**Obs.** σ
$\tilde{g}$ 300N	180	0.03	480.3±2.9	502	6.6E+01	2.3E-02	2.3E-02
$\tilde{g}$ 400N	230	0.05	154.6±1.2	153	1.1E+01	1.5E-02	1.6E-02
$\tilde{g}$ 500N	290	0.05	49.4±0.6	32	2.5E+00	1.3E-02	1.2E-02
$\tilde{g}$ 600N	330	0.05	24.5±0.4	17	6.9E-01	1.1E-02	1.1E-02
$\tilde{g}$ 700N	270	0.05	71.2±0.7	47	2.1E-01	1.1E-02	1.1E-02
$\tilde{g}$ 800N	400	0.05	8.8±0.2	7	7.2E-02	1.1E-02	1.1E-02
$\tilde{g}$ 900N	380	0.05	11.5±0.3	10	2.6E-02	1.1E-02	1.1E-02
$\tilde{g}$ 1000N	410	0.04	7.8±0.2	7	9.9E-03	1.3E-02	1.3E-02
$\tilde{g}$ 1100N	460	0.04	4.6±0.2	6	3.9E-03	1.5E-02	1.5E-02
$\tilde{g}$ 1200N	400	0.03	8.8±0.2	7	1.5E-03	1.7E-02	1.7E-02
$\tilde{t}$ 200N	120	0.03	2734.4±13.8	2747	1.3E+01	2.5E-02	2.5E-02
$\tilde{t}$ 300N	170	0.06	619.1±3.6	643	1.3E+00	1.3E-02	1.3E-02
$\tilde{t}$ 400N	240	0.07	126.3±1.1	127	2.2E-01	1.0E-02	9.6E-03
$\tilde{t}$ 500N	280	0.08	59.2±0.6	38	4.8E-02	8.1E-03	7.9E-03
$\tilde{t}$ 600N	320	0.08	29.0±0.4	20	1.3E-02	7.3E-03	7.2E-03
$\tilde{t}$ 700N	350	0.09	17.7±0.3	16	3.6E-03	6.8E-03	6.7E-03
$\tilde{t}$ 800N	370	0.09	13.2±0.3	11	1.1E-03	6.6E-03	6.4E-03

Table 7.3: Results of the analysis for gluinos and staus (masses in GeV): cut on reconstructed mass in GeV ("M_{reco}"), signal efficiency ("Sig. Eff."), number of candidates expected from background ("Back. Exp."), number of observed candidates ("Obs."), theoretical cross section ("Th. σ"), expected median 95% confidence level upper limit on cross section assuming the background-only hypothesis ("Exp. σ"), observed 95% confidence level upper limit on cross section ("Obs. σ"), expected minimum cross section to make a discovery of significance at the level of five standard deviations ("Disc. σ"). The "N" after the mass indicates that the charge-suppression nuclear interaction model was used. The units of cross section are pb.

Model	**Exp. σ Ct.**	**Exp. σ Sh.**	**Exp. σ Ct./Sh.**
$\tilde{g}$ 300	3.8E-03	3.3E-03	1.15
$\tilde{g}$ 400	3.3E-03	2.9E-03	1.14
$\tilde{g}$ 500	3.1E-03	2.7E-03	1.15
$\tilde{g}$ 600	3.0E-03	2.6E-03	1.16
$\tilde{g}$ 700	3.0E-03	2.5E-03	1.18
$\tilde{g}$ 800	3.0E-03	2.6E-03	1.14
$\tilde{g}$ 900	3.2E-03	2.8E-03	1.14
$\tilde{g}$ 1000	3.5E-03	3.2E-03	1.09
$\tilde{g}$ 1100	4.0E-03	3.6E-03	1.11
$\tilde{g}$ 1200	4.8E-03	4.3E-03	1.12
$\tilde{t}$ 200	5.8E-03	3.9E-03	1.47
$\tilde{t}$ 300	3.4E-03	3.1E-03	1.09
$\tilde{t}$ 400	2.8E-03	2.6E-03	1.07
$\tilde{t}$ 500	2.4E-03	2.1E-03	1.12
$\tilde{t}$ 600	2.4E-03	2.0E-03	1.22
$\tilde{t}$ 700	2.3E-03	1.9E-03	1.21
$\tilde{t}$ 800	2.1E-03	1.8E-03	1.16
$\tilde{\tau}$ 200	2.3E-03	1.6E-03	1.42
$\tilde{\tau}$ 247	1.4E-03	1.3E-03	1.1
$\tilde{\tau}$ 308	1.2E-03	1.1E-03	1.11
$\tilde{\tau}$ 370	1.1E-03	9.9E-04	1.11
$\tilde{\tau}$ 432	1.0E-03	9.0E-04	1.11
$\tilde{\tau}$ 494	9.3E-04	8.4E-04	1.11

Table 7.4: Expected 95% CL cross section limit for the counting experiment ("Exp. σ Ct.") and for the shape-based analysis ("Exp. σ Sh."); ratios of counting experiment to shape-based analysis for expected 95% CL cross section limits ("Exp. σ Ct./Sh."). The units of cross section are pb.

Model	**Exp. σ Ct.**	**Exp. σ Sh.**	**Exp. σ Ct./Sh.**
$\tilde{g}$ 300N	3.0E-02	2.3E-02	1.29
$\tilde{g}$ 400N	1.8E-02	1.5E-02	1.19
$\tilde{g}$ 500N	1.6E-02	1.3E-02	1.25
$\tilde{g}$ 600N	1.3E-02	1.1E-02	1.2
$\tilde{g}$ 700N	1.4E-02	1.1E-02	1.26
$\tilde{g}$ 800N	1.4E-02	1.1E-02	1.27
$\tilde{g}$ 900N	1.4E-02	1.1E-02	1.24
$\tilde{g}$ 1000N	1.6E-02	1.3E-02	1.24
$\tilde{g}$ 1100N	1.9E-02	1.5E-02	1.24
$\tilde{g}$ 1200N	2.3E-02	1.7E-02	1.35
$\tilde{t}$ 200N	4.0E-02	2.5E-02	1.57
$\tilde{t}$ 300N	1.5E-02	1.3E-02	1.11
$\tilde{t}$ 400N	1.2E-02	1.0E-02	1.2
$\tilde{t}$ 500N	9.1E-03	8.1E-03	1.13
$\tilde{t}$ 600N	8.3E-03	7.3E-03	1.14
$\tilde{t}$ 700N	8.3E-03	6.8E-03	1.22
$\tilde{t}$ 800N	8.1E-03	6.6E-03	1.23

Table 7.5: Expected 95% CL cross section limit for the counting experiment ("Exp. σ Ct.") and for the shape-based analysis ("Exp. σ Sh."); ratios of counting experiment to shape-based analysis for expected 95% CL cross section limits ("Exp. σ Ct./Sh."). The "N" after the mass indicates that the charge-suppression nuclear interaction model was used. The units of cross section are pb.

the gain becomes less, since the cut-and-count analysis' I_{as} cut can be looser and still result in expected background below 1 event. Here adding shape information does not result in much gain. With more integrated luminosity, and the corresponding increase in expected background, the shape analysis should gain in limit-setting power for higher mass points.

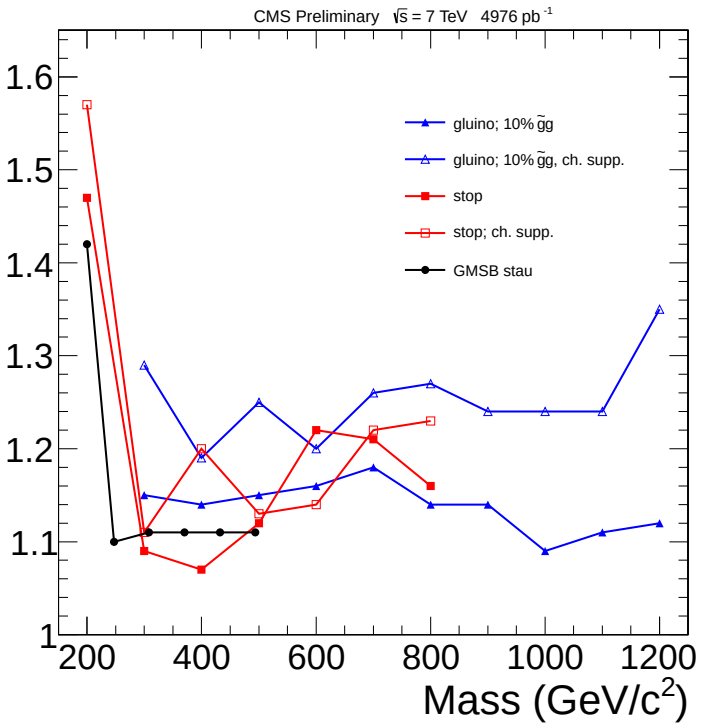

Figure 7.18: Ratio of expected standard analysis 95% confidence upper limit on the HSCP cross section to that expected from the shape-based method. The largest gain comes at the 200 GeV mass point, where the counting experiment's I_{as} cut is higher.

The cross section upper limits for each model can be plotted as a function of mass. By comparing to the theoretical predictions for the production cross section, one can set limits on the mass. Figure 7.19 shows the cross section as a function of mass for gluinos, stops, and GM staus. The gluinos and stops are considered using both the nominal nuclear interaction model, and the charge suppression model. The mass limits are: 1101 GeV for the gluinos (0.1 glueball fraction), 750 GeV for stops, and 306 GeV for staus. For the charge suppression models, the mass limits are 975 GeV for gluinos

(0.1 glueball fraction) and 646 GeV for stops.

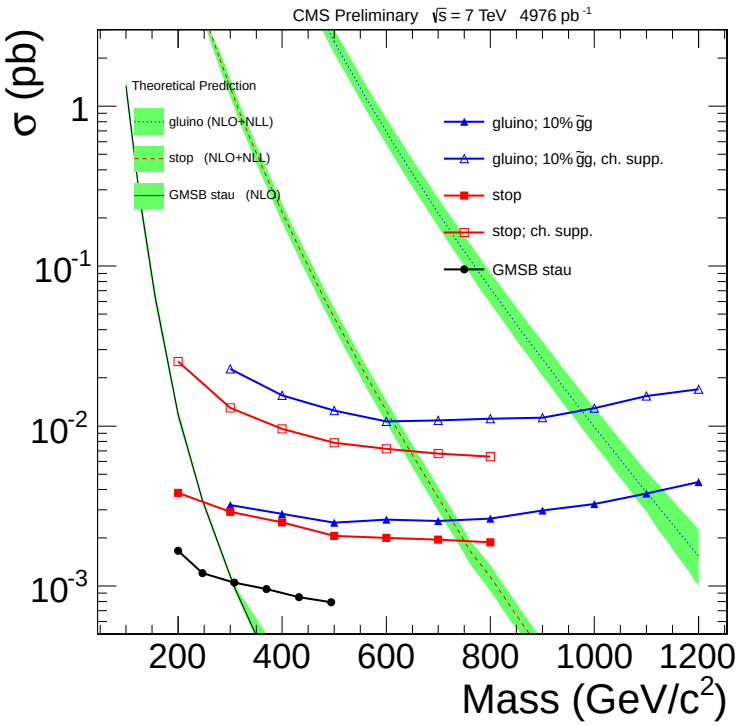

Figure 7.19: Observed cross section upper limits at the 95% confidence level vs. the mass of the signal candidate for gluinos, stops, and staus.

The discovery potential, or the minimum cross section needed for a 5σ discovery has also been calculated. Here the median test statistic value from signal+background pseudoexperiments at a given trial cross section is compared to the background-only test statistic distribution. One finds the trial cross section from background+signal pseudoexperiments that corresponds to a CLs p-value of 2.87×10^{-7} or 5σ deviation from the background-only pseudoexperiments. The test statistic used here is defined as:

$$q_0 = -2 \ln \lambda(0), \, \hat{\mu} \geq 0 \tag{7.5}$$

where q_0 is zero for $\hat{\mu} < 0$. Here the asymptotic approximation for the profile likelihood ratio is used to obtain the discovery significance of particular cross section values [78]. The asymptotic approach was chosen because the alternative requires generating large numbers of pseudoexperiments and is not practical for covering all models and

mass points. By comparing the asymptotic results with those from pseudoexperiments, one can judge the applicability of the asymptotic approximation for this particular background model. It was found that the asymptotic results are at most a factor of 1.5 smaller than that obtained from pseudoexperiments, so the former are scaled by a factor of 1.5 in all cases. A range of trial cross section values are used for the background+signal pseudoexperiments and the results are interpolated to find the minimum 5σ discovery signal cross section. The results are shown in Tables 7.6 and 7.7.
The minimum cross sections are smaller by a factor of about 1.5 to 3 compared to the cut and count analysis, illustrating that the shape-based method is significantly more sensitive to the presence of HSCP signals. The comparison of the minimum discovery cross sections is given in Tables 7.8 and 7.9.

In Figure 7.20 the ratio of the expected minimum discovery cross section for the standard analysis to that expected from the shape-based method is plotted as a function of mass for all models considered. The gain has a minimum for models with about 400 GeV mass, before increasing as the mass increases. For the low mass points, the gain comes from the fact that the I_{as} cut in the cut-and-count analysis is much tighter than that used here. In the cut-and-count case, the tight I_{as} cut reduces the expected background level, which in turn optimizes the discovery potential. For the higher mass points, the gain increases as the I_{as} for signal concentrates more and more in the high I_{as} region. For the intermediate mass points, the I_{as} for signal is still fairly flat, and the standard analysis I_{as} cut is loose, so the gain is less.

7.8 Systematic Uncertainties

This analysis requires an accurate simulation of the signal behavior in order to determine the dE/dx shape. The level of uncertainty in the signal simulation was studied for several important effects. Some of the descriptions of these effects overlaps with those in the cut-and-count analysis [28].

The trigger efficiency was examined for both the single muon and missing energy triggers. The single muon trigger efficiency varied by up to 5% between simulation and data for all energies considered [50]. When searching for late-arriving particles, the simulation of the muon trigger electronics synchronization also contributes to the

Model	$\mathbf{M_{reco}}$	**Sig. Eff.**	**Th.** σ	**Exp.** σ	**Obs.** σ	**Disc.** σ
$\tilde{g}$ 300	180	0.21	6.6E+01	3.3E-03	3.2E-03	4.1E-03
$\tilde{g}$ 400	230	0.23	1.1E+01	2.9E-03	2.8E-03	3.2E-03
$\tilde{g}$ 500	290	0.23	2.5E+00	2.7E-03	2.5E-03	2.6E-03
$\tilde{g}$ 600	360	0.23	6.9E-01	2.6E-03	2.6E-03	2.3E-03
$\tilde{g}$ 700	410	0.22	2.1E-01	2.5E-03	2.5E-03	2.1E-03
$\tilde{g}$ 800	460	0.22	7.2E-02	2.6E-03	2.6E-03	2.0E-03
$\tilde{g}$ 900	500	0.2	2.6E-02	2.8E-03	3.0E-03	2.0E-03
$\tilde{g}$ 1000	540	0.18	9.9E-03	3.2E-03	3.3E-03	2.1E-03
$\tilde{g}$ 1100	570	0.16	3.9E-03	3.6E-03	3.8E-03	2.2E-03
$\tilde{g}$ 1200	600	0.14	1.5E-03	4.3E-03	4.5E-03	2.4E-03
$\tilde{t}$ 200	130	0.2	1.3E+01	3.9E-03	3.8E-03	6.1E-03
$\tilde{t}$ 300	190	0.23	1.3E+00	3.1E-03	2.9E-03	3.8E-03
$\tilde{t}$ 400	250	0.25	2.2E-01	2.6E-03	2.5E-03	2.9E-03
$\tilde{t}$ 500	310	0.29	4.8E-02	2.1E-03	2.1E-03	2.2E-03
$\tilde{t}$ 600	360	0.3	1.3E-02	2.0E-03	2.0E-03	1.9E-03
$\tilde{t}$ 700	410	0.3	3.6E-03	1.9E-03	2.0E-03	1.6E-03
$\tilde{t}$ 800	450	0.31	1.1E-03	1.8E-03	1.9E-03	1.4E-03
$\tilde{\tau}$ 200	120	0.58	1.2E-02	1.6E-03	1.7E-03	2.5E-03
$\tilde{\tau}$ 247	150	0.64	3.4E-03	1.3E-03	1.2E-03	1.9E-03
$\tilde{\tau}$ 308	190	0.68	9.8E-04	1.1E-03	1.0E-03	1.4E-03
$\tilde{\tau}$ 370	230	0.71	3.5E-04	9.9E-04	9.6E-04	1.2E-03
$\tilde{\tau}$ 432	260	0.73	1.4E-04	9.0E-04	8.5E-04	9.7E-04
$\tilde{\tau}$ 494	300	0.77	6.2E-05	8.4E-04	7.9E-04	8.5E-04

Table 7.6: Results of the analysis for gluinos, stops, and staus (masses in GeV): cut on reconstructed mass in GeV ("M_{reco}"), signal efficiency ("Sig. Eff."), theoretical cross section ("Th. σ"), expected median 95% confidence level upper limit on cross section assuming the background-only hypothesis ("Exp. σ"), observed 95% confidence level upper limit on cross section ("Obs. σ"), expected minimum cross section to make a discovery of significance at the level of five standard deviations ("Disc. σ"). The units of cross section are pb.

Model	$\mathbf{M_{reco}}$	**Sig. Eff.**	**Th.** σ	**Exp.** σ	**Obs.** σ	**Disc.** σ
$\tilde{g}$ 300N	180	0.03	6.6E+01	2.3E-02	2.3E-02	2.7E-02
$\tilde{g}$ 400N	230	0.05	1.1E+01	1.5E-02	1.6E-02	1.6E-02
$\tilde{g}$ 500N	290	0.05	2.5E+00	1.3E-02	1.2E-02	1.2E-02
$\tilde{g}$ 600N	330	0.05	6.9E-01	1.1E-02	1.1E-02	9.8E-03
$\tilde{g}$ 700N	270	0.05	2.1E-01	1.1E-02	1.1E-02	1.0E-02
$\tilde{g}$ 800N	400	0.05	7.2E-02	1.1E-02	1.1E-02	8.5E-03
$\tilde{g}$ 900N	380	0.05	2.6E-02	1.1E-02	1.1E-02	8.5E-03
$\tilde{g}$ 1000N	410	0.04	9.9E-03	1.3E-02	1.3E-02	9.4E-03
$\tilde{g}$ 1100N	460	0.04	3.9E-03	1.5E-02	1.5E-02	9.9E-03
$\tilde{g}$ 1200N	400	0.03	1.5E-03	1.7E-02	1.7E-02	1.2E-02
$\tilde{t}$ 200N	120	0.03	1.3E+01	2.5E-02	2.5E-02	3.9E-02
$\tilde{t}$ 300N	170	0.06	1.3E+00	1.3E-02	1.3E-02	1.6E-02
$\tilde{t}$ 400N	240	0.07	2.2E-01	1.0E-02	9.6E-03	1.1E-02
$\tilde{t}$ 500N	280	0.08	4.8E-02	8.1E-03	7.9E-03	7.8E-03
$\tilde{t}$ 600N	320	0.08	1.3E-02	7.3E-03	7.2E-03	6.7E-03
$\tilde{t}$ 700N	350	0.09	3.6E-03	6.8E-03	6.7E-03	5.9E-03
$\tilde{t}$ 800N	370	0.09	1.1E-03	6.6E-03	6.4E-03	5.6E-03

Table 7.7: Results of the analysis for gluinos and staus (masses in GeV): cut on reconstructed mass in GeV ("M_{reco}"), signal efficiency ("Sig. Eff."), theoretical cross section ("Th. σ"), expected median 95% confidence level upper limit on cross section assuming the background-only hypothesis ("Exp. σ"), observed 95% confidence level upper limit on cross section ("Obs. σ"), expected minimum cross section to make a discovery of significance at the level of five standard deviations ("Disc. σ"). The "N" after the mass indicates that the charge-suppression nuclear interaction model was used. The units of cross section are pb.

Model	**Disc. σ Ct.**	**Disc. σ Sh.**	**Disc. σ Ct./Sh.**
$\tilde{g}$ 300	8.5E-03	4.1E-03	2.08
$\tilde{g}$ 400	5.5E-03	3.2E-03	1.73
$\tilde{g}$ 500	5.2E-03	2.6E-03	1.98
$\tilde{g}$ 600	4.8E-03	2.3E-03	2.13
$\tilde{g}$ 700	4.8E-03	2.1E-03	2.32
$\tilde{g}$ 800	4.9E-03	2.0E-03	2.49
$\tilde{g}$ 900	5.2E-03	2.0E-03	2.63
$\tilde{g}$ 1000	5.7E-03	2.1E-03	2.77
$\tilde{g}$ 1100	6.6E-03	2.2E-03	3.06
$\tilde{g}$ 1200	7.6E-03	2.4E-03	3.12
$\tilde{t}$ 200	1.4E-02	6.1E-03	2.31
$\tilde{t}$ 300	6.7E-03	3.8E-03	1.75
$\tilde{t}$ 400	4.8E-03	2.9E-03	1.68
$\tilde{t}$ 500	4.0E-03	2.2E-03	1.86
$\tilde{t}$ 600	3.8E-03	1.9E-03	2.05
$\tilde{t}$ 700	3.6E-03	1.6E-03	2.25
$\tilde{t}$ 800	3.4E-03	1.4E-03	2.39
$\tilde{\tau}$ 200	5.7E-03	2.5E-03	2.24
$\tilde{\tau}$ 247	3.7E-03	1.9E-03	1.96
$\tilde{\tau}$ 308	2.3E-03	1.4E-03	1.67
$\tilde{\tau}$ 370	1.8E-03	1.2E-03	1.56
$\tilde{\tau}$ 432	1.7E-03	9.7E-04	1.75
$\tilde{\tau}$ 494	1.5E-03	8.5E-04	1.76

Table 7.8: Comparison between shape-based and counting experiment results: expected minimum cross section to make a 5σ discovery for the counting experiment ("Disc. σ Ct.") and that for the shape-based analysis ("Disc. σ Sh."); ratios of counting experiment to shape-based analysis for minimum cross section for 5σ discovery ("Disc. σ Ct./Sh.). The units of cross section are pb.

Model	**Disc. σ Ct.**	**Disc. σ Sh.**	**Disc. σ Ct./Sh.**
$\tilde{g}$ 300N	6.8E-02	2.7E-02	2.49
$\tilde{g}$ 400N	3.0E-02	1.6E-02	1.91
$\tilde{g}$ 500N	2.7E-02	1.2E-02	2.26
$\tilde{g}$ 600N	2.2E-02	9.8E-03	2.24
$\tilde{g}$ 700N	2.2E-02	1.0E-02	2.11
$\tilde{g}$ 800N	2.2E-02	8.5E-03	2.58
$\tilde{g}$ 900N	2.2E-02	8.5E-03	2.59
$\tilde{g}$ 1000N	2.6E-02	9.4E-03	2.77
$\tilde{g}$ 1100N	3.1E-02	9.9E-03	3.14
$\tilde{g}$ 1200N	3.6E-02	1.2E-02	3.02
$\tilde{t}$ 200N	1.0E-01	3.9E-02	2.53
$\tilde{t}$ 300N	3.4E-02	1.6E-02	2.1
$\tilde{t}$ 400N	1.9E-02	1.1E-02	1.79
$\tilde{t}$ 500N	1.5E-02	7.8E-03	1.92
$\tilde{t}$ 600N	1.4E-02	6.7E-03	2.1
$\tilde{t}$ 700N	1.3E-02	5.9E-03	2.2
$\tilde{t}$ 800N	1.3E-02	5.6E-03	2.31

Table 7.9: Comparison between shape-based and counting experiment results: expected minimum cross section to make a 5σ discovery for the counting experiment ("Disc. σ Ct.") and that for the shape-based analysis ("Disc. σ Sh."); ratios of counting experiment to shape-based analysis for minimum cross section for 5σ discovery ("Disc. σ Ct./Sh.). The "N" after the mass indicates that the charge-suppression nuclear interaction model was used. The units of cross section are pb.

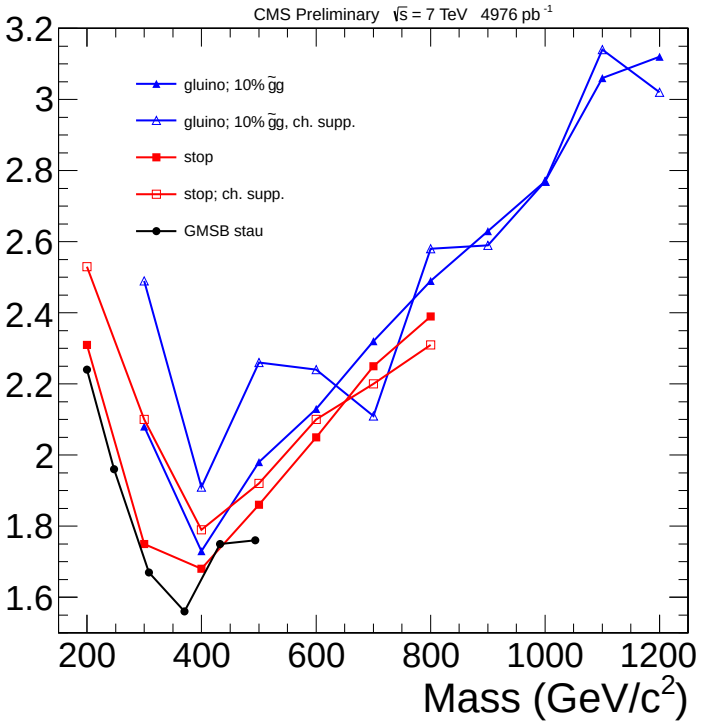

Figure 7.20: Ratio of expected standard analysis minimum discovery cross section to that expected from the shape-based method. The highest gain comes for the highest-mass HSCP, where the signal I_{as} distribution concentrates more and more in the high I_{as} region. The shape-based analysis takes advantage of the increasing difference in the I_{as} distributions between signal and background.

trigger efficiency uncertainty. This effect was quantified by using the synchronization from data and comparing to that in simulation, and was found to result in a relative change in the efficiency of less than 2%. For the missing energy trigger, the jet energy scale and jet energy resolution uncertainties are the main effects. The jet energy scale uncertainty was found to be less than 3% across the energy range [79]. The charge suppression models are most sensitive to the missing energy trigger, as they most likely become neutral due to material interactions before reaching the muon system. The trigger efficiency varied by up to 5% for these models when changing the jet energy scale and resolution by +/- 1 standard deviation. The other models rely more on the muon trigger, and the same test shows a variation of only 2% in the trigger efficiency. Therefore, looking at all these results, an overall 5% uncertainty on the trigger efficiency is assigned for all models.

Pile-up, or the mean rate of interactions in each bunch crossing does not contribute significantly to the uncertainty on the signal efficiency compared to the statistical uncertainty from the available simulated signal events. The track reconstruction efficiency is uncertain to 2% [80].

The track momentum scale was studied by following a previous effort comparing muons from the decay of Z bosons between simulation and data [50]. Parameterizing the difference and minimizing, the following correction to simulation is obtained:

$$\frac{1}{P_T'} = \frac{1}{P_T} + \delta_{K_T}(q, \phi, \eta) \tag{7.6}$$

Here,

$$\delta_{K_T}(q, \phi, \eta) = a + b\eta^2 + dq\sin(\phi - \phi_0) \tag{7.7}$$

and q is the charge of the particle (± 1), a = 0.236 TeV^{-1}, b = -0.135 TeV^{-1}, d = 0.282 TeV^{-1}, and ϕ_0 = 1.337. By applying this shift to the simulation, the signal efficiency changed by about 4%. Therefore an overall 4% uncertainty is assigned for this effect.

The dE/dx considered here is both the I_h, which affects overall signal efficiency via the mass cut, and I_{as}, which affects the shape and the efficiency. To study the change in signal efficiency due to the uncertainty on the dE/dx scale, data taken with Minimum Bias triggers were used to compare the I_h and I_{as} distributions for low momentum protons. This showed that the I_h scale was in fact underestimated in the simulation by up to 5%. The I_{as} scale and resolution were both underestimated in the simulation. The

simulation I_{as} was shifted upward by 0.015 and smeared by 0.083 to account for this. Both I_h and I_{as} scale changes were applied at the same time, owing to the correlation between the two. In most cases, the signal efficiency increased overall, but some models displayed a decrease. Therefore the simulation is not corrected for this effect, and an overall 2% uncertainty is assigned, from the maximum observed efficiency decrease. The effect of the I_{as} shift on the shape of the signal I_{as} distribution is studied below. The efficiency change is included in the study of the shape change. Since we use I_h when we calculate the mass of each HSCP candidate, and the systematic scale uncertainties for I_h and I_{as} are correlated, we combine the systematic uncertainty in the efficiency due to I_h and I_{as} scales together. This leads to double counting of the efficiency uncertainty for the latter. We consider this an acceptable result due to the difficulty of separating the shape and efficiency effects, and the fact that this approach errs on the conservative side.

The above effects, on the overall normalization, were treated with a single gaussian constraint on the signal efficiency of 7%, as shown in Table 7.10. The remaining effects alter the shape of the I_{as} distribution. A more detailed study compared the I_{as} distribution for protons between simulation and data with Minimum Bias trigger conditions in slices of number of dE/dx measurements. The resulting shifts were applied to the simulation, and a new I_{as} shape obtained, which was then used in the limit computation. The limit results computed in this way fluctuated in a manner consistent with statistical fluctuation. Nevertheless, the shift is still taken into account as a coherent shape shift in the RooStats tool. Having obtained the shape applying the positive and negative shifts from the systematic effect, a quadratic interpolation is done between these two shapes and the nominal and used a constraint term in the likelihood function.

There is an uncertainty stemming from the background prediction function used in the high I_{as} region and the values of the fitted exponential slope. The choice of fit function was driven based on looking at the high I_{as} tail in the data after preselection. This is shown in Figure 7.21. The data in the high I_{as} tail region that is typically included in the fit begins where the I_{as} decreases about about 3-4 orders of magnitude from its peak at $I_{as} = 0$. This region is fitted with an exponential in Figure 7.21 with good results. Therefore the choice of an exponential function is reasonable. To

Source of systematic uncertainty	Relative uncertainty (%)
Signal efficiency:	
- Trigger efficiency	5
- Track reconstruction efficiency	< 2
- Track momentum scale	< 4
- Ionization energy loss I_h	2
- Pile-up	0.5
Total uncertainty on signal efficiency	7
Luminosity	2.2

Table 7.10: Systematic uncertainties and their determined relative uncertainties.

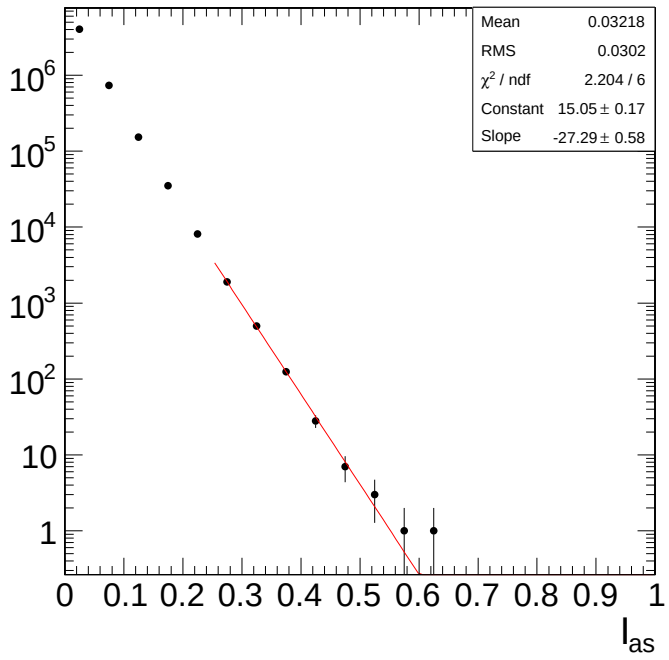

Figure 7.21: I_{as} distribution in the data after preselections have been applied. It is seen that for the high I_{as} tail, an exponential function fits the data well.

account for the uncertainty on the fitted exponential slope parameter, the background shape was varied coherently by adding and subtracting the error on the slope parameter from its nominal value.

The uncertainty on the value of I_{as} in each bin in the prediction is driven by the uncertainty on the number of tracks in the B region in that bin. The C/A ratio can be seen as a measure of how significant the B region statistical uncertainty is relative to that in the search region. The B region statistical error, when scaled by C/A, can become significant. In the case where the mass cut is high and the resulting minimum momentum cut high, the statistical error of the D' region is small relative to that of the BC/A prediction. In this case, C/A < 1. When the mass cut is low, C/A > 1, and the statistical uncertainty on the number of events in the search region will be small, while that in the B region will be large. This occurs with the small cut values used for models with masses less than about 200 GeV, which are not considered in this analysis.

A detector-related effect is the modeling of the number of dE/dx measurements (NoM) in simulation. This effect could cause the distribution of HSCP tracks among the NoM slice to vary between data and simulation. To study this effect, the NoM distributions are compared from a sample of data from the C region sideband and simulated Drell-Yan events decaying to dimuons, as shown in Figure 7.22. The simulation seems to predict more measurements per track than the data, which means that events fail the preselection more often in data than in the simulation. The difference in average NoM between simulation and data yields an additional 1.5% efficiency loss in data for every dE/dx measurement in simulation. This implies an efficiency loss of less than 0.2%, which is negligible. In order to account for the effect of the NoM shape variation, the simulation is adjusted by the data/MC difference and then included as a coherent shift in the signal I_{as} shape.

A pixel tracker measurement was used for the integrated luminosity, which has 2.2% uncertainty [81].

Finally, there are several theoretical uncertainties which are important, namely, the nuclear interaction and hardonization models used for hadronizing HSCPs, the multiple parton interaction (MPI) model used in the Monte Carlo generator, and the η distribution variation due to unknown details of the HSCP production process. To model uncertainty in the strong interaction model, the charge-suppression model [19] is

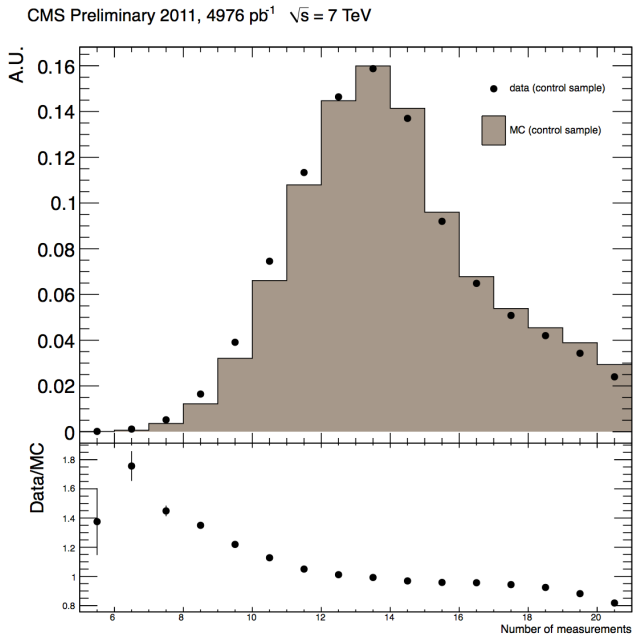

Figure 7.22: The distribution of number of dE/dx measurements (NoM) for data and Monte Carlo Drell-Yan decaying to dimuons. Only the C region sideband is considered, and the distributions are normalized to one. The lower plot shows the ratio of data to Monte Carlo.

considered in addition to the Pomeron and Reggeon exchange model [72]. The latter is used as the default, while the former is more pessimistic in the sense that nearly all R-hadrons become neutral after interaction with the detector calorimeters. Two hadronization schemes of 10% and 50% gluino-gluon ball or glueball fractions were used to account for uncertainty in that model. Limits are presented for the 10% glueball fraction case only. In the case of the small single-HSCP detection efficiency for the gluino, the event-level efficiency is about twice the single-HSCP detection efficiency, so that increasing the glueball fraction to 50% has the effect of reducing the efficiency by a factor of about 1.8. This causes the gluino 10% glueball fraction limits to go up by the same factor.

The MPI tune corresponds to different parton distribution functions (PDF) in the Monte Carlo event generator. The tune used for this analysis is known as D6T, which order the parton showers by Q^2 [82]. A different tune, Z2, which uses the same PDFs but orders the parton showers in P_T, was used to study the effect of changing MPI tunes. The Z2 events contain more initial state radiation, which can increase trigger and reconstruction efficiencies, leading to improved upper limits. Therefore, the D6T tune is used here to be more conservative in limit setting.

To study the effect of an uncertainty on the HSCP η distribution, due to unknown details of the HSCP production process, the two MPI tunes D6T and Z2 were used. The η distribution from the same HSCP model for each tune was compared, and as shown in Figure 7.23, there are no significant differences. Therefore this effect is considered negligible.

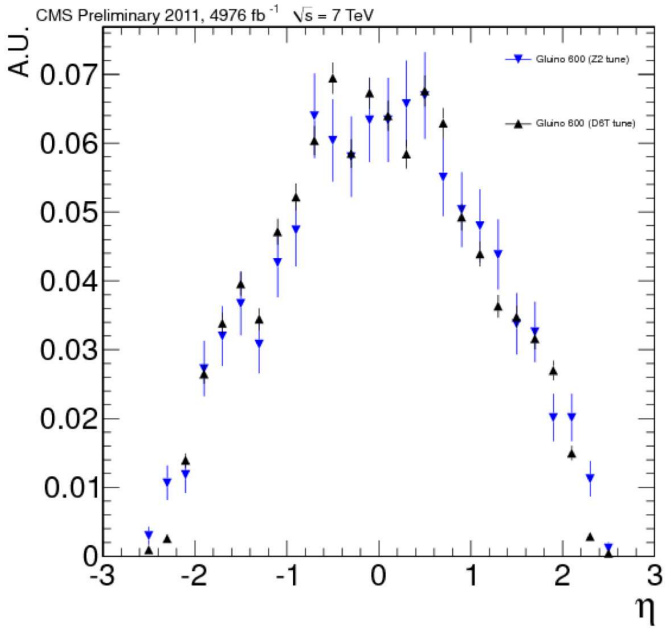

Figure 7.23: The pseudorapidity η distribution for the gluino with mass 600 GeV, using two different Monte Carlo parton distribution function tunes, D6T and Z2. Each distribution is normalized to unity. It can be seen that the two distributions are not significantly different.

Chapter 8

Conclusion

A search for Heavy Stable Charged Particles (HSCP) in the Compact Muon Solenoid (CMS) detector using data collected in the 2011 proton-proton collision run of the Large Hadron Collider has been successfully carried out. Observation of these particles would indicate physics beyond the Standard Model. A description of the Standard Model and models of new physics was described. Limits on the cross section for various HSCP models as a function of mass have been obtained. Comparing these to the theoretical predictions, mass limits are calculated: 1101 GeV for gluinos (0.1 glueball fraction), 750 GeV for stops, and 306 GeV for staus. For the charge suppression models, the limits are 975 GeV for gluinos (0.1 glueball fraction) and 646 GeV for stops. The results have improved upon an earlier cut-and-count technique by using knowledge of the specific ionization (dE/dx) distribution and by binning the data in the pseudorapidity η and the number of dE/dx measurements, variables that are known to affect the shape of the dE/dx distribution. The discovery sensitivity is increased considerably, especially for higher mass HSCP models.

In addition, the CMS electromagnetic calorimeter timing and performance was described, and an application of the timing was presented: the measurement of "satellite" bunches of protons in the Large Hadron Collider (LHC) beam.

This novel HSCP search technique can be expanded to use time-of-flight data from the CMS muon system. Furthermore, with the 2012 LHC data-taking underway, at a higher center of mass energy of 8 TeV, the analysis can provide even stronger results, and its advantage over the cut-and-count analysis should grow as the integrated luminosity

in 2012 exceeds that of 2011.

References

[1] Where we are: The Standard Model. `http://quarknet.fnal.gov/run2/standard.html`.

[2] Precision Electroweak Measurements and Constraints on the Standard Model. 2008, 0811.4682.

[3] Luca Lista. Ewk results from cms. Technical Report CMS-CR-2011-193, CERN, Geneva, Sep 2011.

[4] Stephen P. Martin. A Supersymmetry Primer. 2006. arXiv:hep-ph/9709356.

[5] N. Jarosik, C.L. Bennett, J. Dunkley, B. Gold, M.R. Greason, et al. Seven-Year Wilkinson Microwave Anisotropy Probe (WMAP) Observations: Sky Maps, Systematic Errors, and Basic Results. *Astrophys.J.Suppl.*, 192:14, 2011, 1001.4744.

[6] M. Fairbairn, A.C. Kraan, D.A. Milstead, T. Sjostrand, Peter Z. Skands, et al. Stable massive particles at colliders. *Phys.Rept.*, 438:1–63, 2007, hep-ph/0611040.

[7] G.F. Giudice and R. Rattazzi. Theories with Gauge-Mediated Supersymmetry Breaking. 1998. arXiv:hep-ph/9801271.

[8] Savas Dimopoulos, Scott D. Thomas, and James D. Wells. Sparticle spectroscopy and electroweak symmetry breaking with gauge-mediated supersymmetry breaking. *Nucl. Phys.*, B488:39–91, 1997, hep-ph/9609434.

[9] Marcela S. Carena, Debajyoti Choudhury, Rodolfo A. Diaz, Heather E. Logan, and Carlos E.M. Wagner. Top squark searches at the Tevatron in models of low-energy supersymmetry breaking. *Phys.Rev.*, D66:115010, 2002, hep-ph/0206167.

[10] K.A. Olive. Class notes from Physics 8502: General Relativity and Cosmology II, May 2007.

[11] A. Rizzi et al. Search for Heavy Stable Charged Particles with 100 pb-1 and 1 fb-1 at CMS experiment. CMS AN2007/049.

[12] B.C. Allanach, M. Battaglia, G.A. Blair, Marcela S. Carena, A. De Roeck, et al. The Snowmass points and slopes: Benchmarks for SUSY searches. *Eur.Phys.J.*, C25:113–123, 2002, hep-ph/0202233.

[13] Manuel Toharia and James D. Wells. Gluino decays with heavier scalar superpartners. *JHEP*, 0602:015, 2006, hep-ph/0503175.

[14] Nima Arkani-Hamed and Savas Dimopoulos. Supersymmetric unification without low energy supersymmetry and signatures for fine-tuning at the LHC. *JHEP*, 0506:073, 2005, hep-th/0405159.

[15] JoAnne L. Hewett and Maria Spiropulu. Particle physics probes of extra space-time dimensions. *Ann.Rev.Nucl.Part.Sci.*, 52:397–424, 2002, hep-ph/0205106.

[16] Mark Byrne. Universal extra dimensions and charged LKPs. *Phys.Lett.*, B583:309–314, 2004, hep-ph/0311160.

[17] JoAnne L. Hewett, Ben Lillie, Manuel Masip, and Thomas G. Rizzo. Signatures of long-lived gluinos in split supersymmetry. *JHEP*, 0409:070, 2004, hep-ph/0408248.

[18] Camilo Andrs Carrillo Montoya, Juan Carlos Sanabria, and Marcello Maggi. *Search for Heavy Stable Charged Particles in the CMS Experiment using the RPC Detectors. oai:cds.cern.ch:1360197*. PhD thesis, Andes U., Bogota, 2010. presented Nov 2010.

[19] Rasmus Mackeprang and David Milstead. An Updated Description of Heavy-Hadron Interactions in GEANT-4. *Eur.Phys.J.*, C66:493–501, 2010, 0908.1868.

[20] Frank E. Paige, Serban D. Protopopescu, Howard Baer, and Xerxes Tata. ISAJET 7.69: A Monte Carlo event generator for pp, anti-p p, and e+e- reactions. 2003, hep-ph/0312045.

[21] W. Beenakker, R. Hopker, and M. Spira. PROSPINO: A Program for the production of supersymmetric particles in next-to-leading order QCD. 1996, hep-ph/9611232.

[22] Wim Beenakker, Silja Brensing, Michael Kramer, Anna Kulesza, Eric Laenen, et al. Soft-gluon resummation for squark and gluino hadroproduction. *JHEP*, 0912:041, 2009, 0909.4418.

[23] Fabio Maltoni and Tim Stelzer. MadEvent: Automatic event generation with MadGraph. *JHEP*, 02:027, 2003, hep-ph/0208156.

[24] Torbjorn Sjostrand, Stephen Mrenna, and Peter Z. Skands. PYTHIA 6.4 Physics and Manual. *JHEP*, 05:026, 2006, hep-ph/0603175.

[25] M.A. Dobbs, S. Frixione, Eric Laenen, K. Tollefson, H. Baer, et al. Les Houches guidebook to Monte Carlo generators for hadron collider physics. pages 411–459, 2004, hep-ph/0403045. Compiled by the Working Group on Quantum Chromodynamics and the Standard Model.

[26] Johan Alwall, Simon de Visscher, and Fabio Maltoni. QCD radiation in the production of heavy colored particles at the LHC. *JHEP*, 0902:017, 2009, 0810.5350.

[27] Loic Quertenmont. *Search for Heavy Stable Charged Particles with the CMS detector at the LHC. oai:cds.cern.ch:1361029*. PhD thesis, Louvain U., 2010. presented Oct 2010.

[28] T. Adams, G. Bruno, C. Carrillo, F. Cavallo, J. Chen, S.I. Cooper, et al. Search for Heavy Stable Charged Particles in pp collisions using 2011 CMS data. 2011. CMS AN 2011-167.

[29] T. Adams. Searches for Long-lived Particles at the Tevatron Collider. *Mod.Phys.Lett.*, A23:371–385, 2008, 0802.1048.

[30] G. Aad et al. The ATLAS Experiment at the CERN Large Hadron Collider. *JINST*, 3:S08003, 2008.

[31] A.Augusto Alves et al. The LHCb Detector at the LHC. *JINST*, 3:S08005, 2008.

[32] K. Aamodt et al. The ALICE experiment at the CERN LHC. *JINST*, 3:S08002, 2008.

[33] (ed.) Evans, Lyndon and (ed.) Bryant, Philip. LHC Machine. *JINST*, 3:S08001, 2008.

[34] Jean-Luc Caron. View of the cern / lhc / alps region from the jura.. vue des alpes avec implantation du cern depuis le jura. AC Collection. Legacy of AC. Pictures from 1992 to 2002., Mar 1998.

[35] TOTEM Collaboration, W. Kienzle et al. TOTEM, Total cross section, elastic scattering and diffractive dissociation at the LHC: Technical Proposal. *CERN-LHCC-99-007*, `http://cdsweb.cern.ch/record/385483`.

[36] Stephen Holmes, Ronald S. Moore, and Vladimir Shiltsev. Overview of the Tevatron Collider Complex: Goals, Operations and Performance. *JINST*, 6:T08001, 2011, 1106.0909.

[37] G.L. Bayatian et al. CMS physics: Technical design report. 2006.

[38] Jean-Luc Caron. The LHC injection complex. L'ensemble d'injection du LHC. AC Collection. Legacy of AC. Pictures from 1992 to 2002., May 1993.

[39] Stephen Myers. LHC Commissioning and First Operation. *Conf.Proc.*, C100523:MOXBMH01, 2010.

[40] M. Lamont. The LHC From Commissioning To Operation. *CERN-ATS-2011-186*, `http://cdsweb.cern.ch/record/1382978`.

[41] Absolute calibration of luminosity measurement at cms: Summer 2011 update. `http://http://cdsweb.cern.ch/record/1376102`.

[42] `https://cms.web.cern.ch/org/photos-and-images`.

[43] CMS collaboration. The CMS experiment at the CERN LHC. *JINST*, 0803(S08004), 2008.

[44] S. Boreham, M. Brice, P. Ginter, C. Marcelloni, and M. Hoch. Photos from the cms photo book. CMS Collection., Aug 2008.

[45] CMS, tracker technical design report. 1998. 15 April 1998.

[46] Electromagnetic calorimeter calibration with 7 tev data. 2010. CMS PAS EGM-10-003.

[47] Energy Response and Longitudinal Shower Profiles Measured in CMS HCAL and Comparison with GEANT4. 2006. CMS NOTE 2006/143.

[48] Performance of the cms cathode strip chambers with cosmic rays. *J. Instrum.*, 5(arXiv:0911.4992. CMS-CFT-09-011):T03018 . 39 p, Nov 2009.

[49] Richard Breedon, Peter Timothy Cox, M. Tripathi V Andreev, Katsushi Arisaka, David Cline, Jay Hauser, Mikhail Ignatenko, B Lisowsky, Christina Matthey, Gregory Rakness, and Daniel Wenman. Performance testing of the cms cathode strip chambers. Technical Report CMS-NOTE-2009-020, CERN, Geneva, Nov 2009.

[50] Performance of muon reconstruction in pp collisions at sqrt(s) = 7 tev. 2010. CMS PAS MUO-10-004.

[51] P. Adzic et al. Energy resolution of the barrel of the CMS electromagnetic calorimeter. *JINST*, 2:P04004, 2007.

[52] G. L. Bayatian et al. CMS technical design report, volume II: Physics performance. *J. Phys.*, G34:995–1579, 2007.

[53] Search for a higgs boson decaying into two photons in the cms detector. 2011. CMS PAS HIG-11-030.

[54] CMS: The electromagnetic calorimeter. Technical design report. 1997.

[55] P. Adzic, R. Alemany-Fernandez, C.B. Almeida, N.M. Almeida, G. Anagnostou, et al. Reconstruction of the signal amplitude of the CMS electromagnetic calorimeter. *Eur.Phys.J.*, C46S1:23–35, 2006.

[56] Serguei Chatrchyan et al. Time Reconstruction and Performance of the CMS Electromagnetic Calorimeter. *JINST*, 5:T03011, 2010, 0911.4044.

[57] Electromagnetic calorimeter commissioning and first results with 7 tev data. Technical Report CMS-NOTE-2010-012. CERN-CMS-NOTE-2010-012, CERN, Geneva, Jul 2010.

[58] Vardan Khachatryan et al. Transverse-momentum and pseudorapidity distributions of charged hadrons in pp collisions at sqrt(s) = 7 TeV. *Phys.Rev.Lett.*, 105:022002, 2010, 1005.3299.

[59] Electron reconstruction and identification at sqrt(s) = 7 tev. 2010. CMS PAS EGM-10-004.

[60] S van der Meer. Calibration of the effective beam height in the isr. oai:cds.cern.ch:296752. Technical Report CERN-ISR-PO-68-31. ISR-PO-68-31, CERN, Geneva, 1968.

[61] G Anders, N Bacchetta, V Balabara, C Barschel, D Belohrad, D Berge, H Burkhardt, S I Cooper, M Ferro-Luzzi, G Franzoni, C Gabaldon, M Gagliardi, J J Gras, V Halyo, B Heinemann, P Hopchev, A Hunt, W Kozanecki, S Kwan, M Ludwig, D Marlow, P Odier, S Pagan Griso, J Panman, T Pauly, S Thoulet, S White, J C Yun, and M Zanetti. Lhc bunch current normalisation for the april-may 2010 luminosity calibration measurements. Feb 2011.

[62] A Alice et al. Lhc bunch current normalisation for the october 2010 luminosity calibration measurements. Mar 2011.

[63] W.-M. Yao et al. Review of Particle Physics. *Journal of Physics G*, 33:1+, 2006.

[64] Vardan Khachatryan et al. Search for Heavy Stable Charged Particles in pp collisions at sqrt(s)=7 TeV. *JHEP*, 03:024, 2011, 1101.1645.

[65] Andrea Giammanco. Particle identification with energy loss in the cms silicon strip tracker. Technical Report CMS-NOTE-2008-005. CERN-CMS-NOTE-2008-005, CERN, Geneva, Jun 2007.

[66] Loic Quertenmont. Particle identification with ionization energy loss in the cms silicon strip tracker. Technical Report CMS-CR-2010-120, CERN, Geneva, Jul 2010.

[67] Vardan Khachatryan et al. Cms tracking performance results from early lhc operation. oai:cds.cern.ch:1277738. Jul 2010.

[68] T. Adams, G. Bruno, C. Carrillo, F. Cavallo, J. Chen, S.I. Cooper, et al. Search for Heavy Stable Charged Particles with the CMS detector at $\sqrt{s} = 7$ TeV. 2010. CMS AN 2010-194.

[69] Jet performance in pp collisions at 7 tev. 2010. CMS PAS JME-10-003.

[70] CMS Collaboration. Tracking and Vertexing Results from First Collisions. CMS Physics Analysis Summary, 2010.

[71] Wolfgang Adam, Boris Mangano, Thomas Speer, and Teddy Todorov. Track Reconstruction in the CMS tracker. Technical Report CMS-NOTE-2006-041, CERN, Geneva, Dec 2006.

[72] Rasmus Mackeprang and Andrea Rizzi. Interactions of coloured heavy stable particles in matter. *Eur. Phys. J.*, C50:353–362, 2007, hep-ph/0612161.

[73] CMS Collaboration. Search for Heavy Stable Charged Particles in pp collisions at 7 TeV. 2010.

[74] Steve Baker and Robert D. Cousins. Clarification Of The Use Of Chi Square And Likelihood Functions In Fits To Histograms. *Nucl. Instrum. Meth.*, 221:437–442, 1984.

[75] Robert D. Cousins. Generalization of Chisquare Goodness-of-Fit Test for Binned Data Using Saturated Models. 2010. `http://www.physics.ucla.edu/~cousins/stats/cousins_saturated.pdf`.

[76] L. Moneta, K. Belasco, K.S. Cranmer, A. Lazzaro, D. Piparo, G. Schott, W. Verkerke, and M. Wolf. The RooStats Project. In *13^{th} International Workshop on Advanced Computing and Analysis Techniques in Physics Research (ACAT2010)*. SISSA, 2010, 1009.1003. PoS(ACAT2010)057.

[77] Alexander L. Read. Presentation of search results: The CL(s) technique. *J.Phys.G*, G28:2693–2704, 2002.

[78] Glen Cowan, Kyle Cranmer, Eilam Gross, and Ofer Vitells. Asymptotic formulae for likelihood-based tests of new physics. *Eur.Phys.J.*, C71:1554, 2011, 1007.1727.

[79] Serguei Chatrchyan et al. Determination of Jet Energy Calibration and Transverse Momentum Resolution in CMS. *JINST*, **06**:P11002, 2011, 1107.4277.

[80] CMS Collaboration. Measurement of tracking efficiency. CMS Physics Analysis Summary, 2010.

[81] CMS Collaboration. Absolute Calibration of the Luminosity Measurement at CMS: Winter 2012 Update. CMS Physics Analysis Summary, 2012.

[82] J. Pumplin et al. New generation of parton distributions with uncertainties from global QCD analysis. *JHEP*, 07:012, 2002, hep-ph/0201195.